POLITECNICO DI MILANO

SCUOLA DI INGEGNERIA INDUSTRIALE E
DELL'INFORMAZIONE

Dipartimento di Elettronica, Informazione e Biomedica (DEIB)

Tesi di Laurea Magistrale in
INGEGNERIA BIOMEDICA

Validation of an image registration algorithm to control radiation-induced damage in childhood brain cancer

Relatore: Prof. Luca Mainardi
Correlatore: Ing. Eros Montin

Tesi di Laurea di:
Loredana Storelli 781059

Anno Accademico 2013-2014

A Gianmarco,
la persona che mi ha insegnato ad apprezzare la vita
proprio quando questa gli ha voltato le spalle.

RINGRAZIAMENTI

I miei più sentiti ringraziamenti vanno al Professor Luca Mainardi per aver seguito il mio lavoro con pazienza e professionalità.
Al correlatore Eros Montin che mi ha aiutato, sostenuto, ma soprattutto motivato a proseguire sempre con passione.
Ringrazio tutto il reparto di Risonanza Magnetica dell'Istituto Nazionale dei Tumori di Milano per avermi ospitato durante tutto il lavoro e aver reso più divertenti le giornate.

Un grazie speciale và alla mia famiglia.
Ai miei genitori che hanno reso possibile con tanto sacrificio la mia formazione, mi hanno supportato ed insegnato sempre ad affrontare a testa alta le difficoltà.
A mia sorella Valeria che sò essermi vicina nonostante non riesca a dimostrarlo.
A mia nonna Cecilia che anche da lontano seguiva con ansia ogni mio esame.
Ai miei zii, in particolare a zia Lina e ai suoi piatti buoni da far tornare il buon umore. A zio Tonio e ai suoi discorsi storico/filosofici con cui riesce sempre a incuriosirmi.
A zio Cesare, al sua affetto e alla sua contagiosa allegria, e a zia Maria e alla sua saggezza.
A zia Licia con cui condividere la passione per il cioccolato.
Alle mie cugine (o meglio sorelle) Marilena e Daniela, che con il loro affetto mi hanno sempre incoraggiato e mai dubitato delle mie capacità. A Mimmo con cui condivido sempre tante risate e momenti divertenti; alla piccola peste Marco, che mi ricorda che si ha sempre qualcosa di nuovo da imparare.

Un ringraziamento particolare anche a Rita, Francesco ed Enrico (la mia seconda famiglia). Grazie a Rita, una persona speciale che con il suo continuo sostegno, incoraggiamento e affetto, mi ha permesso di credere sempre in me stessa.
A Francesco, il fratello acquisito, insieme al quale sono cresciuta, maturata e condiviso tante avventure e ad Enrico una persona da cui imparare tante cose.

Ringrazio anche gli amici di studio e non, con cui ho condiviso 5 anni di fatiche e risate. Al compagno di studi Giacomo, a Silvia, Sara, Ludovica e alla compagna di tesi Dzemila.

Alla mia amica Desirêe e al suo sostegno; agli amici dell'Enterprise Hotel, in particolare Baba e al suo profondo ottimismo.

Un grazie anche a tutto lo staff del ristorante Convivium e non solo, che mi hanno accolto con affetto e gioia, a partire da Claudia, Claudio e Nicola, al loro sostegno, al personale di sala e della cucina che con la loro allegria mi hanno sempre messo di buon umore (oltre che farmi ingrassare).

Il ringraziamento più grande però và ad una persona scomparsa troppo presto, a cui non posso più regalare abbracci, nè vedere sorridere, ma che ho sentito vicina soprattutto nei momenti difficili di questo percorso. E' grazie a lui se anche nelle giornate nuvolose mi ricordo dell'esistenza del sole. A lui voglio dire: ce l'abbiamo fatta!

Milano, 18 dicembre 2013

Contents

List of Figures

List of Tables

Abstract

It is well known that radiotherapy for cranial tumors induce toxicity to the central nervous system. This neurotoxicity is a potential cause of neurobehavioral morbidity in childhood cancer survivors affecting different aspects of cognitive function.
It is important in this context to evaluate the damage caused by radiation-therapy at distance of years in order to obtain better pianifications of the future treatments, thus improving the quality of life of the treated subjects.
For this purpose it is important to well compare images at distance of time, with different features, to control the proper growth of the brain structures that have undergone radiation therapy.
The main issue of this work is the validation of an automatic algorithm of image registration to compare post-radiotherapy cerebral structures with the same after a period of follow up, in pediatric subjects with brain tumors all treated with radiation therapy and without recidive.
So a validation framework was produced to verify if the algorithm used for the registration, is able to align correctly Magnetic Resonance Images (with different resolutions and field of view) scanned at distance of years, accounting for physiological growth of the patients.

Introduction

Childhood brain tumors are the most common tumors in children and constitute the largest group of solid neoplasms, second only to leukemia in their overall frequency during childhood.
The treatment of these malignancies is complex and usually combines surgery, chemotherapy and Cranial Radiation Therapy (CRT).
A limitation of radiotherapy (RT) for cranial tumors is the toxicity to the central nervous system [2].
These complications of brain tumors treatment are prevalent and potentially cause neurobehavioral morbidity in childhood cancer survivors [3].
Long-term effects assessment is essential to maximize the quality of life and the identification of the damaged structures in treated patients with cognitive deficit, could improve the radiotherapeutic planning with a saving of the most sensitive structures [4]. So the goal is the identification of structures that are critical in the genesis of cognitive disorders at different RT dose levels in order to obtain better pianifications of the future treatments, thus improving the quality of life.
In this context it is necessary to evaluate RT-induced damages integrating different data; for example data of Diffusion Tensor Imaging (DTI) with morphological sequence of Magnetic Resonance Imaging (MRI). Then the data obtained are merged with radiotherapy plans to test the relationships between locations, dose, distribution and shape of the treatment with detectable abnormalities in various brain structures, such as cerebral cortex, white matter and myelination of the beams.
Thus it is necessary to have a valid clinical instrument that allows the physicians to perform this comparison as reliably as possible.
In this work it was assessed if the automatic algorithm of image registration used is able to perform this task and correctly align post radiotherapy MRI of pediatric brains all with childhood cancer, and MRI of follow up of the same patients at distance of years.

Materials and Methods

Patients included in this study are all with histological diagnosis of malignant brain tumours in pediatric age (from 2 to 17 years old) and treated with focal radiotherapy (min 30.6 - max 67.4 Gy).

The data employed are Magnetic Resonance Images T1-weighted MPR, VIBE or TSE sequences of brain with a Siemens machine of 1.5T, data of DWI and radiosurgical planning.
The automatic image registration algorithm to validate used the open source software *Plastimatch* for image computation [5].

In this study it was implemented a validation framework which includes different steps:

- Generation of a known vector field to deform the image used as 'reference image' (the MRI after the period of follow up).
- Deformation of the reference image with the known vector field previously created using Plastimatch, and degradation of the image in resolution.
- Addition of known Gaussian noise on the deformed image, to create the worse condition for the validation.
- Registration between the original image (reference image) and the degraded one (test image) using an approach based on free-form deformation with B-splines, and mutual information as measurement of similarity.
- Comparison of the vector field estimated from the registration with the known one and error estimation, using different evaluation parameters: Mean Magnitude Error and Normalized Mutual Information.

Finally it was tested the registration framework of the previous validation, to find the optimal input parameters for the algorithm (bin, grid and λ) that offer the best alignment between the two images, in terms of minimization of mean magnitude error. In this case the registration was performed between a brain MRI selected from one of the patients included in this study, and the same image but manually deformed with the software *IRTK-Image Registration Toolkit* to simulate brain growth.

Results

Mean Magnitude Error and Normalized Mutual Information are computed only on the brain area of the image (BET) and reported in a boxplot which represents

the trend of the evaluation parameters at different levels of noise on the image for each patient.
In Figure 1 is shown an example of result found for a patient.

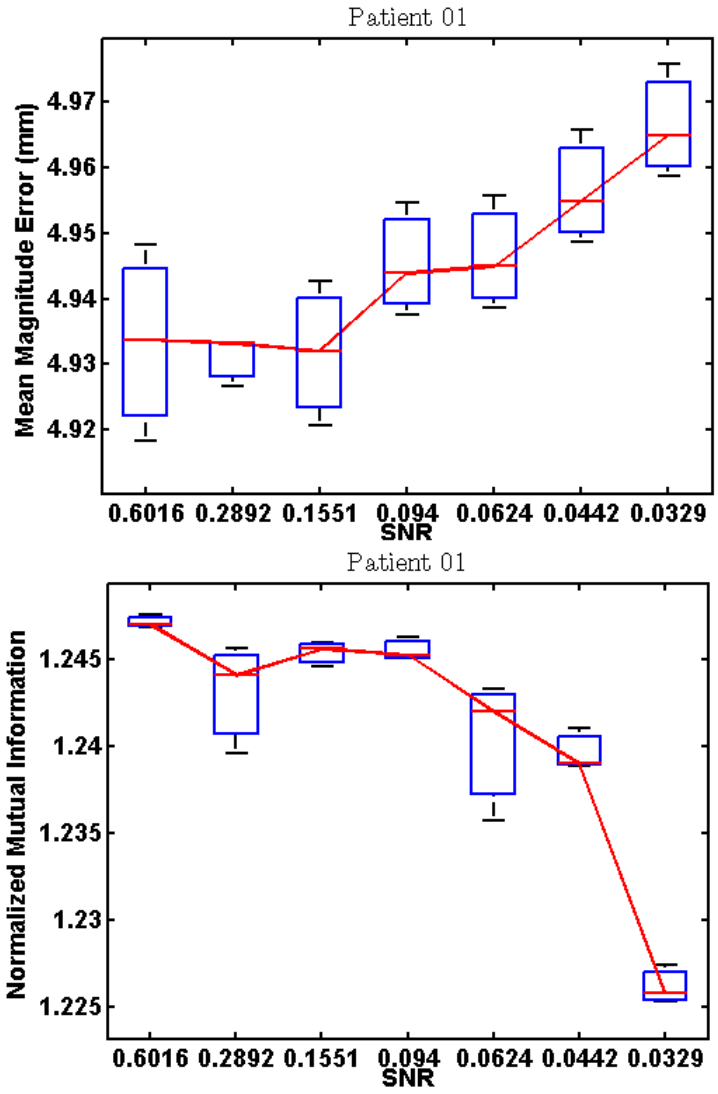

Figure 1: The boxplots represent the trend of registration error in the upper figure and the mutual information in the image below, on the brain area at different levels of Signal-to-Noise Ratio. The red line represents the fitting with spline function of the median values of the parameters for the different repetitions.

It is possible to note in all patients that the trend of the registration error

increases at increasing of noise scaling although the values are acceptable (in the order of mm) also for high noise intensity on the image; while normalized mutual information between the reference and the registered image decreases with worsening of registration.
The trend of the mean error for all patients at increasing of noise intensity on the images is reported in Figure 2.

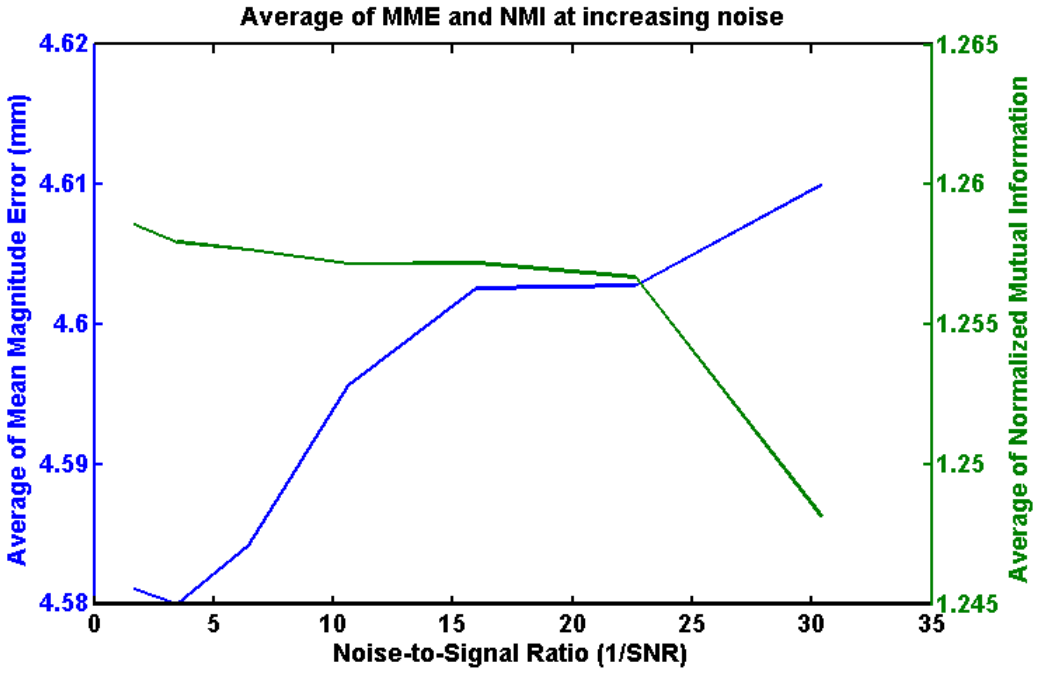

Figure 2: Average of the Mean Magnitude Error (at left) and Normalized Mutual Information (at right) at increasing levels of noise on the images, for all patients.

About the optimization of input parameters in Figure 3 are reported the results obtained.
It is possible to note that there is a range for each of the input parameters that is optimal in term of minimization of the registration error.

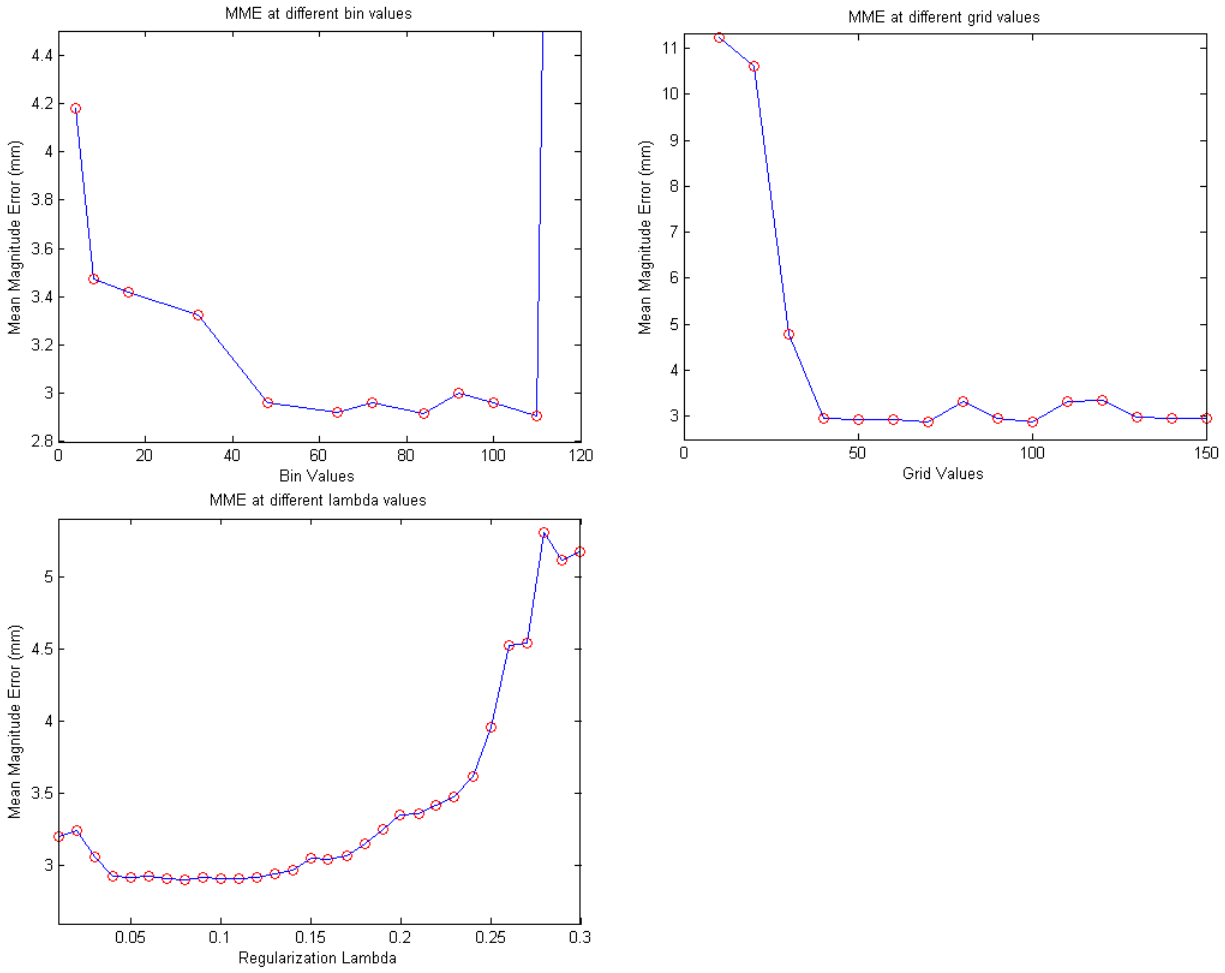

Figure 3: From the top left: The first graphic shows the trend of the registration error at different number of bin values. The near figure represents the trend of the registration error at different grid values, while the figure below shows the same trend but for different λ values.

Conclusions

The algorithm has demonstrated from an initial visual inspection a good capability to correctly align the corresponding structures of two images. This is also confirmed by a quantitative assessment that has revealed negligible registration error (in the order of millimeters) also for high values of noise, and a qualitative assessment by an expert neuroradiologist.
So the *Plastimatch* image registration algorithm demonstrated to have the following properties: reliability, stability and robustness.
The test for the selection of optimal input parameters for the algorithm revealed an optimal range of values in term of minimization of the registration error.
Considering the different number of bin values, it emerged that low values and too high values are not suitable to correctly model the histogram of an image, thus having a bad estimation of the mutual information between the images and producing a bad registration result.
It was also pointed out that the grid dimensions to give in input to the registration algorithm must exceed a certain value, to correctly register them.
For the regularization λ the criterion of selection indicates that too low values are not preferable, to avoid that a weak regularization of the term in the cost function could generate a strong warping of the moving image thus not aligning it correctly to the reference image.
Vice versa high values of λ could weight too much the regularization term and prevent the information conveyed by the mutual information making a great warping, also if it was necessary; thus producing a bad registration result.

From the comparison of Fractional Anisotropy between the structures that have undergone high radiation dose to the same structures that have received little or no dose, it emerged a statistically significant difference.
Therefore, it is important to improve radiosurgical planning in childhood brain tumors. For this purpose it may be useful the functional MRI (fMRI) before each radiosurgical planning to better evaluate what brain structures should strictly avoid radiation treatment.

Sommario

La radioterapia è una terapia medica consistente nell'utilizzo di radiazione ionizzante, in grado di danneggiare il DNA del tessuto bersaglio rendendo questo trattamento dannoso anche per i tessuti sani.
Nel caso di pazienti pediatrici che hanno subito radioterapia all'encefalo, questa può essere a distanza di anni una potenziale causa di morbilità neurocomportamentale che interessa diversi aspetti della funzione cognitiva, in particolare l'attenzione, la memoria e la velocità di ragionamento.
In questo contesto clinico risulta dunque importante valutare eventuali danni ai tessuti causati dalla radioterapia a distanza di anni per poter eventualmente ottenere miglioramenti nelle tecniche di pianificazione in radiochirurgia.
Il principale obiettivo del lavoro quindi è la validazione di un algoritmo automatico di registrazione di immagini che permetta un corretto confronto tra le strutture encefaliche dopo la radioterapia e le stesse dopo un periodo di follow up di almeno 4 anni in assenza di recidive. Tutto ciò per valutare il corretto sviluppo dei tessuti che hanno subito dose di radiazione ionizzante.
E' stata quindi implementata una struttura di validazione per verificare se l'algoritmo utilizzato per la registrazione sia in grado di allineare correttamente le due immagini di Risonanza Magnetica (RM) acquisite a distanza di anni, le quali presentano differenze in risoluzione, campo di vista, ma soprattutto nella grandezza delle strutture di interesse dovute alla fisiologica crescita encefalica degli infanti.

Introduzione

I tumori cerebrali infantili sono i tumori più comuni in età pediatrica e costituiscono il gruppo più ampio di neoplasie solide, seconde solo alla leucemia nella loro frequenza di occorrenza nel periodo dell'infanzia.
Il trattamento di queste neoplasie è complesso e di solito combina chirurgia, chemioterapia e radioterapia encefalica.
Un limite del trattamento radioterapico nei tumori cerebrali è la tossicità indotta al sistema nervoso centrale [2]. Queste complicazioni dovute al trattamento possono minare severamente la qualità di vita del paziente trattato [3].
Dunque è molto importante valutare i danni a lungo termine prodotti dalle radiazioni nei pazienti che hanno subito la radioterapia in età pediatrica. Tutto ciò per cercare di migliorare la pianificazione radiochirurgica al fine di salvaguardare le strutture cerebrali più a rischio, evitando futuri danni neurocomportamentali al paziente [4].
In questo contesto dunque è rilevante integrare dati di tipo diverso, come immagini del Tensore di Diffusione (DTI) e sequenze morfologiche di Risonanza Magnetica (RM) con dati riguardanti la pianificazione radioterapica, per individuare correttamente dose, distribuzione e strutture. A questo scopo è fondamentale avere uno strumento clinico che permetta di integrare tutti questi dati in modo affidabile e robusto.
Lo studio qui proposto si propone quindi di validare un algoritmo automatico di registrazione di immagini, per poter verificare se lo strumento utilizzato è in grado di allineare in modo preciso le strutture cerebrali del paziente acquisite in RM dopo la radioterapia e le stesse a ditanza di anni, dopo un periodo cosiddetto di 'follow up' in assenza di recidive, superando le limitazioni dovute alla diversa risoluzione, campo di vista ma soprattutto dovute alla fisiologica crescita cerebrale del paziente.

Materiali e metodi

I pazienti coinvolti nello studio sono soggetti pediatrici (dai 2 ai 17 anni) con diagnosi istologica di glioma maligno e trattati con radioterapia focale (min 30.6 - max 67.4 Gy).
I dati utilizzati sono immagini RM pesate in T1 con sequenze MPR, VIBE o Turbo

Spin Echo, acquisite con un magnete Siemens a 1.5T, dati di immagini pesate in Diffusione (DWI) e dati riguardanti il trattamento radioterapico.
L'algoritmo da validare utilizza come supporto il software 'open source' *Plastimatch* [5].

Nello studio è stata implementata una struttura di validazione che si articola in diverse fasi:

- Generazione di un vettore di deformazione noto da applicare all'immagine RM attuale (dopo il periodo di 'follow up') usata come immagine di riferimento.

- Deformazione con *Plastimatch* dell'immagine di riferimento usando il vettore di deformazione precedentemente generato e contemporanea degradazione dell'immagine in risoluzione.

- Addizione di un rumore Gaussiano (a media e varianza note) sull'immagine precedentemente deformata (immagine di test).

- Registrazione tra l'immagine di riferimento e l'immagine di test generata ai passi precedenti, usando un approccio basato su deformazioni elastiche (B-splines) e mutua informazione come misura di similarità.

- Comparazione del vector field usato per la deformazione iniziale dell'immagine di riferimento e quello stimato dall'algoritmo di registrazione usando la cifra di merito 'Mean Magnitude Error'. Infine calcolo della mutua informazione normalizzata tra l'immagine di riferimento e quella registrata dall'algoritmo.

Infine è stato testato l'algoritmo di registrazione al variare dei parametri in input per cercare di estrarre i parametri in ingresso all'algoritmo che forniscano il risultato ottimo di registrazione in termini di minimizzazione del 'Mean Magnitude Error'.
Ciò è stato fatto registrando, al variare dei parametri scelti in ingresso (bin, grid, λ), un'immagine di riferimento di un paziente e la stessa deformata manualmente con il software *IRTK* per simulare una crescita cerebrale.

Risultati

Le cifre di merito Mean Magnitude Error e Mutua Informazione Normalizzata (NMI) sono state calcolate solo sulle zone dell'immagine che rappresentano le strutture cerebrali (BET) e riportate in un boxplot che mostra l'andamento della cifra considerata al variare dell'intensità del rumore aggiunto all'immagine.
Nella Figura 4 è possibile osservare un esempio di tale risultato riferito ad un paziente.

E' possibile notare per tutti i pazienti che l'andamento dell'errore di registrazione aumenta all'aumentare dell'intensità del rumore, pur mantenendosi su valori accettabili (nell'ordine dei mm) anche con rumore molto alto.
Viceversa la mutua informazione intuitivamente decresce col peggioramento della registrazione.
Nella Figura 5 sono riportati gli andamenti medi su tutti i pazienti di errore e mutua informazione.

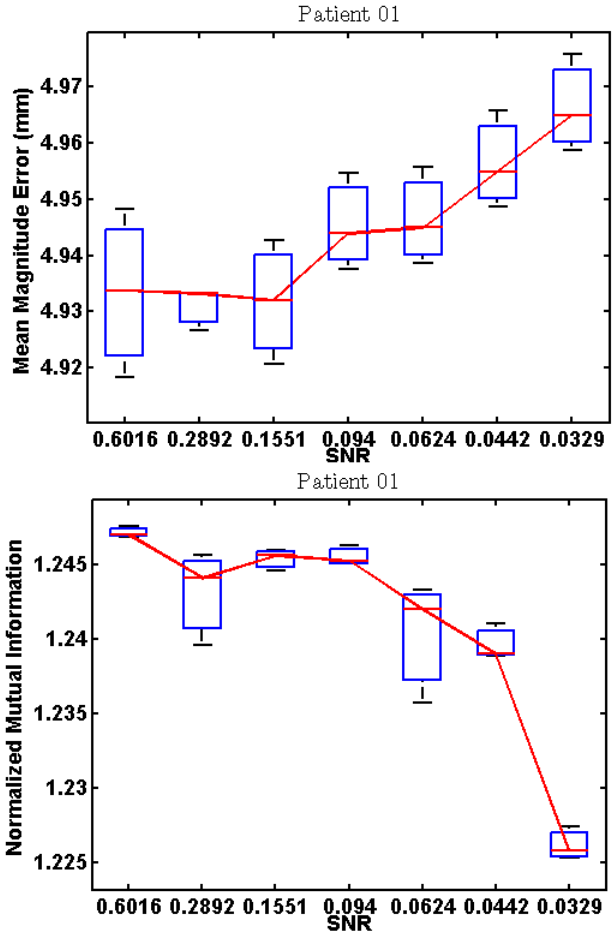

Figura 4: Il boxplot in alto rappresenta l'andamento dell'errore di registrazione sulla zona encefalica a differenti livelli di rapporto segnale-rumore; in basso l'andamento della mutua informazione normalizzata sulla zona encefalica a differenti livelli di rapporto segnale-rumore. La linea rossa rappresenta l'interpolazione con funzione spline delle mediane delle diverse ripetizioni.

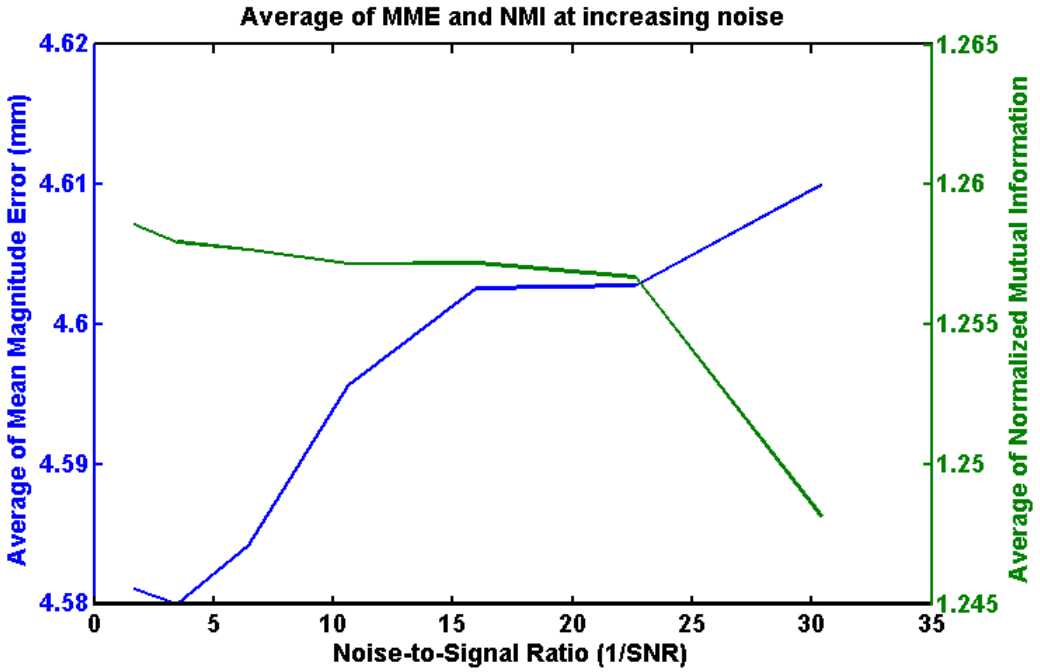

Figura 5: Errore di registrazione medio su tutti i pazienti (andamento in blu) e mutua informazione normalizzata media (andamento in verde) all'aumentare del rumore Gaussiano.

Per quanto riguarda l'ottimizzazione della scelta dei parametri in ingresso è possibile osservare dalla Figura 6 la presenza di un intervallo di valori in cui l'algoritmo è performante.

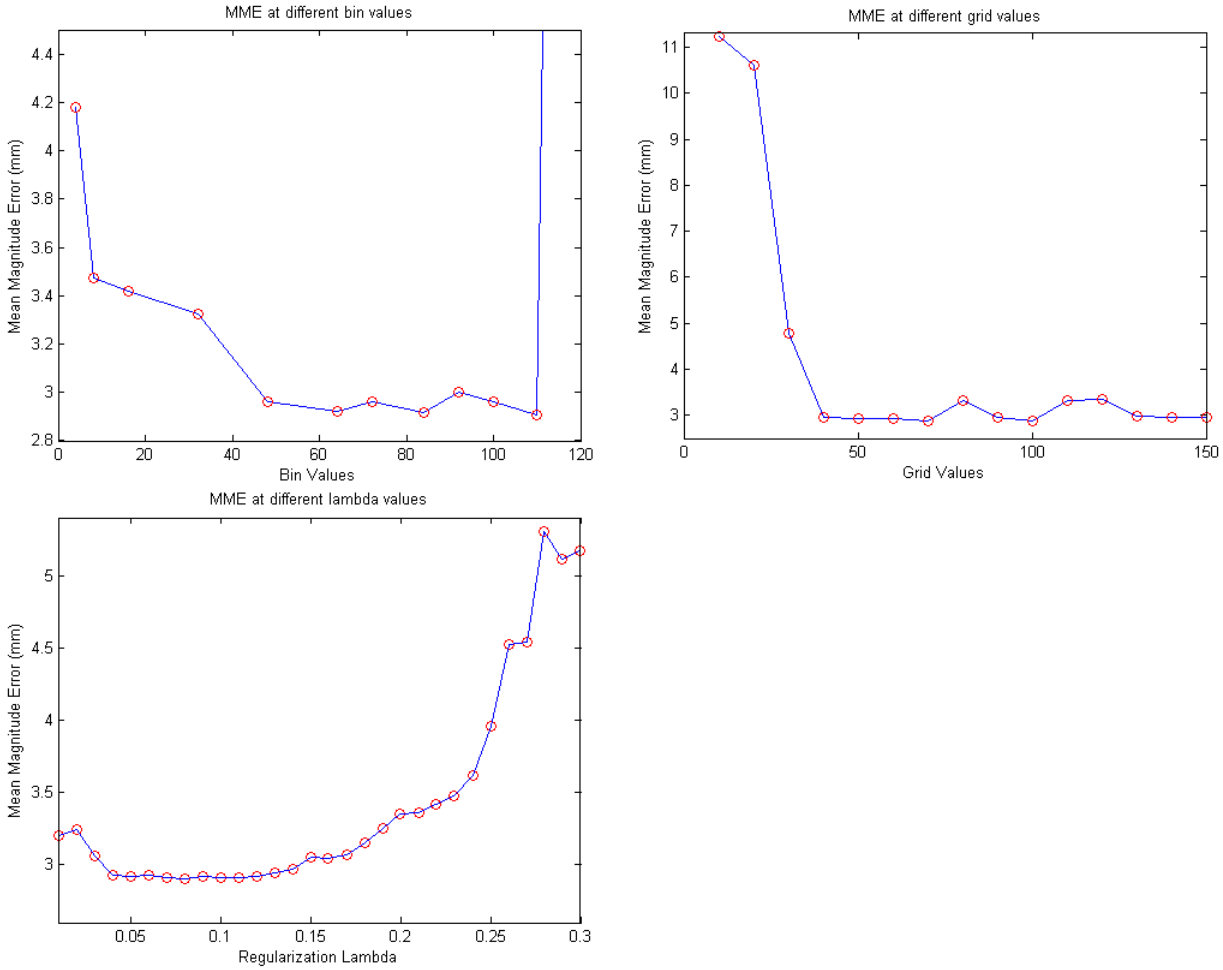

Figura 6: Dalla figura in alto a sinistra: Il primo grafico mostra l'andamento dell'errore di registrazione al variare del valore di bin in ingresso all'algoritmo. La figura accanto mostra sempre il trend dell'errore di registrazione ma al variare dei valori di grid in ingresso. L'ultimo grafico mostra lo stesso al variare dei valori di λ.

Conclusioni

L'algoritmo ha rivelato delle buone prestazioni nell'allineamento corretto delle strutture cerebrali corrispondenti, dimostrandosi affidabile, stabile e robusto. Questo oltre che da un esame visivo è riscontrabile nei valori bassi di errore ottenuti (nell'ordine dei millimetri), anche per livelli elevati di rumore, e da una valutazione

qualitativa da parte di un esperto neuroradiologo.
Per il lavoro di ottimizzazione della scelta dei parametri in ingresso sono stati estrapolati empiricamente degli intervalli ottimali per ognuno dei tre parametri scelti.
Per quanto riguarda il numero di bin è stato selezionato un intervallo intermedio di valori (tra 42 e 110 circa). Per la grid sono preferibili valori maggiori di un certo valore minimo soglia (individuato in questo caso a $\sim 30mm$). Infine per il λ l'intervallo ottimale riguarda un range di valori bassi (tra 0.04 e 0.14), intervallo che si restringe all'aumentare della deformazione applicata all'immagine di partenza.

Dal confronto dei valori di Anisotropia Frazionale tra le strutture che hanno subito dose elevata di radiazione e la stessa zona controlaterale, è emersa una differenza statisticamente significativa.
Pertanto, è fondamentale il miglioramento della pianificazione radiochirurgica nei tumori cerebrali infantili. A tale scopo può essere utile la risonanza magnetica funzionale (fMRI) prima di ogni programma radiochirurgico, al fine di valutare meglio quali strutture cerebrali devono essere assolutamente preservate durante il trattamento.

Chapter 1

Childhood brain tumors

Brain tumor is an intracranial solid neoplasm, which is an abnormal mass of tissue as a result of abnormal growth or division of cells, that include all tumors inside the cranium or in the central spinal canal [1].
They are the most common tumors in children and constitute the largest group of solid neoplasms, second only to leukemia in their overall frequency during childhood [6].
The etiology appears to be multi-factorial and there is no clear primary cause [7].
Intracranial tumors represent approximately 20% of all pediatric malignancies [8].
Worldwide, it is estimated that childhood cancer has an incidence of more than 175,000 per year, and a mortality rate of approximately 96,000 per year [9].
Rates of this disease have increased by 0.6% per year between 1975 to 2002 in the United States and by 1.1% per year between 1978 and 1997 in Europe [10].

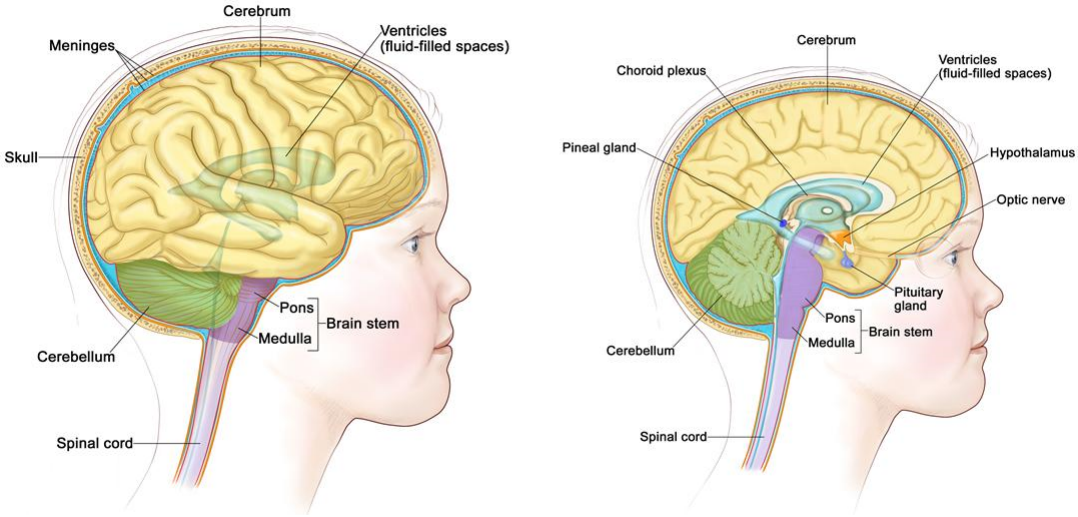

Figure 1.1: Anatomy of the inside of the brain, showing cerebellum, the pineal and pituitary glands, optic nerve, ventricles (with cerebrospinal fluid shown in blue), and other parts of the brain.

Pediatric tumors of the Central Nervous System (CNS) are a very heterogeneous group with varied histologies, ages at onset, and prognoses. In Figure 1.1 is represented the anatomy of the inside of the brain with a relevance for the most sensitive structures.
The overall distribution of childhood brain cancers according to their histological appearance differs markedly from the pattern seen in adults, as shown in Table 1.1 [6].
The majority of pediatric brain tumors arise below the tentorium, which is an extension of the dura mater that separates the cerebellum from the inferior portion of the occipital lobes (see Figure 1.2).

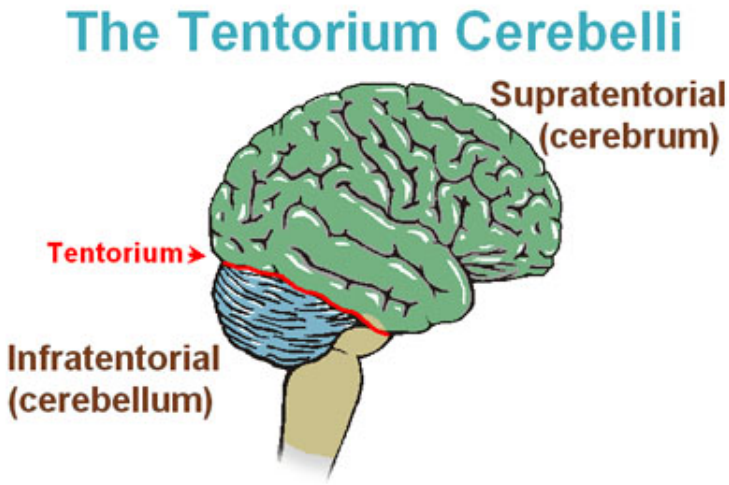

Figure 1.2: Brain: Tentorium cerebelli

Astrocytomas account for 52% of CNS malignancies, medulloblastomas comprise 21%, other gliomas 19%, and ependymomas 9% [1].

LOCATION AND TYPE OF TUMOR	PERCENTAGE OF ALL BRAIN TUMOR
Infratentorial	
Primitive neurodermal tumor (medulloblastoma)	20-25
Low-grade astrocytoma, cerebellar	12-18
Ependymoma	4-8
Malignant glioma, brain stem	3-9
Low grade astrocytoma, brain stem	3-6
Other	2-5
Total	45-60
Supratentorial hemispheric	
Low grade astrocytoma	8-20
Malignant glioma	6-12
Ependymoma	2-5
Mixed glioma	1-5
Ganglioglioma	1-5
Oligodendroglioma	1-2
Choroid-plexos tumor	1-2
Primitive neuroectodermal tumor	1-2
Meningioma	0.5-2
Other	1-3
Total	25-40
Supratentorial midline	
Suprasellar	
Craniopharyngioma	6-9
Low-grade glioma, chiasmatic-hypothalamic	4-8
Germ-cell tumor	1-2
Pituitary adenoma	0.5-2.5
Pineal region	
Low-grade glioma	1-2
Germ-cell tumor	0.5-2
Pineal parenchymal tumor	0.5-2
Total	15-20

Table 1.1: Distribution of common brain tumors in children, according to location and histologic appearance [1].

Improvements in treatment have resulted in an increased rate of survival among those with childhood brain tumors, especially medulloblastoma.
The treatment of CNS malignancies is complex and usually combines surgery, chemotherapy and/or targeted therapies and cranial radiation therapy (CRT) [11]. Although some tumors, according to the location and aggressiveness, such as low-grade astrocytomas, can be treated with surgery alone with a high rate of event free survival, other more aggressive tumor types require additional therapeutic intervention such as radiation [8].
Nonsurgical treatment is currently recommended in unresectable disease with severe or progressive symptoms, or upon radiological progression [12]. Infact the surgical removal of this tumor necessarily involve a craniotomy, that is a surgical operation in which a bone flap is temporarily removed from the skull to access the brain, as shown in Figure 1.3. Craniotomies are often a critical operation performed on patients suffering from brain lesions, also bacterial meningitis usually occurs in about 0.8 to 1.5% of individuals and postcraniotomy pain is frequent and moderate to severe in nature [13].

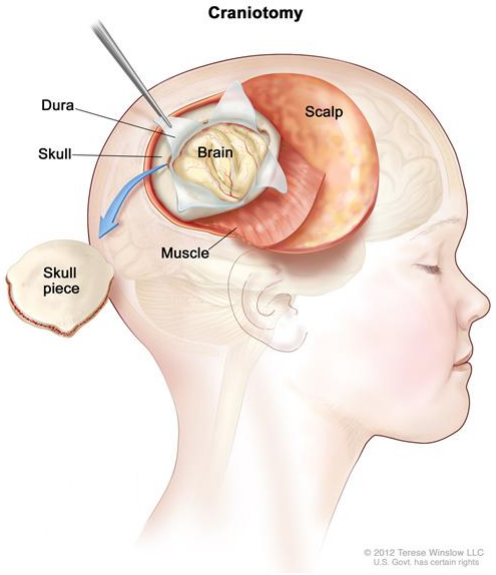

Figure 1.3: Craniotomy: An opening is made in the skull and a piece of the skull is removed to show part of the brain.

1.1 Gliomas

A glioma is a type of tumor that arises from glial cells of the brain or spine [14]. The glial cells are non-neuronal cells that maintain homeostasis, form myelin, and provide support and protection for neurons in the brain and peripheral nervous system.
In Figure 1.4 is shown an example of low-grade glioma in childhood patients.

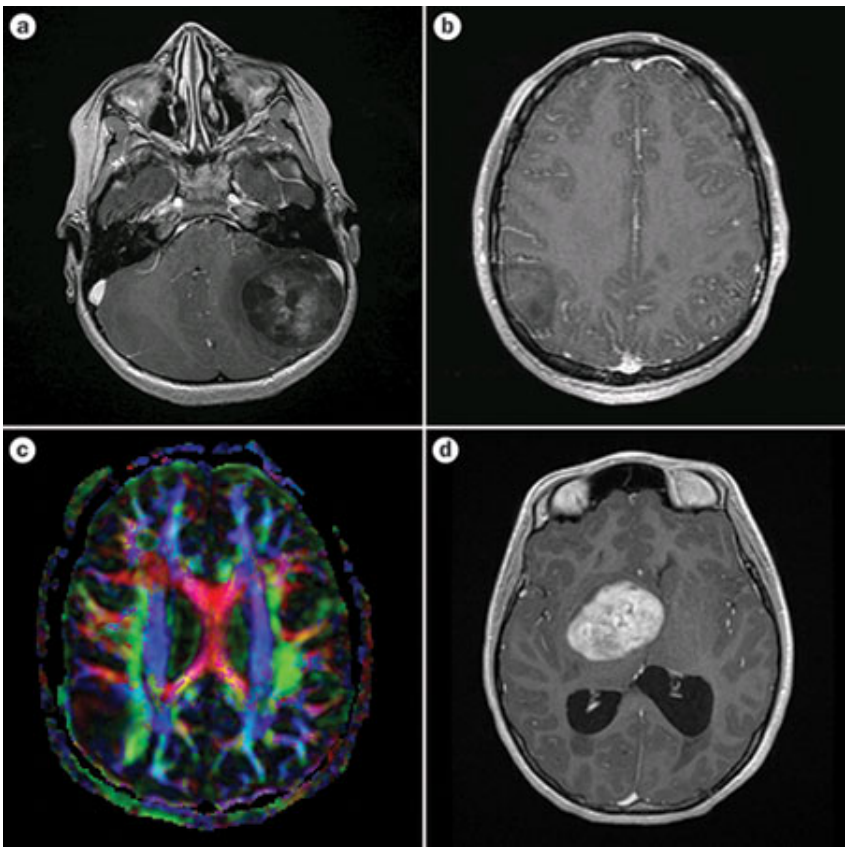

Figure 1.4: a: Axial image of a cerebellar hemispheric pilocytic astrocytoma in a 5-year-old girl. b: Axial image of a non-pilocytic low-grade glioma in a 17-year-old boy. c: Diffusion tensor imaging of the tumor in part b, illustrating displacement of the surrounding white matter pathways away from the tumor. d: Axial contrast-enhanced MRI scan of a diencephalic pilocytic astrocytoma in a 3-year-old girl.

Gliomas are classified by cell type, by grade, and by location.
Gliomas are named according to the specific type of cell they share histological features with, but not necessarily originate from. The main types of gliomas are:

- Ependymomas: ependymal cells.
- Astrocytomas: astrocytes (glioblastoma multiforme is the most common astrocytoma).
- Oligodendrogliomas: oligodendrocytes.
- Brainstem glioma: develop in the brain stem.
- Optic nerve glioma: develop in or around the optic nerve.
- Mixed gliomas, such as oligoastrocytomas, contain cells from different types of glia.

Gliomas are further categorized according to their grade, which is determined by pathologic evaluation of the tumor.

- Low-grade gliomas are well-differentiated (not anaplastic); these tend to exhibit benign tendencies and portend a better prognosis for the patient. However, they have a uniform rate of recurrence and increase in grade over time so should be classified as malignant.
- High-grade gliomas are undifferentiated or anaplastic; these are malignant and carry a worse prognosis.

A final classification of gliomas is according to whether they are above or below a membrane in the brain called the tentorium (Figure 1.2).

- supratentorial: above the tentorium, in the cerebrum, mostly found in adults (70%).
- infratentorial: below the tentorium, in the cerebellum, mostly found in children (70%).
- pontine: located in the pons of the brainstem. The brainstem has three parts (pons, midbrain and medulla); the pons controls critical functions such as breathing, making surgery on these extremely dangerous.

1.1.1 Pathophisiology

High-grade gliomas are highly-vascular tumors and have a tendency to infiltrate. They have extensive areas of necrosis and hypoxia. Often tumor growth causes a breakdown of the blood–brain barrier in the vicinity of the tumor. As a rule, high-grade gliomas almost always grow back even after complete surgical excision, and so are commonly called recurrent cancer of the brain.
On the other hand, low-grade gliomas grow slowly, often over many years, and can be followed without treatment unless they grow and cause symptoms.
Several acquired (not inherited) genetic mutations have been found in gliomas. Tumor suppressor protein 53 (p53) is an early mutation [15].
p53 during DNA and cell duplication, makes sure that the DNA is copied correctly and destroys the cell (apoptosis) if the DNA is mutated and can't be fixed. When p53 itself is mutated, other mutations can survive.
Phosphatase and tensin homolog (PTEN), another protein that also helps destroy cells with dangerous mutations, is itself lost or mutated. Epidermal growth factor receptor (EGFR), a growth factor that normally stimulates cells to divide, is amplified and stimulates cells to divide too much. Together, these mutations lead to cells dividing uncontrollably, a hallmark of cancer.
Recently, mutations in IDH1 and IDH2 were found to be part of the mechanism and associated with a more favorable prognosis [16]. The IDH1 and IDH2 genes are significant because they are involved in the citric acid cycle in mitochondria. Mitochondria are involved in apoptosis. Furthermore, the altered glycolysis metabolism in some cancer cells leads to low oxygen (hypoxia).
The normal response to hypoxia is to stimulate the growth of new blood vessels (angiogenesis). So these two genes may contribute to both the lack of apoptosis and vascularization of gliomas.

1.1.2 Treatment

Treatment for brain gliomas depends on the location, the cell type and the grade of malignancy. Often, treatment is a combined approach, using surgery, radiation therapy, and chemotherapy [17].
The radiation therapy is in the form of external beam radiation or the stereotactic approach using radiosurgery.

Spinal cord tumors can be treated by surgery and radiation.
Temozolomide instead is a chemotherapeutic drug that is able to cross the blood–brain barrier effectively and is currently being used in therapy for high-grade tumors.

A 2007 meta-analysis compared surgical resection and biopsy as the initial surgical management option. Results show that there is insufficient evidence to make a reliable decision [18].
For high-grade gliomas, a 2003 meta-analysis compared radiotherapy with radiotherapy and chemotherapy. It showed a small but clear improvement from using chemotherapy with radiotherapy [19].
In low grade gliomas a comparative study found that treatment a center that favored early surgical resection was associated with better overall survival than treatment at a center that favored biopsy and watchful waiting [20].
For Glioblastoma Multiforme, a 2008 meta-analysis showed that Temozolomide is an effective treatment for "prolonging survival and delaying progression as part of primary therapy and with a low incidence of early adverse events" [21].

1.2 Astrocytomas

Astrocytomas are a type of cancer of the brain that originates in a particular kind of glial cells, star-shaped brain cells in the cerebrum called astrocytes [22].
Astrocytomas are the most common glioma and can occur in most parts of the brain and occasionally in the spinal cord. This type of tumor does not usually spread outside the brain and spinal cord and it does not usually affect other organs. Within the astrocytomas, there are two broad classes recognized in literature, those with [23]:

- Narrow zones of infiltration (mostly invasive tumors; e.g., pilocytic astrocytoma, subependymal giant cell astrocytoma, pleomorphic xanthoastrocytoma), that often are clearly outlined on diagnostic images.

- Diffuse zones of infiltration (e.g., high-grade astrocytoma, anaplastic astrocytoma, glioblastoma), that share various features, including the ability to arise at any location in the CNS, but with a preference for the cerebral hemispheres; they occur usually in adults; and an intrinsic tendency to progress to more advanced grades.

The low-grade type, as in Figure 1.5, is of peculiar interest because it is principally observed in children or young adults and are credited with a relatively good prognosis [24].
It consists of relatively slow-growing astrocytomas, usually considered benign that sometimes evolve into more malignant or as highergrade tumors. This benign nature, however, applies only to the pilocytic subtype, which has long been recognized as a potentially curable tumor, especially in the cerebellum, its usual localization. Unfortunately, pilocytic astrocytomas are few in the cerebral hemispheres, whereas the other subtypes, namely fibrillary astrocytomas, protoplasmic astrocytomas, gemistocytic astrocytomas, and mixed oligoastrocytomas, are clearly dominant, with a more severe prognosis.
Improvements in neuroimaging permit the diagnosis of many low-grade astrocytomas that would not have been recognized previously.

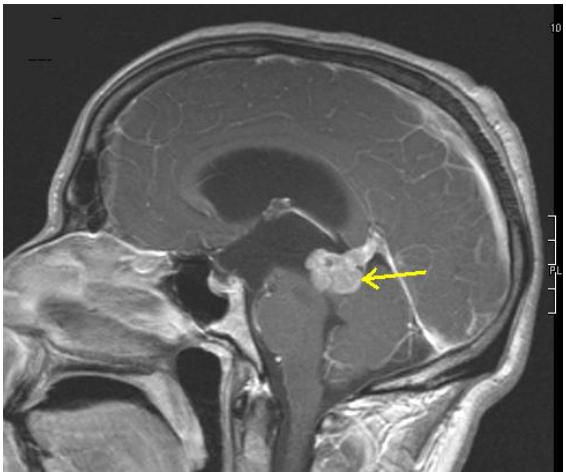

Figure 1.5: Low grade astrocytoma of the midbrain (lamina tecti). Sagittal T1-weighted magnetic resonance imaging. The tumor is marked with an arrow.

1.2.1 Pathophysiology

Astrocytoma causes regional effects by compression, invasion, and destruction of brain parenchyma, arterial and venous hypoxia, competition for nutrients, release of metabolic end products (e.g., free radicals, altered electrolytes, neurotransmitters), and release and recruitment of cellular mediators (e.g., cytokines) that disrupt normal parenchymal function.
Secondary clinical sequelae may be caused by elevated intracranial pressure (ICP) attributable to direct mass effect, increased blood volume, or increased cerebrospinal fluid (CSF) volume [22].
The World Health Organization (WHO) scheme is based on the appearance of certain characteristics: atypia, mitoses, endothelial proliferation, and necrosis. These features reflect the malignant potential of the tumor in terms of invasion and growth rate. Tumors without any of these features are grade I, and those with one of these features (usually atypia) are grade II. Tumors with 2 criteria and tumors with 3 or 4 criteria are WHO grades III and IV, respectively. Thus, the low-grade group of astrocytomas are grades I and II.

1.2.2 Treatment

There is no accepted standard of treatment for low-grade or anaplastic astrocytoma. Generally removal of the tumor will allow functional survival for many years. In some reports, the five-year survival has been over 90% with well resected tumors [24].
Indeed, broad intervention of low grade conditions is a contested matter. In particular, pilocytic astrocytomas are commonly indolent bodies that may permit normal neurologic function. However, left unattended these tumors may eventually undergo neoplastic transformation.
To date, complete resection of high grade astrocytomas is impossible because of the diffuse infiltration of tumor cells into normal parenchyma.
Thus, high grade astrocytomas inevitably recur after initial surgery or therapy, and are usually treated similarly as the initial tumor. Despite decades of therapeutic research, curative intervention is still nonexistent for high grade astrocytomas; patient care ultimately focuses on palliative management.

1.3 Medulloblastomas

Medulloblastoma is a highly invasive embryonal neuroepithelial tumor that arises in the cerebellum or posterior fossa and has a tendency to disseminate throughout the CNS early in its course [25].
In Figure 1.6 is shown an example of medulloblastoma of the cerebellum. Tumors that originate in the cerebellum are referred to as infratentorial because they occur below the tentorium.
Morphologically similar tumors arising in the pineal region are termed pineoblastomas, and those arising in other CNS locations are called primitive neuroectodermal tumors (PNETs).

Figure 1.6: MRI showing a medulloblastoma of the cerebellum. The tumor is marked with an arrow.

Medulloblastoma affects children 10 times more than adults and it is the second most frequent brain tumor in children after astrocytoma [26].
In adults, medulloblastoma is rare, comprising fewer than 2% of CNS malignancies.

1.3.1 Pathophysiology

Medulloblastoma is a cerebellar tumor arising predominantly from the cerebellar vermis. The histogenesis of medulloblastoma remains controversial.
One view suggests that the cell of origin derives from the external granular layer of the cerebellum [27].
Another hypothesis proposes that medulloblastomas have more than one cell of origin. This is based on studies showing differential immunoreactivity to a neuronal calcium-binding protein that is not expressed in the external granular layer and to a beta-tubulin isotype that is expressed in the neuronal cells of the ventricular matrix and external granular layer. Numerous molecular alterations that appear to modulate the biological behavior of medulloblastoma or its response to therapy have been reported [28].

As the tumor grows, obstruction of cerebrospinal fluid (CSF) passage through the fourth ventricle generally occurs, resulting in hydrocephaly. The tumor may spread contiguously, to the cerebellar peduncle and/or the floor of the fourth ventricle; anteriorly, to the brainstem; inferiorly, to the cervical spine; or superiorly, above the tentorium. It also may spread via the CSF intracranially or to the leptomeninges and spinal cord. Of all the pediatric CNS neoplasms, medulloblastoma has the greatest propensity for extraneural spread, especially to bone and bone marrow; however, the rate of such events is less than 4% [29].

1.3.2 Treatment

With aggressive surgery, craniospinal radiotherapy and chemotherapy, more than 50% of children with medulloblastoma can be expected to be free of disease 5 years later. Using current treatments, 80-90% of those without disseminated disease can be cured; however, treatment for this disease often results in significant endocrinological and intellectual sequelae [30].

Standard therapy for medulloblastoma consists of aggressive surgery followed by radiation to the entire craniospinal axis with boost to both the primary tumor site and focal CNS metastatic sites. Recently, adjuvant chemotherapy has also been shown to be beneficial [31].

1.4 Ependymomas

Ependymoma is a tumor that arises from the ependyma, a tissue of the central nervous system. Usually, in pediatric cases the location is intracranial, while in adults it is spinal.
The common location of intracranial ependymoma is the fourth ventricle, as shown in Figure 1.7. Rarely, ependymoma can occur in the pelvic cavity.

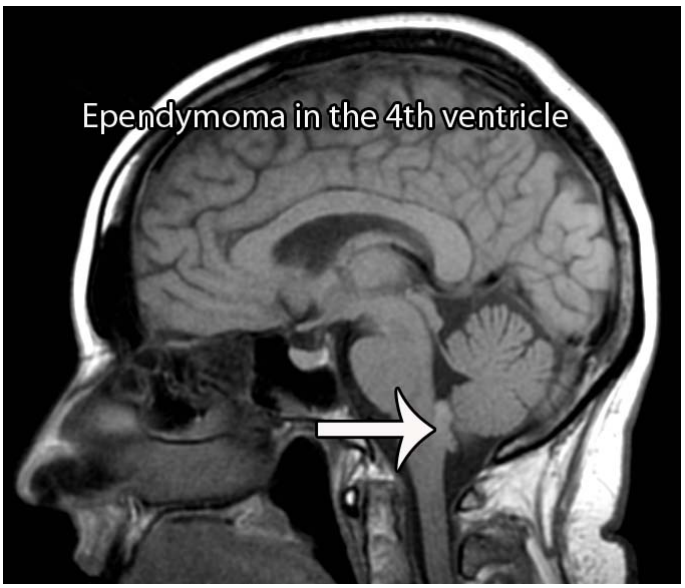

Figure 1.7: Ependymoma in the 4th ventricle. The tumor is marked with an arrow.

Ependymomas are classified as either supratentorial (in the cerebral hemispheres) or infratentorial (in the back of the brain). Variations of this tumor type include subependymoma, subependymal giant-cell astrocytoma, and malignant ependymoma. Ependymoblastoma, which occurs in infants and children under three years, is no longer considered a subtype of ependymoma.
The World Health Organization (WHO) divides them into 4 types on the basis of histologic appearance:

- WHO grade I: Myxopapillary ependymoma, subependymoma.
- WHO grade II: Ependymoma (with cellular, papillary, and clear cell variants).

- WHO grade III: Anaplastic ependymoma

1.4.1 Pathophysiology

Ependymomas are traditionally thought to arise from oncogenetic events that transform normal ependymal cells into tumor phenotypes. The precise nature and order of these genetic events are unknown; however, significant progress has been made toward delineating mutations that segregate with various tumor phenotypes. Some evidence now suggests that radial glia may be the cells of origin [32].

1.4.2 Treatment

Well-differentiated ependymomas are usually treated with surgery. For other ependymomas, total surgical removal is the preferred treatment in addition to radiation therapy.
The malignant (anaplastic) varieties of this tumor, malignant ependymoma and the ependymoblastoma, are treated similarly to medulloblastoma but the prognosis is much less favorable.
Malignant ependymomas may be treated with a combination of radiation therapy and chemotherapy. Ependymoblastomas, which occur in infants and children younger than 5 years of age, may spread through the cerebrospinal fluid and usually require radiation therapy.
The subependymoma, a variant of the ependymoma, is apt to arise in the fourth ventricle but may occur in the septum pellucidum and the cervical spinal cord. It usually affects people over 40 years of age and more often affects men than women.

1.5 Cranial Radiation Therapy (CRT)

Radiation therapy is an effective cancer treatment option in conjunction with chemotherapy and surgery and it uses high-energy rays to kill tumor cells, thereby stopping them from growing and multiplying [33].
Radiation therapy may be used for people who cannot undergo surgery. In other cases, it is used after surgery to kill any tumor cells that may remain.
It is a local therapy. This means that it affects only cells in its path.
Cranial irradiation is used to treat patients with primary or metastatic brain tumors and as prophylaxis for selected patients at high risk of neoplastic involvement of the nervous system. It does not harm cells elsewhere in the brain.
In cranial tumors different type of protocols are expected for the treatment, according to the histological type of the brain tumor; they can execute the complete irradiation of the central nervous system or only a focused irradiation of the precise site of the lesion [2].

1.5.1 Effects of radiation in tissues

By penetrating in a tissue, radiation interact with cellular components, leading energy according to a curve called Dose Delivery Curve. Dose is defined as amount of energy in the mass unit:

$$D = \frac{dE}{dm}[Gy] \tag{1.1}$$

It is visible from Figure 1.8 that the dose delivery in a tissue is not linear until it exceeds the point of maximum dose relase, called Build Up point.

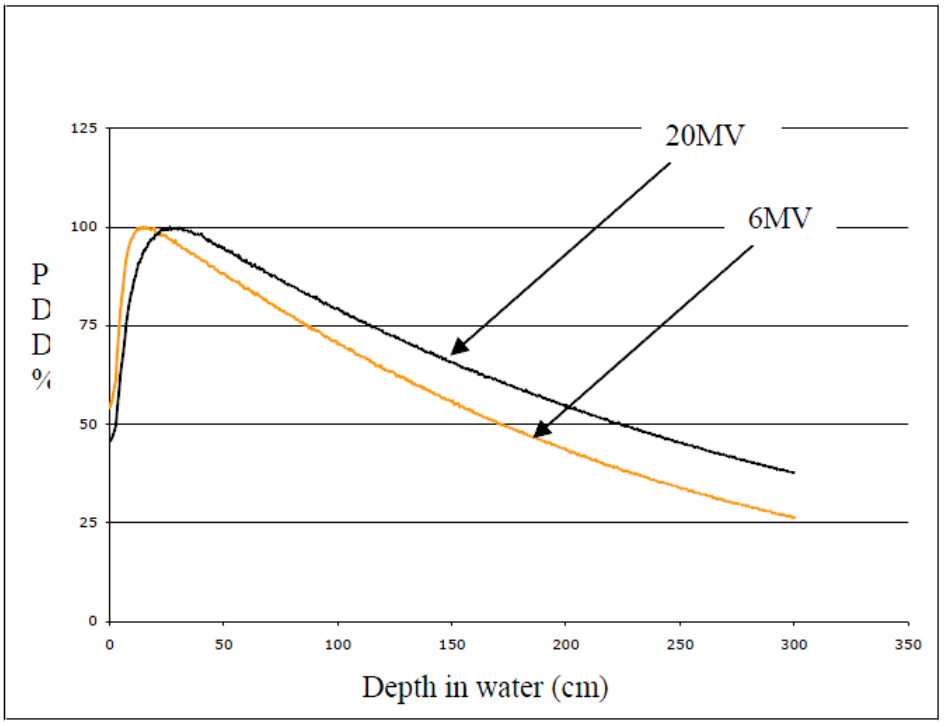

Figure 1.8: Dose delivery depending on the depth of penetration of the radiation X. The dose absorbed by tissue is highest in the first 10 cm crossed. For this reason treat deep lesions becomes problematic for the release of dose in non-pathological tissues. In the figure are shown two curves release dose, representatives of two different intensity beam (6 and 20 mV). It can be noted that a high-intensity beam has a penetration greater than one of lesser intensity. In this image the field of view is 20x20 cm.

In general, the damage induced by ionizing radiation is probabilistic, but if the given dose is very high, one can speak of a deterministic correlation between dose and expected damage. Indeed, there is a dose-characteristic threshold beyond which there is cell death or proliferative inhibition due to the irradiation.
In this case radiation therapy kills cancer cells by damaging their DNA.
This DNA damage is caused by one of two types of energy, photon or charged particle involved in the radiation and is either direct or indirect ionization of the atoms which constitute the DNA chain [34]. Indirect ionization happens as a result of the ionization of water, forming free radicals, notably hydroxyl radicals, which then damage the DNA. While the healthy tissues show a good ability in repair DNA damages, the tumor tissues have less efficient recovery mechanisms.
Double-stranded DNA breaks, as shown in Figure 1.9, prove to be the most significant technique to cause cell death [34].

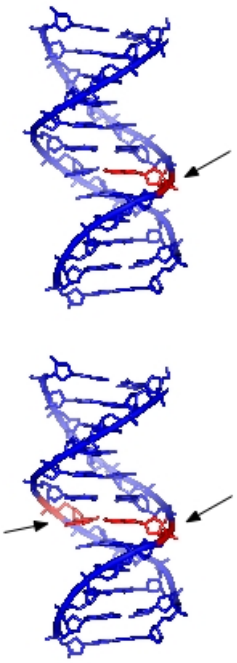

Figure 1.9: The irradiation of tissues can cause a single break of DNA chain (first figure) or a double strand break (figure below). Double-stranded DNA breaks prove to be the most significant because cells are unable to retrieve the damage, coming to death.

The success of radiation therapy depends on the total radiation dose to which the tumor is subjected, this is limited by the tolerance of healthy tissue surrounding the lesion [35]. Infact high doses of radiation give better local control of the lesion and a longer survival without relapse, but it is extremely important that the tolerance of the surrounding healthy tissue is respected.
For this purpose the radiation treatment consists of two processes: the radiosurgical planning and the irradiation. The phase of planning provides the acquisition of biomedical images, used for the contouring of the organs at risk and the definition of the treatment volume, as shown in Figure 1.10. On the basis of such information is calculated the dose profile to be dispensed, avoiding that healthy organs surrounding the lesion are included in the radiation field and getting the best possible uniformity in the volume of interest.

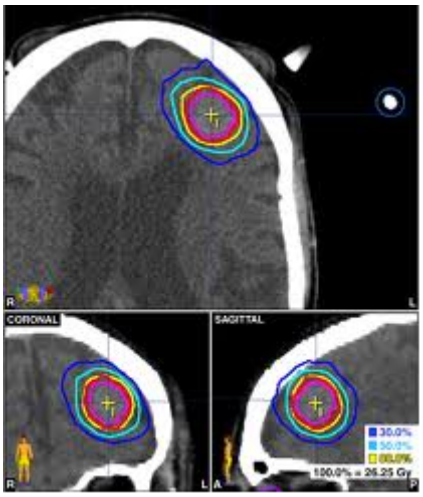

Figure 1.10: There are three main volumes in radiotherapy planning. The first is the position and extent of gross tumour (GTV), i.e. what can be seen, palpated or imaged; the second volume contains the GTV, plus a margin for sub-clinical disease spread which therefore cannot be fully imaged; this is known as the clinical target volume (CTV). The third volume, the planning target volume (PTV), allows for uncertainties in planning or treatment delivery. It is a geometric concept designed to ensure that the radiotherapy dose is actually delivered to the CTV. Radiotherapy planning must always consider critical normal tissue structures, known as organs at risk.

The step of irradiation is in turn composed of two parts: the setup of the patient and the delivery of the dose of radiation. The setup is performed at the beginning of each treatment session and consists in positioning and immobilization of the patient, to reproduce the geometric configuration of the phase of radiosurgical planning.
During the irradiation phase is emitted radiant beams defined in the treatment plan. In Figure 1.11 is reported an example of linear accelerator for the irradiation, integrated with an imaging acquisition system.

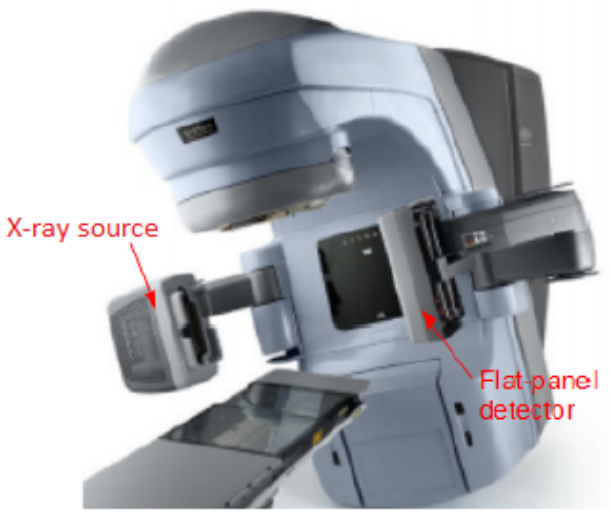

Figure 1.11: Acquisition system with integrated the linear accelerator in the treatment room. There are visible the Flat-panel detector and the X-ray source.

Imaging plays an important role in the whole process of radiation treatment because it is the basis of the recognition and diagnosis of malignant disease, for the process planning, for the assessment of patient positioning and distribution of dose and to monitor the patient's response to treatment.

1.5.2 Radiation-induced damage

Radiation therapy has led directly to significant increases in survival of children with certain types of intracranial tumors [11]. Improvements in treatment have resulted in an increased rate of survival among those with childhood brain tumors, especially medulloblastoma; however, given the aggressive nature of this therapy, concomitant with improved survival rates is the recognition that many long-term survivors have permanent neurologic, neurocognitive, endocrinologic, and neuropsychologic deficits. So children are at risk for exhibiting changes in brain structure, neuronal biochemistry, and neurocognitive functioning, since brain is highly vulnerable to neurotoxic agents during the prime learning period of a child's life [11]. For example several clinical trials on Primary Central Nervous System lymphoma (PCNSL) have reported neurotoxicity as a consequence of therapy [36]. When a combination of whole-brain radiotherapy and chemotherapy is used, the incidence ranges from 20% to 30% of patients [37].
So a limitation of radiotherapy (RT) for cranial tumors is the toxicity to the central nervous system [2].

Radiation-induced brain injury has traditionally been divided into three temporal phases [2]:

- acute: appears to be secondary to transient vasogenic edema and occurs within several weeks after treatment.
- early delayed: which occurs within 1–6 months following RT treatment and typically impacts deep gray and white matter.
- late delayed: which may occur months to years following treatment.

In each of the stages of radiation injury, there is an increase in free tissue water that may result from damaged endothelial cells or demyelination. These damages can potentially cause increased capillary permeability and vasogenic edema, or cause water to replace hydrophobic myelin [38].
Although acute and early delayed effects are transient, late delayed injury is usually permanent and is characterized by necrosis and histopathologic abnormalities [39].

The extent of these delayed effects varies with radiation dose, brain volume irradiated, and age at treatment, and might also be influenced by genetic factors and individual susceptibility [11].
Late radiation injury has been associated with leukoencephalopathy, brain atrophy, necrosis, endocrine dysfunction and neurocognitive deterioration [40].
In humans, numerous cross-sectional studies have correlated white matter degradation with cognitive decline in adult survivors of childhood cancers [41, 42]. Radiation affects subcortical white matter function, as opposed to cortical functions that the tumor itself may affect [43].
In particular children treated with cranial irradiation for brain tumors have reduced white matter volume and deficits in reading ability [44].

Treatment effects on growth are multifactorial and include also the difficulty distinguishing between tumor and treatment effects on cognitive function, these patients also may have additional medical problems, which may have a negative impact on neurocognitive function [45].
This neurotoxicity is a potential cause of neurobehavioral morbidity in childhood cancer survivors affecting different aspects of cognitive function, especially attention, memory, and processing speed, which, in turn, affect intelligence quotient (IQ) and academic achievement [46, 47].
It is well documented that children with tumors arising in the suprasellar region have a high likelihood of permanent long term hormonal dysfunction [48].
High-dose irradiation to the hypothalamic region may result in delayed-onset hormonal deficiency [49]. In addition, neurocognitive dysfunction has consistently been documented years after treatment in children receiving brain irradiation [50]. The likelihood of such deficits occurring has been related to early age at diagnosis and treatment; type, extent, and location of tumor; and the dose of radiation and volume received.
The incidence of neurologic sequelae suffered by children with brain tumors, and the time of onset of such difficulties, has not been extensively evaluated.

These complications of brain tumor treatment are prevalent and severely impact upon the patient's quality of life [3]. So there is a greater and more urgent need for attention to neurocognitive outcomes, contributing to the quality of life of these

children.

Although the understanding of what causes late delayed cognitive decline is still limited, long-term effects assessments are essential to maximize the quality of life of survivors of childhood cancer and the identification of the damaged structures in treated patients with cognitive deficit, could improve the radiotherapeutic planning with a saving of the most sensitive structures; thus reducing the appearance of cognitive and learning problems together with a reduction of rehabilitative needs and scholar support [4].
Understanding brain development and the relationship between neurogenesis, memory, and anatomical structures that are linked to memory is a crucial step towards better identifying long-term CRT-induced cognitive defects and development of treatment interventions or preventive measures [11].
Many newer treatment approaches have attempted to address this problem by reducing the dose of the Craniospinal Irradiation (CSI) component of radiation therapy while maintaining the current survival rates [51].

The evidence of a significance statistical association between the parameters of interest could give new knowledge on the role of the radio-induced damages in the genesis of the cognitive deficit post radiotherapy. So the goal is the identification of structures that are critical in the genesis of cognitive disorders at different RT dose levels in order to obtain better pianifications of the future treatments, thus improving the quality of life [11].

Chapter 2

Experimental Protocol

2.1 Patients enrollment

In this study 10 patients have been enrolled with histological diagnosis of malignant brain tumours in pediatric age (from 2 to 17 years old) and treated with focal radiotherapy (min 30.6 - max 67.4 Gy) at the IRCCS Eugenio Medea at Bosisio Parini (LC).
A further inclusion criteria was the lack of relapse at the time of entering the study and no documented major neurosurgical injury.

2.2 Data

Data used are Magnetic Resonance Images (MRI) acquired at IRCCS Istituto Nazionale dei Tumori (INT) in Milan, with a Siemens machine of 1.5 T.
The images are all T1-weighted MPR, VIBE or TSE sequences of brain (Appendix A), with a resolution of 0.5 mm x 0.5 mm x 1 mm and a field of view of 500 x 500 pixels for each of the 180 axial slices for the acquisitions of follow up (Figure 2.2); while the resolution is 1 mm x 1 mm x 6 mm with a field of view of 260 x 260 x 60 voxels for the acquisitions after the radiation treatment (Figure 2.1).
This is due to the fact that the two acquisitions are separated temporally, in terms of years from one to another, so the two images are separated mainly by new acquisition technologies and growth of the cerebral structures.
In Figure 2.1 and 2.2 there is an example of the data available for this study.

It is possible to observe how the two acquisitions are divergent in resolution, field of view and size of the brain structures.
In this study are involved also data from the Diffusion Weighted Imaging (DWI) acquisition, as the Fractional Anisotropy (FA) or Diffusion Tensor Imaging (DTI). Finally are also included data on the treatment plan and radiotherapy performed, as the information of dose imparted at the different structures (Figure 2.3).

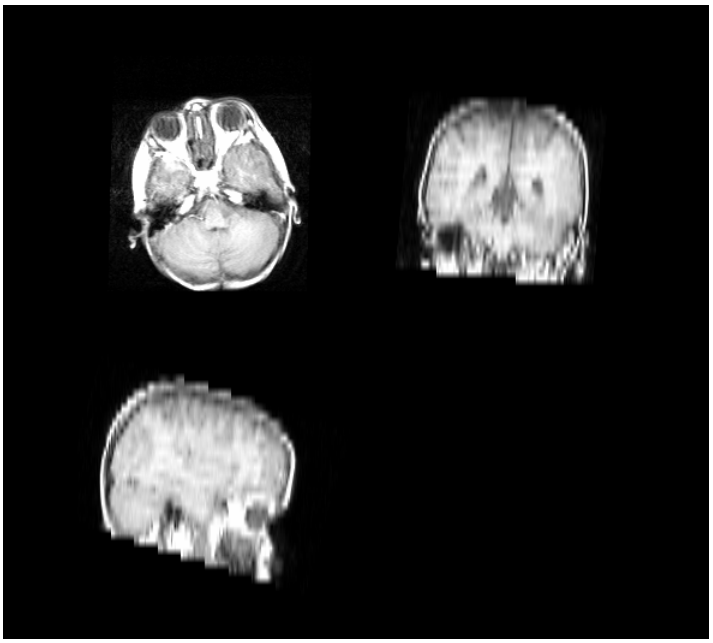

Figure 2.1: T1-weighted MPR Magnetic Resonance Image of a 4-years old patient after the radiation treatment, in transverse, coronal and sagittal view.

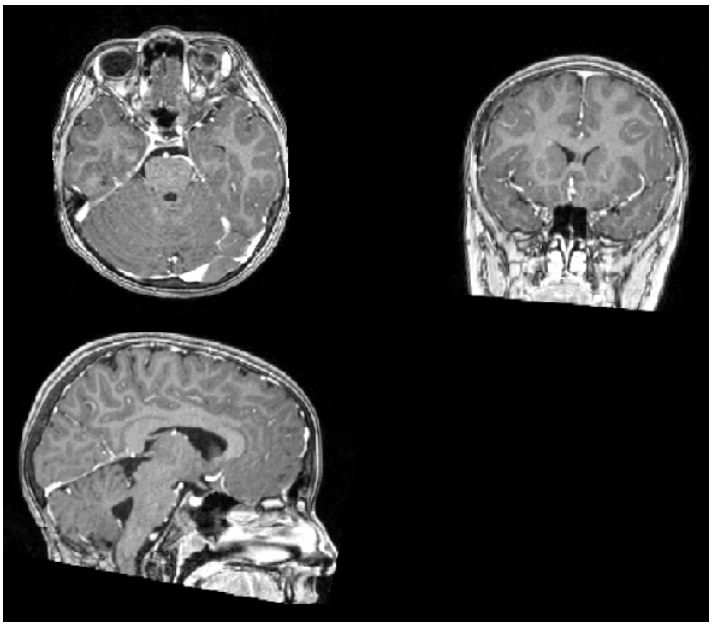

Figure 2.2: T1-weighted MPR Magnetic Resonance Image of a 10-years old patient after a follow up period from the treatment, in transverse, coronal and sagittal view.

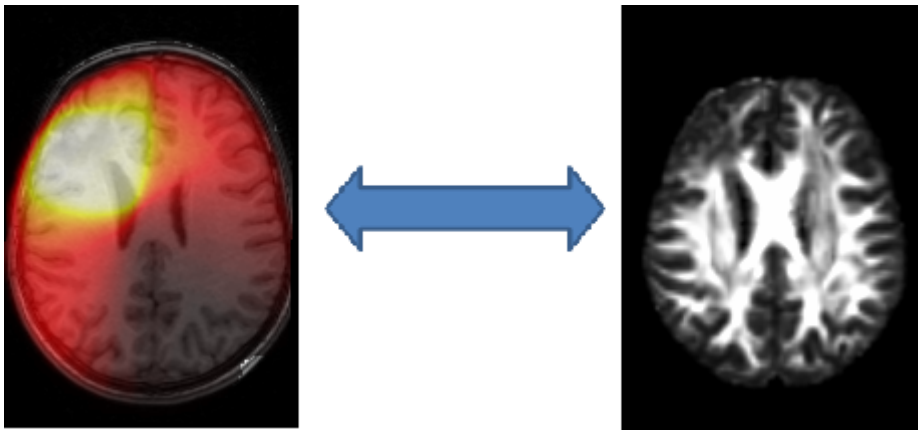

Figure 2.3: Left: MRI acquisition with integrated the information of radiation dose of a pediatric patient. Right: Fractional Anisotropy of the same patient.

2.3 Thesis objective

In this clinical context it emerged the importance to evaluate long-term RT-induced damages integrating different MRI data; we approached the problem by analysis of data of DTI with morphological sequence of Magnetic Resonance Imaging (MRI). Then the data obtained are merged with radiotherapy plans to test the relationships between locations, dose, distribution and shape of the treatment with detectable abnormalities in various brain structures, such as cerebral cortex, white matter and myelination of the beams.

This comparison is important to evaluate the correct development of the cerebral structures that received the radiation treatment and eventually the damages provoked by the latter.
The image registration, which is a process used to transform different sets of data into one coordinate system [52], seems to be a valuable tool to perform this task.

In this clinical study the need is to correctly register images acquired after the radiotherapic treatment to the Central Nervous System (CNS) with images acquired after a period of follow up of almost three years from the treatment, without relapses.
The passage of time between the two acquisitions adds furthers difficulties to the problem of registration, since it makes the images divergent in resolution, field of view but above all in the size of the structures of interest, due to the cerebral growth of the children (see Figures 2.1 and 2.2).
So this work try to evaluate the capability of the automatic registration algorithm proposed, to overcome these limitation, but also its reliability and robustness.

Particularly the topic of this work is the validation of an automatic algorithm of image registration for the correct alignment between post radiotherapy MRI of brain structures, and MRI of follow up of the same patients at distance of years.

Chapter 3

Image Registration

In general, Image Registration is "the process of transforming different sets of data into one coordinate system"; that is the determination of a geometrical transformation that aligns points in one view of an object with corresponding points in another view of that object or another object [52].
It is the process of finding a geometric transformation g between the two respective image-based coordinate systems that maps a point $\mathbf{x}$ in the first image set to the point $g(\mathbf{x})$ in the second set that has the same patient-based coordinates, i.e. represents the same anatomic location [53]. This notion presupposes that the anatomy is the same in the two image sets, thus the patient should not have undergone for example a surgical resection between the two acquisition.
However image fusion should be distinguished from image *registration*, which is a necessary first step before fusion can be successful.

The inputs of registration are the two images to be registered, that can be 3-dimensional (images acquired by tomography) or 2-dimensional images (X-ray projections). The output is a geometrical transformation, which is merely a mathematical mapping from points in one view to points in the second.
In a typical image registration process, an initial transformation model is constructed to align the moving image (that is the image that undergone the transformation) to the fixed image at first. Then the appropriate features are extracted from both images and the correspondences between these features are measured using 'similarity metric' to assess the quality of the alignment.

At last the optimal transformation is estimated by minimizing the similarity metric using an iterative optimization method and embedded in a hierarchical scheme. An image registration process is represented schematically in Figure 3.1.

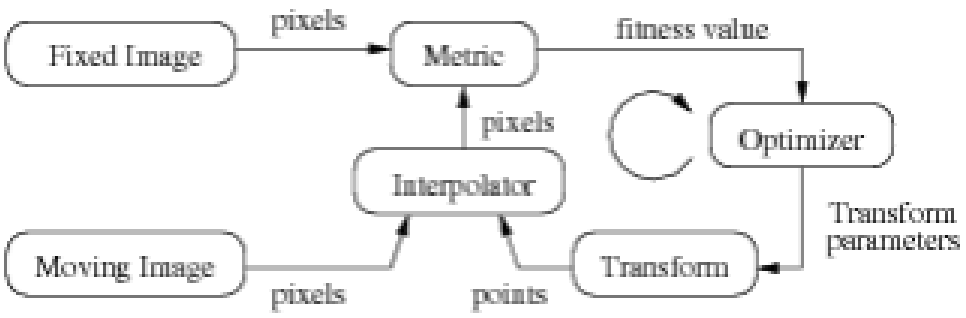

Figure 3.1: A flowchart of image registration algorithm.

The determination of points correspondence is a problem specific to the domain of objects being imaged.

There are many image registration methods, and they may be classified in many ways.
The method used in this work is based on **geometrical transformations** which refers to the mathematical form of the geometrical mapping used to align points in one space with those in the other.

3.1 Geometrical Transformations

These transformations map points from the space X of one view to the space Y of a second view [52]. The transformation T applied to a point in X represented by the column vector x produces a transformed point x',

$$x' = T(x) \tag{3.1}$$

If x' is equal, or approximately equal, to a point y in Y which corresponds to

x, the registration is made successfully. Any non-zero displacement $T(x) - y$ is a registration error.
The possible types of transformations are divided into two main classes: *rigid* or *non-rigid*.

Rigid transformations

Rigid mappings are defined as geometrical transformations that preserve all distances, straightness of lines and all non-zero angles between straight lines.
Rigid transformations are simple to specify with two components, a translation and a rotation. These transformations also preserve the straightness of lines (and the planarity of surfaces) and all non-zero angles between straight lines.
In Figure 3.2 is showed an example of rigid transformation.

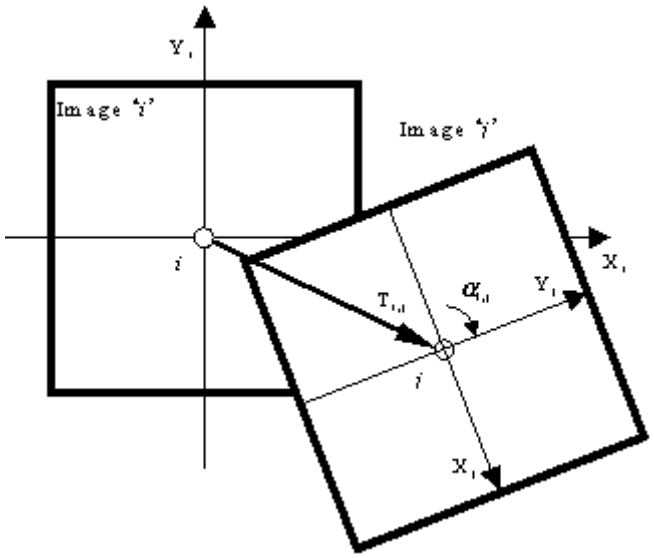

Figure 3.2: An example of rigid transformation.

Registration problems that are limited to rigid transformations are called *rigid registration problems*.
Rigid transformations are simple to specify; infact the translation is a three-dimensional vector $\mathbf{t}$ defined by three coordinates t_x, t_y, t_z relative to a set of x, y, z

Cartesian axes or by giving its length and two angles to specify its direction in polar spherical coordinates.
With this approach, if $\mathcal{T}$ is rigid, then

$$x' = R\mathbf{x} + \mathbf{t} \tag{3.2}$$

where R is a 3 x 3 orthogonal matrix.
These latter transformations both rotate and reflect rigid objects, so that, for example, a right-handed glove becomes a left-handed one.
The rotation of an object (as opposed to the coordinate system to which it is referred) about the x, y and z axes, in that order leads to

$$R = \begin{bmatrix} cos\theta_z & -sin\theta_z & 0 \\ sin\theta_z & cos\theta_z & 0 \\ 0 & 0 & 1 \end{bmatrix} \begin{bmatrix} cos\theta_y & 0 & sin\theta_y \\ 0 & 1 & 0 \\ -sin\theta_y & 0 & cos\theta_y \end{bmatrix} \begin{bmatrix} 1 & 0 & 0 \\ 0 & cos\theta_z & -sin\theta_z \\ 0 & sin\theta_z & cos\theta_z \end{bmatrix} \tag{3.3}$$

with the three matrices in the first line representing the rotations $R_z(\theta_z), R_y(\theta_y)$ and $R_x(\theta_x)$ about z, y and x, respectively.

Non-rigid transformations

Non Rigid transformation are important not only for application to non-rigid anatomy, but also for inter patient registration of rigid anatomy and intra patient registration of rigid anatomy when there are non-rigid distortions in the image acquisition procedure.
In all cases, it is preferable to choose transformations that have physical meaning, but in some cases, the choice is made on the basis of convenient mathematical properties.

The simplest non-rigid transformations are rigid except for scaling,

$$\mathbf{x}' = RS\mathbf{x} + \mathbf{t} \tag{3.4}$$

where $S = diag(s_x, s_y, s_z)$ is a diagonal matrix whose elements represent scale factors along the three coordinate axes.
In Figure 3.3 is reported an example of scaling.

Figure 3.3: Scaling transformation.

Such transformations may be needed to compensate for calibration errors in image acquisition systems. They are appropriate, for example, when gradient strengths are in error in MR.
The coupling of scaling with the rigid transformation is effective when registrations must account for erroneous or unknown scales in the image acquisition process.

The scaling transformations are special cases of the more general *affine* transformation,

$$\mathbf{x}' = A\mathbf{x} + \mathbf{t} \tag{3.5}$$

in which there is no restriction on the elements a_{ij} of the matrix A.
The affine transformation preserves the straightness of lines, and hence, the planarity of surfaces, and it preserves parallelism, but it allows angles between lines to change. In Figure 3.4 are represented different affine transformations.
It is an appropriate transformation class when the image may have been skewed during acquisition as, for example, when the CT gantry angle is incorrectly recorded.
The affine transformation matrix in *homogeneous coordinates*:

$$M = \begin{bmatrix} a_{11} & a_{12} & a_{13} & t_1 \\ a_{21} & a_{22} & a_{23} & t_2 \\ a_{31} & a_{32} & a_{33} & t_3 \\ 0 & 0 & 0 & 1 \end{bmatrix} \tag{3.6}$$

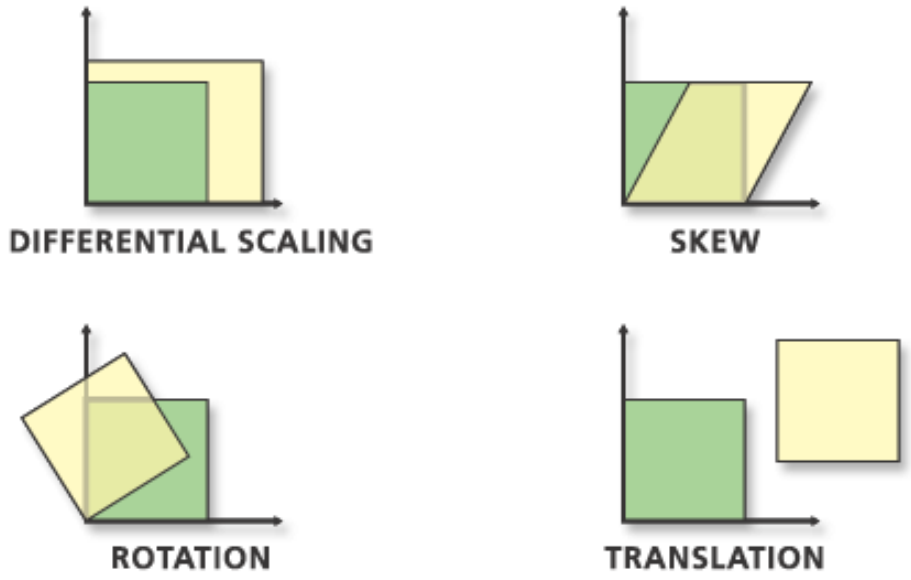

Figure 3.4: Affine transformations.

Curved transformations are those that do not preserve the straightness of lines.
In curved transformations the simplest functional form for $\mathcal{T}$ is a polynomial.

The most used polynomial function is the so called B-splines that is the short for "basis spline".
A function is represented as a linear combination of basis functions:

$$v(x) = \sum_i p_i \beta_i(x) \tag{3.7}$$

The kernel $\beta(u)$ is a piecewise cubic polynomial, for which the argument of the spline window is the sampled cubic B-Spline:

$$\beta^{(3)}(x) = \begin{cases} \frac{1}{6}(4 - 6x^2 + 3\,|x|^3), & 0 \leq |x| < 1 \\ \frac{1}{6}(2 - |x|)^3, & 1 \leq |x| < 2 \\ 0, & 2 \leq |x| \end{cases} \tag{3.8}$$

In Figure 3.5 and 3.6 there are an exemplification of the polynomial B-spline and the effect of the scaling factor of the polynomial, p_i.

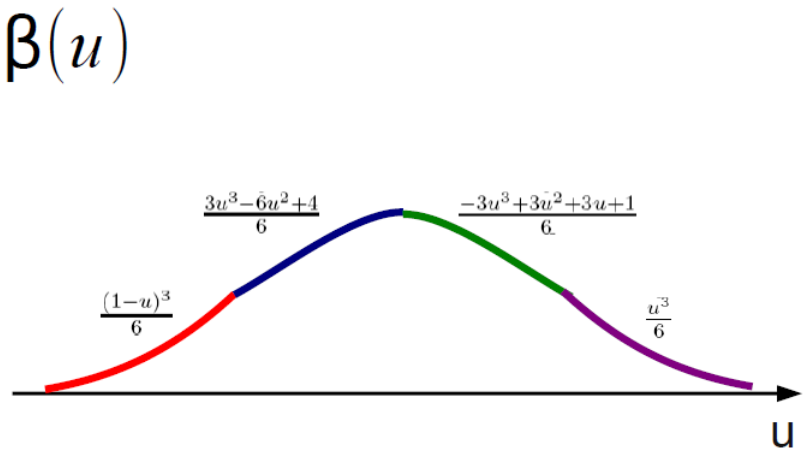

Figure 3.5: Representation of polynomial B-spline.

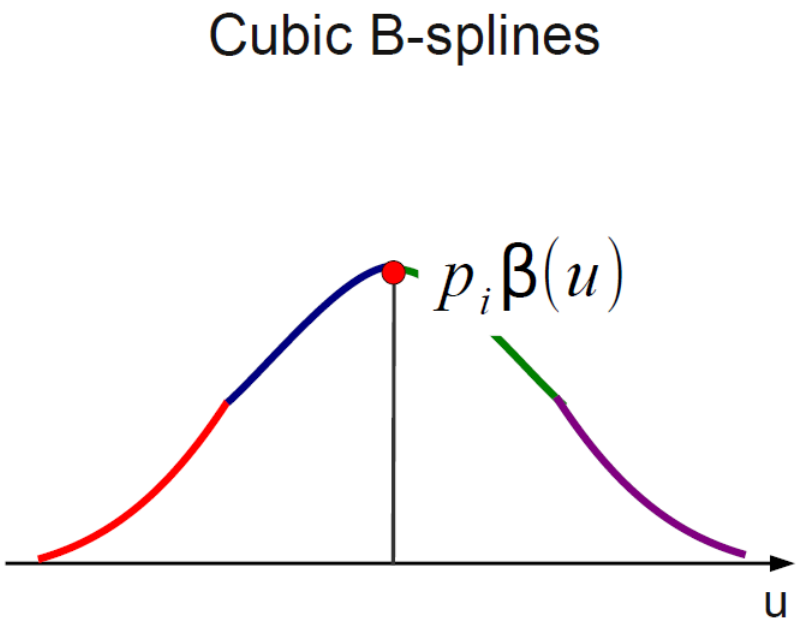

Figure 3.6: Representation of the effect of a scaling factor p_i on the cubic B-splines.

Finally through uniform cubic B-splines the function $v(x)$ could be represented as in Figure 3.7.

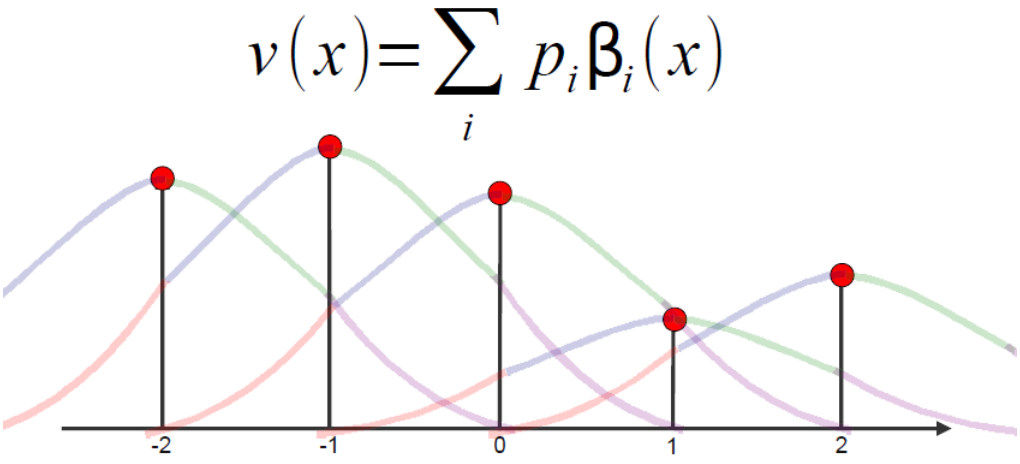

Figure 3.7: Representation of a function $v(x)$ estimated using uniform cubic B-splines.

In the same way, an image $f(x)$ could be described by a set of samples $f_i(x_i), x_i \in V$ on a Cartesian grid with integer spacing.
The calculation of $f(x)$ at points not on the grid requires an interpolation method based on the samples f_i and their location x_i.
In this context occurs the polynomial B-spline. So deformations are modelled on cubic B-splines using a grid of control points, as shown in Figure 3.8.

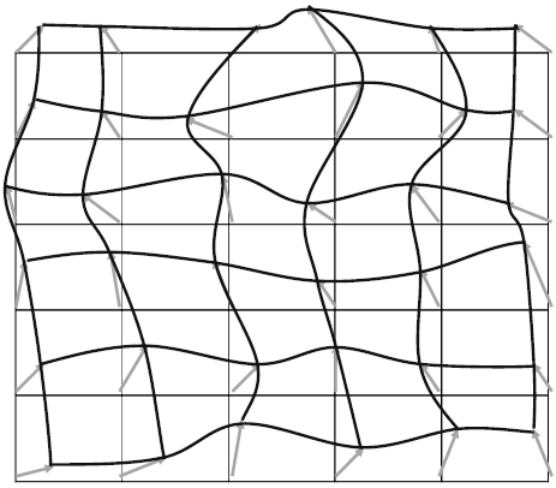

Figure 3.8: Representation of a warped image grid.

The description of a deformation is similar to that of the images; however, the deformation is defined on a much coarser grid.
A deformation is defined on a sparse, regular grid of control points λ_j placed over the test image and is then varied by defining the motion $g(\lambda_j)$ of each control point (Figure 3.8). Using a spline interpolation kernel to compute the deformation values between the control points produces a locally controlled, globally smooth transformation.
The spline deformation model is differentiable with respect to both the deformation parameters (necessary for computing the gradient of mutual information) and spatial coordinates (useful in other applications, for example estimating inverse coordinate mappings).

The resolution $\rho = [\rho_x, \rho_y, \rho_z]$ of the deformation determines the spacing of the grid and can be anisotropic.

The set of control points is a regular grid with spacings:

$$\Delta\rho = [\Delta\rho_x, \Delta\rho_y, \Delta\rho_z]^T \tag{3.9}$$

The (x, y, z) coordinates of the control points are stored in separate three-dimensional (3-D) matrices. Any $j = (t, u, v)$ element of these matrices has a location in the test image given by $[t\Delta\rho_x, u\Delta\rho_y, v\Delta\rho_z]^T$.
Each control point λ_j has an associated three-element deformation coefficient δ_j, describing the x-, y-, and z-components of the deformation. For a give ρ there will be $\left\|\rho\right\| = 3\rho_x, \rho_y, \rho_z$ deformation coefficients.
The deformation at any point $\mathbf{x} = [x, y, z]^T$ in the test image is interpolated using a cubic B-spline convolution kernel.

The transformation of the test image is specified by mapping reference image coordinates according to a locally perturbed rigid body transformation. Given a 3x3 homogeneous rotation matrix $\mathbf{R}$, a three-element transformation vector $\mathbf{T}$, and a deformation term $\mathbf{D}(\mathbf{x}|\ \rho)$, it is possible to apply non-linear transformation to the test image:

$$g(\mathbf{x} \mid \mu) = \mathbf{R}(\mathbf{x} - \mathbf{x}_C) - (\mathbf{T} - \mathbf{x}_C) + \mathbf{D}(\mathbf{x} \mid \rho) \tag{3.10}$$

where $\mathbf{x}_C$ is the location of the center of the test volume and $\mathbf{x}$ is any voxel location in the reference image. $\mathbf{R}$ is the rotation matrix, $\mathbf{T}$ is the translation vector, and ρ_j is the set of deformation coefficients.
The deformation is specified in the so-called *Vector Field*.

In Figure 3.9 there is a graphical representation of the concepts previously explained.

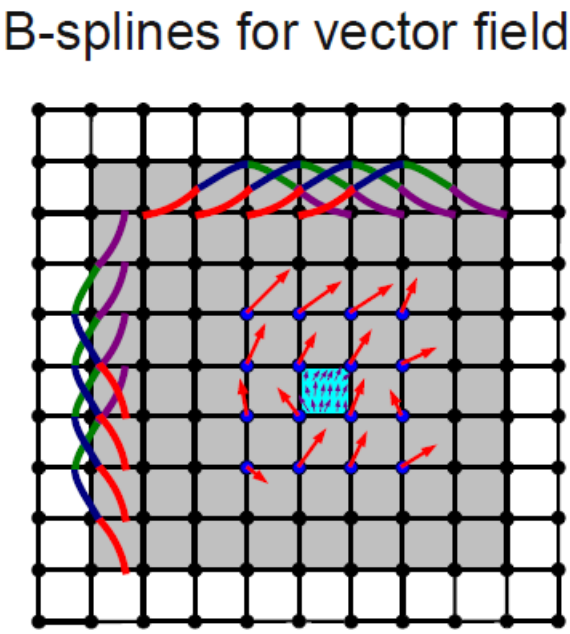

Figure 3.9: Representation on how a B-spline deformation field works on an image grid.

The registration algorithm includes also a metric of similarity between the two images and its optimizer.

3.2 Optimization Methods

Once the model has been formulated, an optimization algorithm can be used to find its solution.
The registration process is automated by varying the deformation in the test image until the discrepancy between the two images is minimized.
The optimization consists in finding local and global function extrema (maximization and minimization), so given a function f, which depends on several independent variables (parameters), the goal is find the minimum (or maximum) value of f [54].

There are different optimization methods implemented. For example the Amoeba or Simplex Method which operates as follows [55]:

- Pick initial simplex (e.g a geometric solid in N dimensions with N+1 vertices)
- Reflect highest vertex across other surface
- Repeat until highest point is not decreased
- Shrink simplex and start again

Figure 3.10 shows these passages.

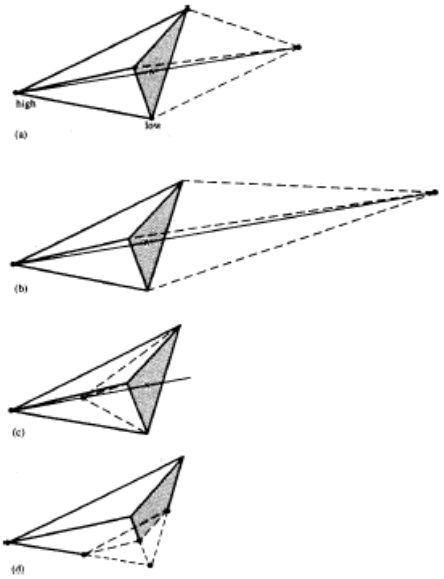

Figure 3.10: The Amoeba or Simplex method.

Another widely used method is that of the Steepest Descend (Figure 3.11) which:

- Minimize along each axis in turn
- Repeat until no improvement is found

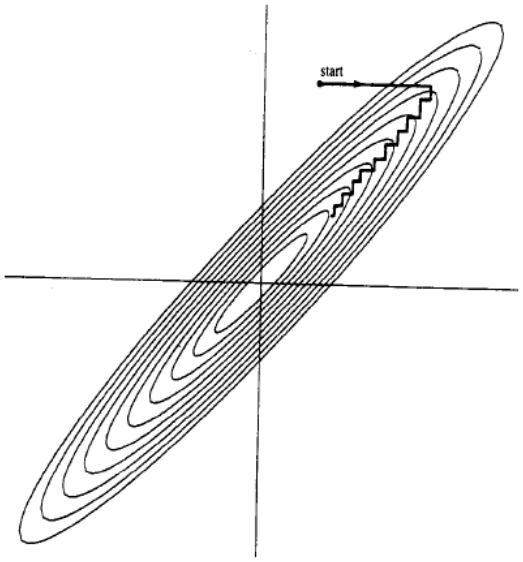

Figure 3.11: The Steepest Descend method.

The L-BFGS-B, instead, is a limited-memory, quasi-Newton minimization package, to reduce the cost function until termination criteria are satisfied.
Limited-memory quasi-Newton methods are useful for solving large problems whose Hessian matrices cannot be computed at a reasonable cost or are too dense to be manipulated easily [54].
These methods maintain simple and compact approximations of Hessian matrices: Instead of storing fully dense n x n approximations, they save just a few vectors of length n that represent the approximations implicit.
The main idea of this method is to use curvature information from only the most recent iterations to construct the Hessian approximation. Curvature information from earlier iterations, which is less likely to be relevant to the actual behaviour of the Hessian at the current iteration, is discarded in the interests of saving storage.
The latter optimization method is that implemented in the registration algorithm to validate in this study.

3.3 Metrics

The cost function to optimize could be vary depending on the images to register. The most widely used are *Mean Square Error* and *Mutual Information.*

The first one is used above all in case of monomodal image registration, because this metric do not take into account the information contained in the voxel, conveyed by its grey scale intensity.
In statistics, it measures the average of the squares of the "errors" which are the amount by which the value implied by the estimator differs from the quantity to be estimated [56]:

$$MSE = \frac{1}{n}\sum_{i=1}^{n}(\hat{Y}_i - Y_i)^2 \tag{3.11}$$

The mutual information instead depends on the probability distributions of the voxel intensities for the static and moving images [57]. It measures the mutual dependence of the two random variables X and Y [58]:

$$MI(X,Y) = \sum_{y\in Y}\sum_{x\in X} p(x,y)log(\frac{p(x,y)}{p(x)p(y)}) \tag{3.12}$$

where $p(x,y)$ is the joint probability distribution function of X and Y, and $p(x)$ and $p(y)$ are the marginal probability distribution functions of X and Y respectively.

It has been shown [59] that mutual information itself is not independent of the overlap between two images. To avoid any dependency on the amount of image overlap, it is preferred to use the normalized mutual information (NMI) as a measure of image alignment:

$$NMI(X,Y) = \frac{H(X)+H(Y)}{H(X,Y).} \tag{3.13}$$

where $H(X)$ and $H(Y)$ are the marginal entropies and $H(X,Y)$ is the joint entropy. For a random variable X with n outcomes, the Shannon entropy is defined as:

$$H(X) = -\sum_{i=1}^{n} p(x_i)log_2 p(x_i) \tag{3.14}$$

3.4 Validation of image registration

Validation is a very important post-step in registration algorithm development to make sure the clinical requirements can be met in the intended applications.
The registration techniques are generally categorized into two groups, rigid registration and non-rigid registration, according to the transformation model.
Although non-rigid deformation occurs much more frequently than rigid body deformation in reality, the development of non-rigid registration algorithms is impeded partly due to the difficulties in validation. Unlike the global rigid transformation, the non-rigid transformation is localized. That means some effective validation methods employed in rigid registration are not appropriate for non-rigid registration.
Moreover all Deformable Image Registration (DIR) evaluation procedures require the use of evaluation data and validation methods. These methods are several and can differ according to the evaluation parameters and the aspects taken into account for the assessment.
The following will present different approaches to validation of image registration.

3.4.1 Qualitative and quantitative assessment

The validation of image registration should be based on qualitative and/or quantitative assessment.
Obviously, the most straightforward validation method is visual inspection by experts, although it seems informal and unreliable.
However qualitative visual inspection is rough and can only be used as a routine preliminary validation approach. Thus it could be accompanied to quantitative validation for a more complete assessment.
As in this study, in the work of *Varadhan et al.* the validation of ITK free-form parametric deformable registration is made by taking into account both the aspects [60]. Infact they evaluate the good performance of the algorithm at first considering the anatomical correspondence between original and deformed image sets identified using markers or contours defined by the users. This qualitative validation is important because in radiotherapy clinical applications, the tumor and organs at risk (OAR) volume changes and, consequently, the partial volume dose received by these structures.

However they also considered quantitative parameters, a choice that has been made also in the study presented here. They used the mean squared error (MSE) as the metric to define the extent of mismatch between the original image A and the deformed registered image B, which is the normalized square difference between the two images A and B. For a perfect image match between images A and B, the MSE error is zero.
It is also computed the determinant of the Jacobian of the deformation field as a criterion for validating physical behaviour of deformation.

It is used frequently to gain information about the image transformation consistency, as in this study and in the work of *Iacono et al.*.
For the analysis, the jacobian operator was applied to the vector field in order to transform a 3D vector field into a 3D scalar image.
The jacobian operator is defined as follows [61]:

$$Jac_p(\Phi) = det(\Delta_p \phi) = \begin{vmatrix} \frac{\partial \Phi_x}{\partial x} & \frac{\partial \Phi_x}{\partial y} & \frac{\partial \Phi_x}{\partial z} \\ \frac{\partial \Phi_y}{\partial x} & \frac{\partial \Phi_y}{\partial y} & \frac{\partial \Phi_y}{\partial z} \\ \frac{\partial \Phi_z}{\partial x} & \frac{\partial \Phi_z}{\partial y} & \frac{\partial \Phi_z}{\partial z} \end{vmatrix} \tag{3.15}$$

It was defined as the determinant of the jacobian matrix of the deformation field. This operator links the local variation of an elementary volume in the floating image to the corresponding warped volume in the target image:

$\delta V_{target} = Jac_p(\Phi)\delta V_{floating}$

When $Jac_p(\Phi) > 1$ in P there is a local expansion, at the contrary when $Jac_p(\Phi) < 1$ there is a shrinkage in P; no transformation when $Jac_p(\Phi) = 1$.
In Figure 3.12 is shown an example of using the Jacobian to assess the evolution of malignant gliomas. In the study presented by this elaborate the Jacobian is used to estimate the deformation induced by brain growth.

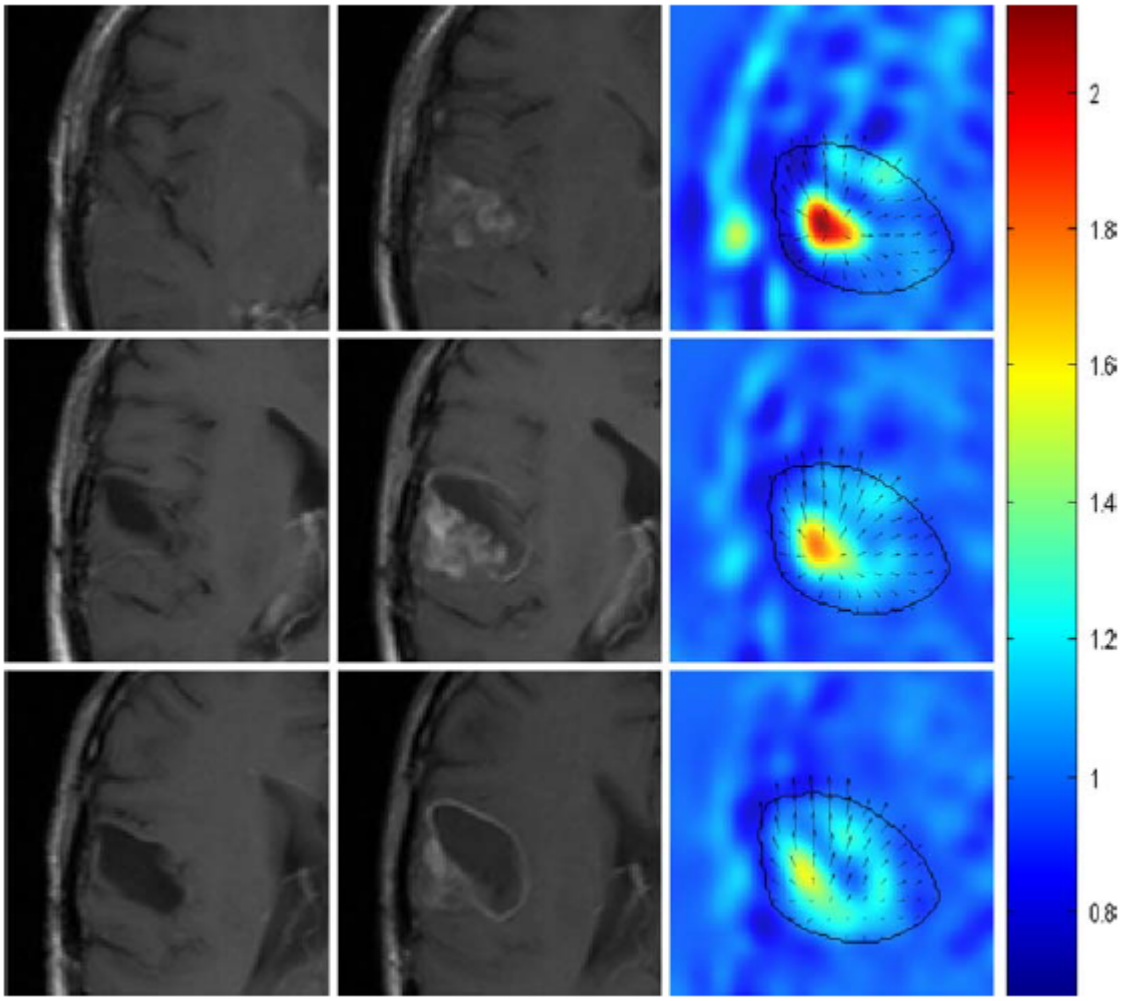

Figure 3.12: The first two columns represent the axial slices related respectively to target volume and floating volume. The last column on the right represents the different axial slices of the jacobian image and its value scale.

Another point in common between this study and that of *Iacono et al.* is the use of the same quantitative evaluation parameter.
They performed infact a quantitative validation by comparing the known vector fields $\mathbf{d(n)}$ and the estimated ones $\mathbf{s(n)}$ using *Mean Magnitude Error* defined as [62]:

$$MME = \overline{\|d(n) - s(n)\|}$$

In addition they also calculated the *Mean Angular Error*:

$$MAE = \overline{\|\angle d(n) - \angle s(n)\|}$$

MAE was computed considering both the azimuth and the zenith angles.
Mean Magnitude Error is used to evaluate the average difference between the applied vector field and that estimated by the registration, to quantify the error made by the algorithm.

3.4.2 Validation by the use of manual or automatic landmarks

A general validation technique could be based on manual or automatic identification of anatomical landmarks in clinical data.
In this study we do not use landmarks, because this validation method depends on the accuracy of the identification of homologous landmarks in two different images. Moreover the major drawbacks of both segmentation and landmark based validation methods are inter-observer variability while manually identifying landmarks or labelling volume of interest. In addition, it is time consuming to satisfy the demand of sufficient landmarks or segments.
An example of work which uses this method is that of *Kadoya et al.*, in which the locations of landmark points are labeled and the distance of corresponding points are calculated as validation metrics [63].
Figure 3.13 shows an example of manually identified landmarks on inhale and exhale images of the lungs.

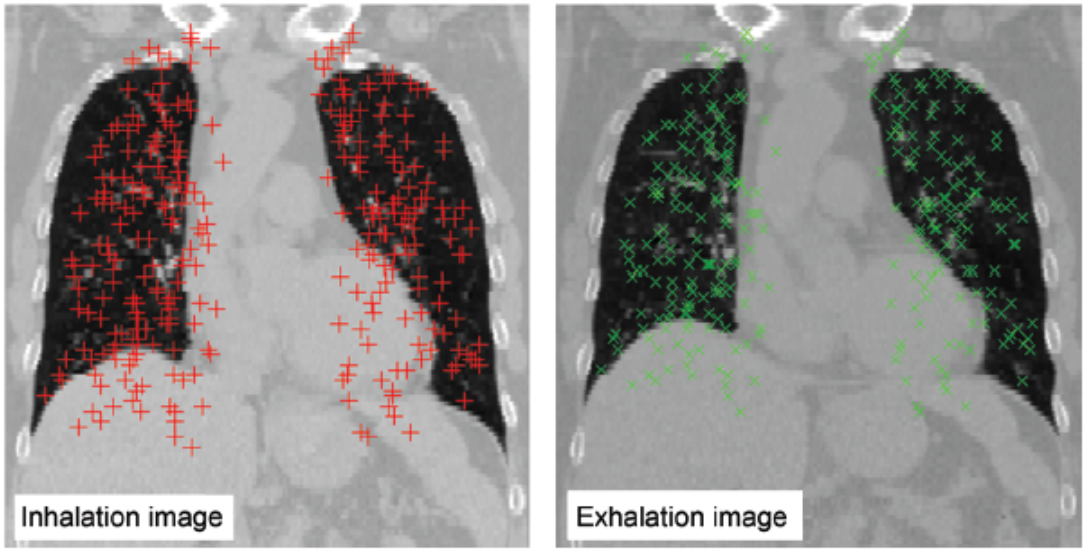

Figure 3.13: An example of inhale and exhale imaging with 300 landmark pairs.

They evaluated the accuracy of one commercially available and three publicly available deformable image registration (DIR) algorithms for thoracic four-dimensional (4D) computed tomography (CT) images. At first they manually calculated displacement vector field (mDVF) using the coordinate list. Then the automatically calculated displacement vector field (aDVF) was estimated by using DIR software.
However an analogy with this study is the validation of registration algorithm using the registration errors, in this case comparing mDVF and aDVF. Mean registration errors and 3D registration errors were quantified via the distance between the target and the source landmark.

3.4.3 Validation on phantom and real data

The validation could be performed on phantoms data or on real patients data. Digital simulation may give a clue that the spatial transformation model is likely to reflect the similarities of modeling assumptions between the simulation and the registration method. One of the main limitations is that the simulated deformations are not necessarily representative of the range of deformations present in real

patient data. So in this study it was chosen to use real patients data. Recently, more and more realistic and flexible phantoms are established which called hybrid phantom. The hybrid phantoms combine the realism of the patient-based voxelized phantom with the flexibility of the equation-based mathematical phantom. In Figure 3.14 is shown an example of physical and digital phantoms used to evaluate imaging performance.

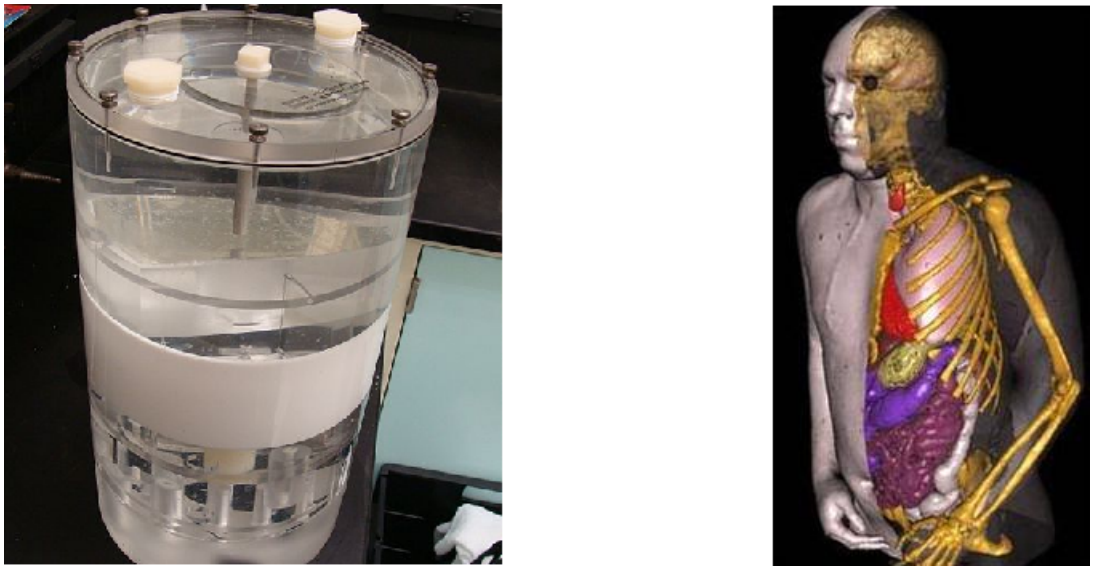

Figure 3.14: Left: An imaging physical phantom for determining CT performance. Right: Computational human phantom developed by RRMDG at Rensselaer Polytechnic Institute in Troy, NY.

3.4.4 Comparison with a gold standard

Once a registration method is validated with some degree of accuracy, it can be used for cross-validating other methods as a gold standard.
For example in the work of *Zambrano et al.* they evaluated the performance of their in-house-developed featurelet-based DIR algorithm against the iPlan® BrainLab treatment planning system (TPS) DIR software [60].
Also in this study they select a quantitative assessment of the quality of the contour propagation for the DIR algorithm. There were calculated the Dice's similarity coefficients, which measure the volume overlap percentage of the two images, as

follows:

$$DSC = \frac{V_s \cap V_t}{(V_s + V_t)/2} 100 \tag{3.16}$$

where Vs and Vt are the volumes of the source and the target structures, respectively.
However it is not an optimal validation strategy in practice, because it is hard to reproduce the conditions in the original validation to ensure its validity.
So in the work proposed by this elaborate the registration algorithm was not compared with a gold standard.

3.4.5 Evaluation of Plastimatch algorithm for image registration

In this context, it is important to cite a significant work by *Sharp et al.* since they evaluate B-Spline registration algorithm on the same open source software used in this study: *Plastimatch* [64].
However the difference with this study concerns the evaluation parameter used for the assessment.
It is applied to one of the most common clinical problem in which deformable image registration is used, that is pulmonary CT image registration.

To estimate the improvement of this algorithm in clinical applicability they used evaluation metrics of Dice coefficients and root mean squared error (RMSE) between the fixed and warped lung masks. This index gives an idea of the mean overlap between the two structure, although it cannot detect internal misalignments and finer errors [65].
Also for a further evaluation of the results they used visual inspection and the invertibility of the transformation. This was computed using the dilation measure, defined as:

$$D_i = \frac{d^2 u_i}{dx^2} + \frac{d^2 u_i}{dy^2} + \frac{d^2 u_i}{dz^2} \tag{3.17}$$

where u_i is the i-th vector in the deformation field. They measured the minimum dilation over all images within the lung mask.
A dilation value below -1 indicates the non invertibility of the vector field, which is to avoid.

These parameters showed that the method provides good alignment between the registered lung CT images. However, these statistics maybe not sufficient to indicate accurate registration on local structures.

At present, there are still few problems to be solved with validation of registration algorithms. First, absence of 'ground truth' transformation is still the major waist in registration validation. Second, none of the validated metrics can determine whether the accuracy of an algorithm is good enough for clinical applications. Clinically relevant validation metrics need to be developed. Third, validation methods are limited by their flexibility, and cannot be easily extended to validation of registration for other types of medical images.
Solutions to the registration accuracy validation problem in previously published papers can be classified using the criteria shown in Table 3.1.

Methodology	Ground truth	Data	Metric
Qualitative	Not used	Clinical Data	Not used
Quantitative	Synthetic transformations	Phisical phantom data	Target registration error
		Digital synthetic data	Target registration error
	Anatomical features	Clinical data	Average distance
			Volume overlap
	Not used	Clinical data	Consistency
			Intensity metric

Table 3.1: Classification of the validation methods.

3.5 Plastimatch image registration algorithm

In this paragraph the Plastimatch algorithm to validate is described.
It works in the way that the correct alignment of the reference image and the test image is performed assessing the more correct deformation process (in the form of strain tensor) that makes the two images visually different.
The vector field is defined on *fixed image* (reference image) and maps the latter to *moving image* (test image).

The images used for the registration are two T1-weighted MRI of the brain structures.
The image used as reference image is the MRI acquired after a period of follow up of almost four years after the radiation therapy, while the test image is the MRI acquired just after the treatment.
Thus the registration problem concerns two monomodal images (the information conveyed by the voxel is the same) but with difference in resolution and size of the structures to align.

At first an initial deformation between the images is estimated to initialize the process.
Thus the registration algorithm warp the moving image with this vector field to precisely overimpose to the fixed one, as exemplified in Figure 3.15.

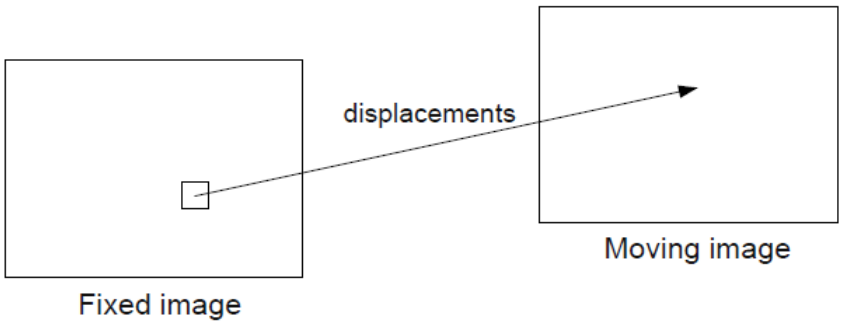

Figure 3.15: How the displacement is estimated by the algorithm between the fixed image and the moving image.

The moving image is warped with the estimated vector field (Figure 3.16), to coincide as much as possible to the fixed image.

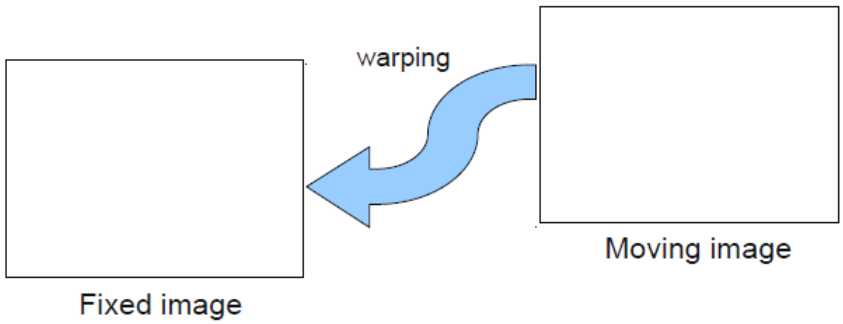

Figure 3.16: The correct direction of the warping performed by the image registration process.

Then it is calculated a cost function. In this study it was used the Mutual Information between the reference image and the warped image at each step, together with a second derivative regularization term:

$$C = MI(f, m) - \lambda c_{RM} \tag{3.18}$$

where f and m are respectively the fixed and the moving images, while λ is a scalar term which penalizes vector fields that are not smooth, weighting on a regularization term.
The regularization term used in plastimatch is the square of the vector field second derivative. For a vector field $u = (u_x, u_y, u_z)$, the regularization term is given as:

$$c_{RM} = \int c_{RM,x} + c_{RM,y} + c_{RM,z} \tag{3.19}$$

where

$$c_{RM,x} = (\frac{\partial u_x^2}{\partial x^2})^2 + (\frac{\partial u_x^2}{\partial y^2})^2 + (\frac{\partial u_x^2}{\partial z^2})^2 + (\frac{\partial u_x^2}{\partial x \partial y})^2 + (\frac{\partial u_x^2}{\partial x \partial z})^2 + (\frac{\partial u_x^2}{\partial y \partial z})^2 \tag{3.20}$$

The integration is generally defined to be performed over the domain of the fixed image.

The term λ is an input parameter of the algorithm used to trade off between image matching and vector field smoothness. Typical values of λ range between 0.005 and 0.1.
In this study it was selected a λ value of 0.05.

Subsequently the algorithm performs an optimization of the deformation previously estimated.
For the algorithm that we want to validate in this study, we used a non-rigid registration which estimates the deformation using a B-spline polynomial (see paragraph 3.1 for details).
So the algorithm performs an optimization of the B-spline coefficients:

$$v(x) = \sum_i p_i \beta_i(x) \tag{3.21}$$

Then it is computed the gradient of the cost function with respect to the P coefficients of the B-spline function β:

$$\frac{\partial C}{\partial P} = \frac{\partial C}{\partial v} \frac{\partial v}{\partial P} \tag{3.22}$$

The following flow chart (Figure 3.17) summarizes the logical steps of the algorithm.

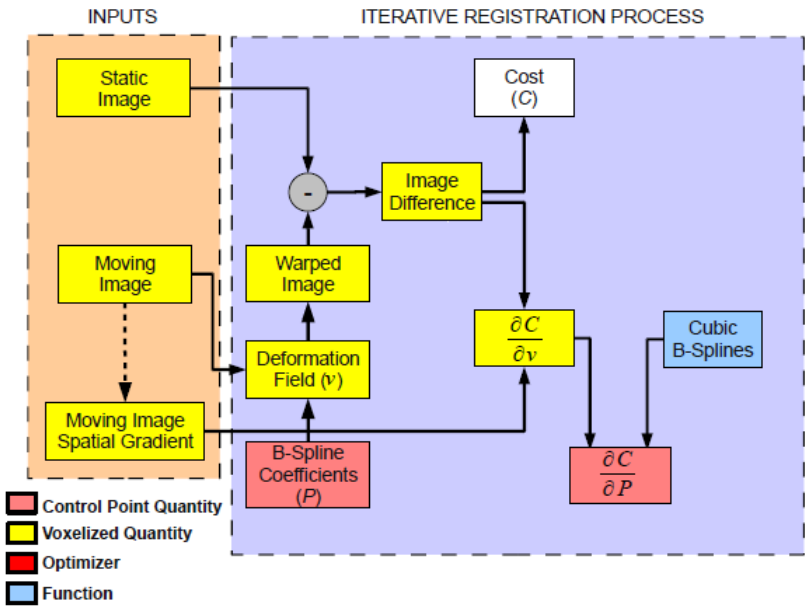

Figure 3.17: Flow chart of a registration algorithm in Plastimatch

Finally the optimization of the cost function is performed, enabling the update of the B-spline coefficients (e.g. the estimated vector field).
Another input parameter of the algorithm is the optimization method. It was used for the validation the Limited-memory quasi-Newton method.

It was made using a multi resolution approach, in order to avoid local minima and to decrease computation time.
Initially it is optimized for a deformation to recover the gross motion of the patient and large anatomic structures. As the resolution increase, there are recovered increasingly fine misalignments.
The complete process is shown in Figure 3.18.

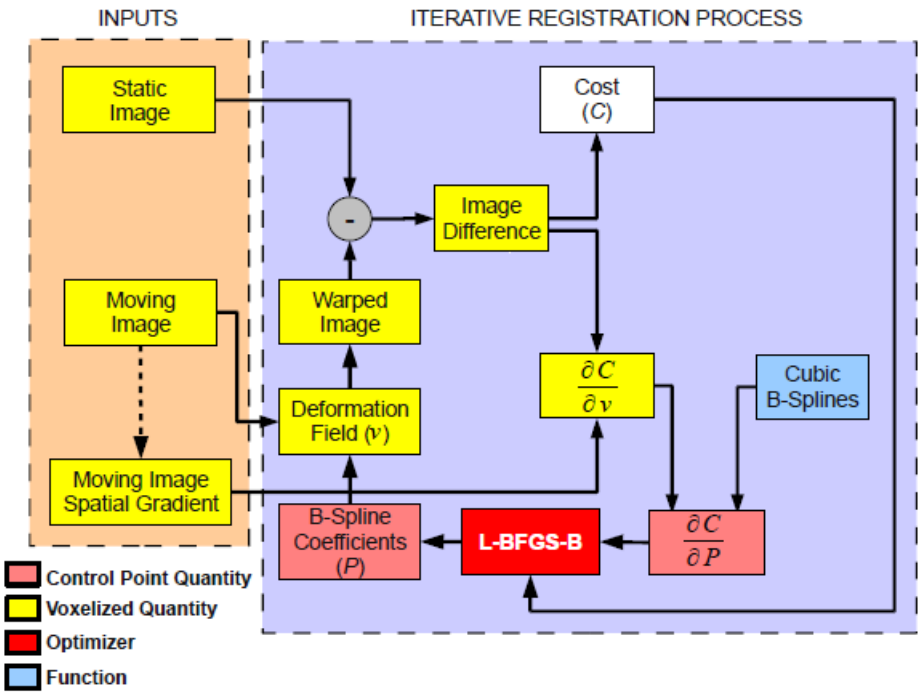

Figure 3.18: Flow chart of a registration algorithm in Plastimatch with the passage of optimization.

The algorithm stops when it reaches the maximum number of iterations (default 150) or the cost function is minimized (or maximized) over a threshold, that can be provided as an input parameter. In this study it is used the default maximum number of iteration.

To use this automatic algorithm it is necessary to create a command file specifying all the input parameters to do the registration, as shown in Figure 3.19.

```
# command_file.txt
[GLOBAL]
fixed=image_1.mha
moving=image_2.mha
img_out=warped_2.mha
xform_out=bspline_coefficients.txt

[STAGE]
xform=bspline
impl=plastimatch
threading=openmp
max_its=30
grid_spac=100 100 100
res=4 4 2
```

Figure 3.19: An example of a registration command file.

In the section `[GLOBAL]` are inserted respectively the name of the fixed and moving image, the name of the registered image and the file containing the spline coefficients.
Subsequently there is a section called `[STAGE]`.
The first indication of the stage refers to the form of the transformation to estimate (spline in this case), while the second refers to the type of implementation of the algorithm, Plastimatch or ITK.
The 'Threading' indicates the method used for parallel cost and gradient computations.
The last three informations concerns: the maximum number of iterations desired, the grid spacing and the resolution of the subsampling.
The grid spacing is the spacing between control points in B-spline grid which indicates the nodes on which it is estimated the deformation. The minimum spacing is 4*(Pixel Size) [66].
Finally the field 'res' indicates the subsampling rate for fixed and moving images to consider in each stage of the algorithm. In automatic mode, image is subsampled to the maximum rate which yields less than 100 voxels in each dimension.

It is also possible to do multi-stage registration using multiple `[STAGE]` sections.

Once the command file was created it is possible to run the image registration from the command line [1].

In this work it has been validated the consistence and affidability of the non-rigid spline registration algorithm using the following parameters, which have shown empirically to provide the best result in term of images alignment:

- L-BFGS method of optimization.
- Cost function based on Mutual Information (MI) and gradient regularization.
- Grid spacing of '60 60 60' (mm).
- Subsampling rate of [3 1] (mm).
- Regularization $\lambda = 0.05$.
- 64 bins.

The last parameter refers to the number of bins in which the histogram of the images is divided. It is used for plastimatch MI metric.

[1] The exact Plastimatch register command is: `plastimatch register command_file.txt`

Chapter 4

Validation

4.1 Method

The main issue of this work is the validation of the algorithm of image registration on Magnetic Resonance Images in pediatrics, which has been described in section 3.5.
It was verified if the algorithm used for the registration, is able to align correctly the corresponding cerebral structures represented on the two images, scanned at distance of years.

4.1.1 Validation of image registration algorithm

The validation framework performed in this study can be divided into three main phases:

i. Preprocessing: Creation of a test image by degradation of the reference images in terms of resolution, known deformation and noise.

ii. Registration process between the reference and the test image.

iii. Error estimation and computation of the evaluation parameters.

i) Preprocessing

The first step can be exemplified by Figure 4.1:

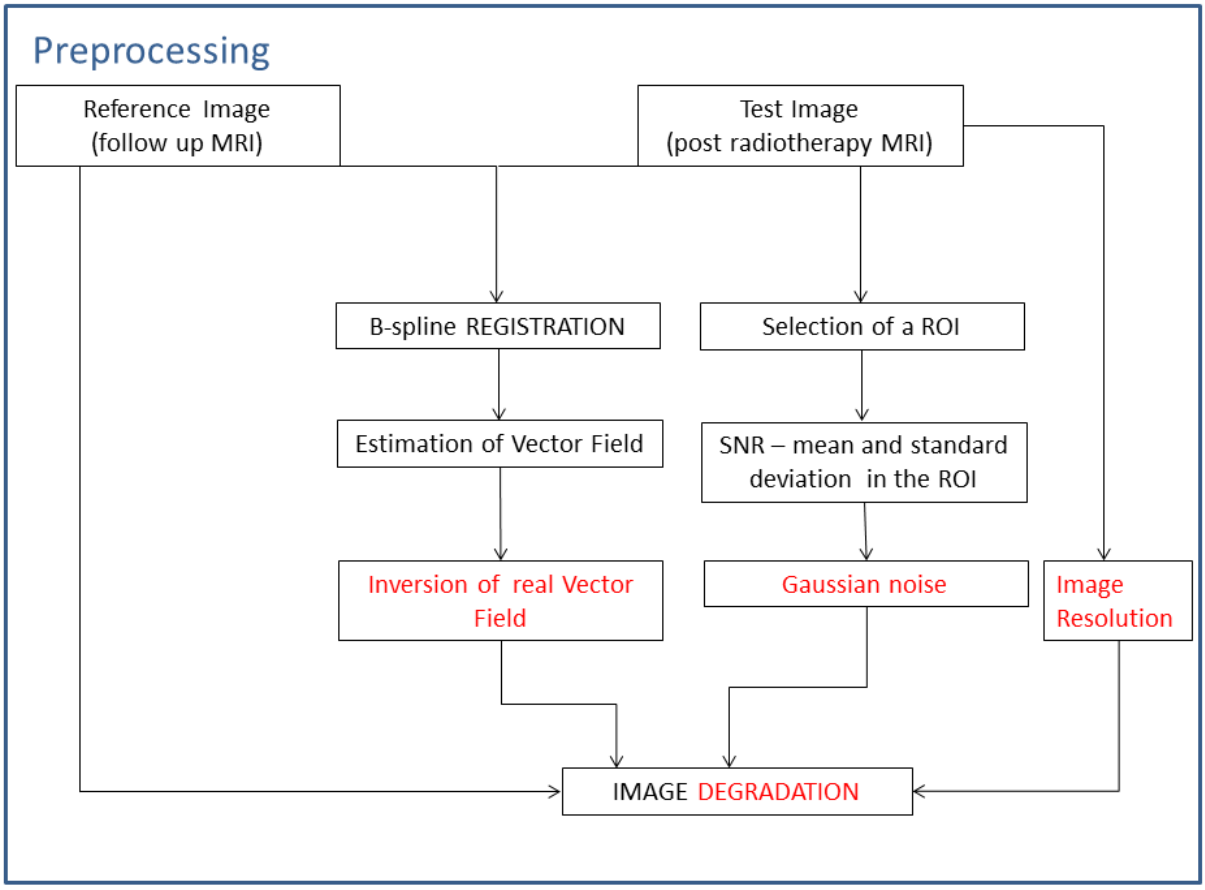

Figure 4.1: Flow chart of the first phase of the work.

For each of the ten patients included in the validation framework, the MRI acquired after their period of follow up was loaded in Matlab®, with an appropriate function taken from the tools for NIfTI and ANALYZE images available on MathWorks site [1] [67].

First of all it was inspected the header of the image (which contain all the information about the dimension of pixel in mm, the field of view, the origin of the coordinate system etc.) to gain more information on the image itself and have a more detailed view of the data available in this study.
In parallel the same images were visualized and inspected using the software MRIcro.

The same was done with the MRI acquired after the treatment of radiotherapy.
There were also visually appreciated the differences between this image and the previously mentioned image (MRI of follow up), that were scanned at distance of years.
It was then became concretely aware of the problem of registration between the two images, different in size of the brain structures and resolution.

To implement the preliminary part of the preprocessing (Figure 4.1), it was extracted from one patient a real deformation field, to simulate a possible brain growth.
We proceed as follows:

- It was registered the reference image (follow up MRI) of the patient randomly selected, and the test image (post radiotherapy MRI) of the same subject using the software Plastimatch and a multistep approach.

- The vector field in output is then inverted to obtain a vector field[2] available

[1] The name of the proper Matlab function is: `load_untouch_nii(filename)`

[2] The vector fields used are five dimensional. This is due to the fact that the images are three dimensional, so there is a 3D matrix which indicates the displacements of each voxel along the x coordinates, one matrix for the y coordinates and one for the z, that express the new position of each voxel of the image. Finally this four dimensional vector has these values concatenated in the fifth dimension.

to warp the reference image of all patients and regain the test image.
This inversion of the tensor is necessary because the registration algorithm estimates the deformation that warp the so called 'moving image' (test image) to be fully aligned with the 'fixed image' (reference image); however in this study the reference image is the "final" image with the cerebral growth, while the test image represents the same structures years before. See Figure 4.2 to better understand this fundamental passage.

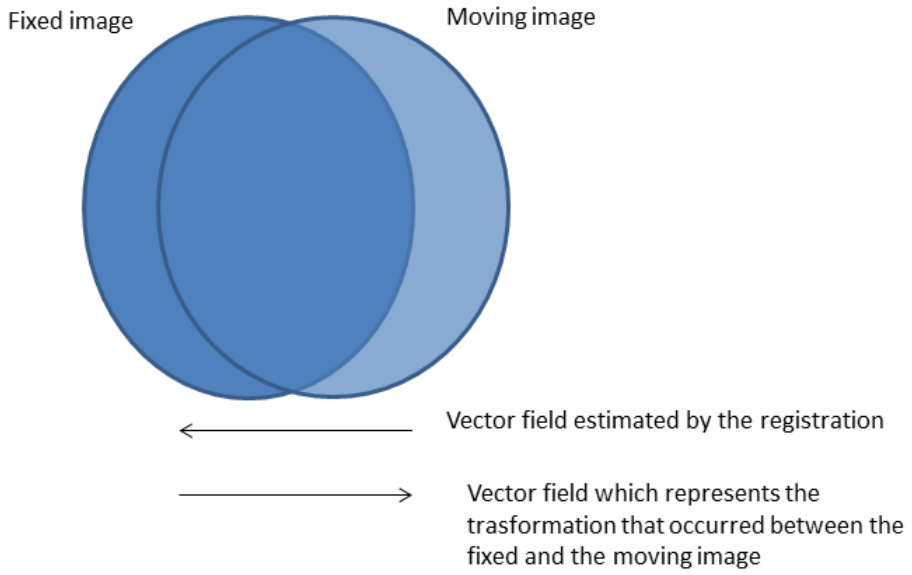

Figure 4.2: The vector field estimated by the registration and the one used to warp all the reference images are inverted.

The inversion described was made loading in Matlab® the vector field in NIfTI format[3].
Then it was reversed the sign of the matrix which represents the vector of deformation and it was resaved still in NIfTI format, with the matrix equal in magnitude but with opposite direction.

- The vector field thus obtained, was used to warp all the reference images of the ten pediatric patients and used as a reference transformation to compare all the deformations estimated by the registration process.

  The deformation of the images was made using Plastimatch and its command: `warp`. This command allows the user to warp an input file (image, dose volume or set list file) with a given transformation (differents formats are available), obtaining an output file that could be the deformed input or still a vector field (see Appendix C).

In Figure 4.3 there is an example of a reference image with the vector field used for the warping.

[3]It was used in this work a NIfTI format also for the vector fields, although there are other formats to store this type of file, for example the *mhd*. This is due to the fact described also in Appendix B, of the more flexibility and adaptability of the NIfTI format to different tools and programs. Infact it has been noticed a problem of management and difficulty of handling the data in *mhd* format. Hence the choice of the NIfTI.

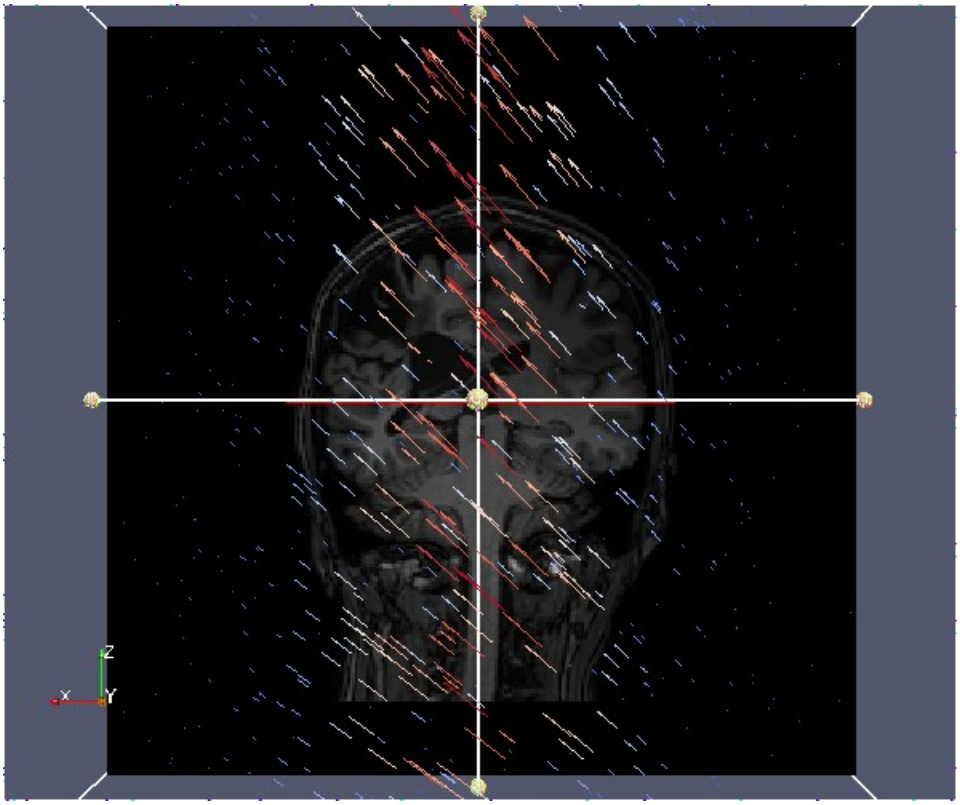

Figure 4.3: A brain MRI with the vector field used for the warping (arrows).

Then this deformed image was also degraded in resolution to reach the conditions of the image scanned years before.
So the original resolution of the image (0.5 x 0.5 x 1 mm) has been imposed on 1 x 1 x 6 mm.

Subsequently this transformed image, was also corrupted by known additive noise to create the worst condition of image registration.

At first a Region of Interest (ROI) was selected on the test image of the same patient chosen for the extraction of the vector field and the signal-to-noise ratio computed in the ROI.
The signal-to-noise ratio computed in this ROI was finally used to generate a Gaussian curve of the noise defined by the mean and the standard deviation previously evaluated.

The mean and standard deviation obtained are respectively 14.58 ± 6.295, rounded to 15 ± 10 for simplicity; so the noise used is $\sim \mathcal{N}(15, 10)$.

Finally the noise thus created was added to the previously deformed and degraded image, concluding the preprocessing phase.

In Figure 4.4 there is an example of a deformed and degraded MRI joined to the same but with additive noise; below their respective histograms are also reported.

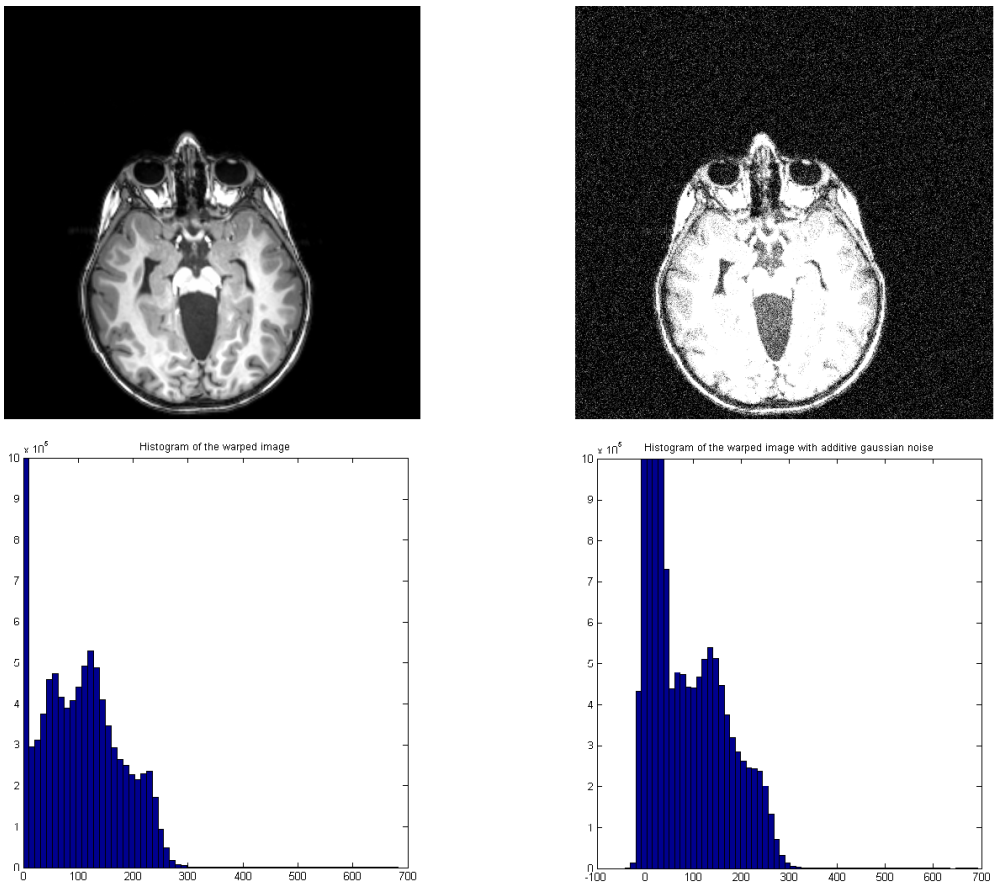

Figure 4.4: A follow up MRI warped and the same noisy image. Under the images are reported the respective histograms. It is possibile to note how the additive Gaussian noise does not alter the shape of the histogram but alters only the mean and standard deviation of the distribution.

ii) Validation framework

The second phase of the work is focused on image registration that is the process to validate in this study.
The detailed description of the registration algorithm to validate is reported in section 3.5.

The flow chart in Figure 4.5 exemplifies the steps done in this phase.

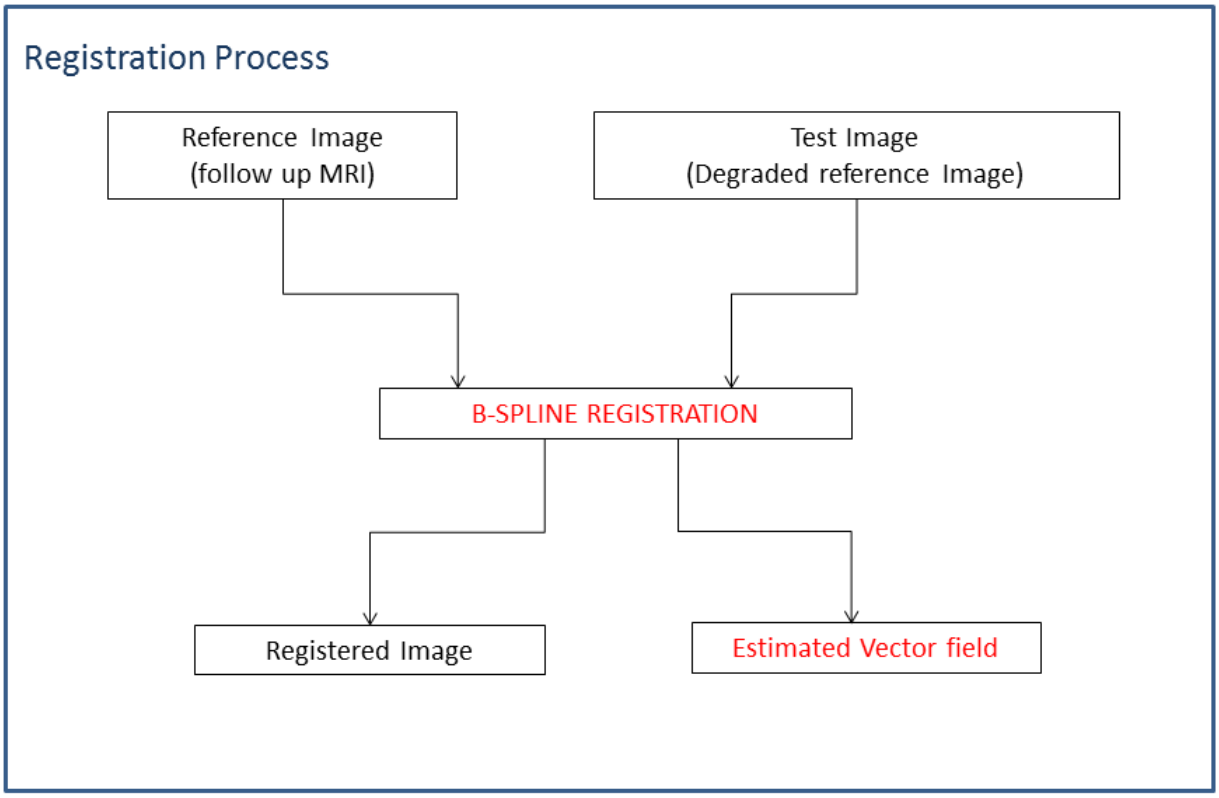

Figure 4.5: Flow chart of the registration framework.

To evaluate the non rigid registration in Plastimatch it was built up an algorithm in Matlab® to automate tasks.

Problems

Before starting the registration between the reference image and the previously test image for all patients, some preliminary operations were made due to some problems we noticed.

- First of all it was implemented a function in ITK[4] (`resliceto`) which try 'to fix' the MRI acquisition on an image mask specifically created. This operation allows the user to set manually the center and the dimension of an image.
  This passage was made so that the different software used for image processing (Plastimatch and Matlab®) can not change the center of the images, altering the proper application of the vector field.
  So in Matlab® it was created a mask to use as a fixed image, generating a matrix of zeros of the desired dimension. Then this matrix was converted in *.nii* format [5] with an image center imposed.
  Once generated, this mask was used by the '`resliceto`' to fix on it an image.

- Before register the two images it was also rescaled the histogram of the warped image.
  This is due to the fact that the original histogram of the image is in a range between 0 and 620, not enough to generate appreciable variations in the levels of Gaussian noise.
  Thus it is rescaled the histogram in a range 0 - 2000.
  Figure 4.6 shows this rescaling on the histogram.

[4] This is an open-source, freely available software system for 3D computer graphics, image processing and visualization. It consists of a C++ class library and several interpreted interface layers [68].

[5] The Matlab® function of the NIfTI tool for this task is: `make_nii`.

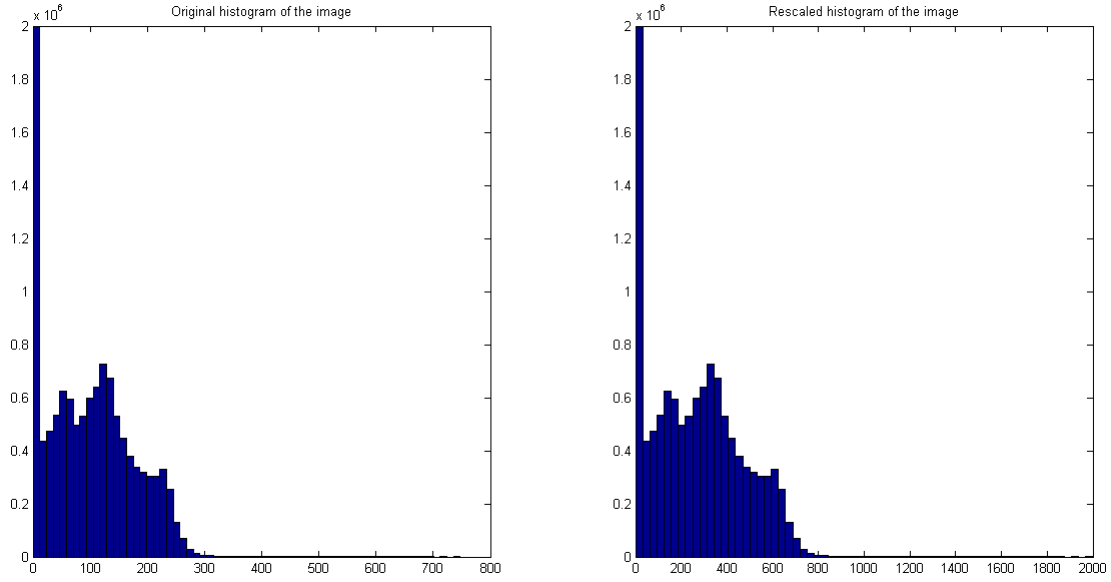

Figure 4.6: The left histogram is that of the image after the warping, while the right one is the histogram after the operation of rescaling. It is possible to observe the same shape of the distribution but an expansion of the range of values.

Features of the algorithm

Seven levels of noise were added to the images.
To increase the level of noise, the normal distribution which was created is multiplied by a scalar which amplifies gradually the effect of noise on the image.

It was decided to impose seven levels of rescaling from 0.5 to 3.5 with a step of 0.5, to test the consistence and the behaviour of the registration algorithm with increasing noise (from half to three times amplified).

At the end of this task the degraded and noisy image was saved as test image for the following processes of registration.

To improve the return of the non-rigid registration and optimize the estimate of the vector field, at first four consequential rigid registrations were performed to initialize the alignment of the images. The parameters selected for these preliminary registrations are less restrictive in terms of accuracy of the result and of lower computational cost.
The first one is that of 'Align_center' which, as the name suggests, operates an alignment of the centers of the two images.
So there are used:

- Subsampling rate=1.
- 20 bins.
- Grid spacing of '40 40 40'.
- Regularization $\lambda = 0.0005$.

The output file was given as input to update the subsequent command file.

The second rigid registration performed is the 'Translation', which provides 3 degrees of freedom to warp the moving image for the correct alignment, preserving angles between lines and distances between points.
The parameters used in this case are:

- Subsampling rate=[10: -1: 1].

- 512 bins.
- Grid spacing of '40 40 40'.
- Regularization $\lambda = 0.0005$.

The last registration done for a good initialization and estimation of macro misalignments is the 'Affine'.
This transformation used 12 degrees of freedom; it does not necessarily preserve angles between lines or distances between points, but it preserves ratios of distances between points lying on a straight line.
The parameters selected are:

- Subsampling rate=[6: -1: 1].
- 64 bins.
- Grid spacing of '40 40 40'.
- Regularization $\lambda = 0.0005$.

After this macro alignment of the two images, the image registration to validate is performed.
Using an elastic transformation it is possibile to integrate a deformation model with the 12 degrees of freedom of the affine transformation matrix, thus improving the capability of deformation and correctly registering the two images.

Workflow

The function created to implement the validation framework performs as follows:

1. The image is loaded and 're sliced' on a mask.

2. Once this preliminary operation was done, the algorithm performs image resolution degradation and the warping of the image with the known vector field previously described.
   Infact, although they have been exposed in the preprocessing phase, it has been chosen to incorporate the operations of deformation and addition of noise in this macro algorithm to avoid having to do it manually on all patients.

3. The histogram of the image was then rescaled in order to add the Gaussian noise.

4. Within a 'for cycle' for the different levels of noise rescaling, it was added the Gaussian noise on the previously deformed image, thus creating the test image for the registration.

5. Image registration.

The passages of the algorithm previously described are iterated for three times exactly equal.
This was done to validate not only the accuracy of the automatic registration algorithm but also the repeatability of the results.
So for each patient 21 non-rigid registration are executed, three for each level of noise scaling. Thus considering all the patients included in this study, the total number of registration performed for the validation of the registration algorithm amount to 210.

In output the algorithm provides the registered image (e.g. the moving image warped with the estimated vector field) and the vector field estimated by the image registration.

iii) Error Estimation

The third and final phase of the validation framework could be summarized by Figure 4.7.

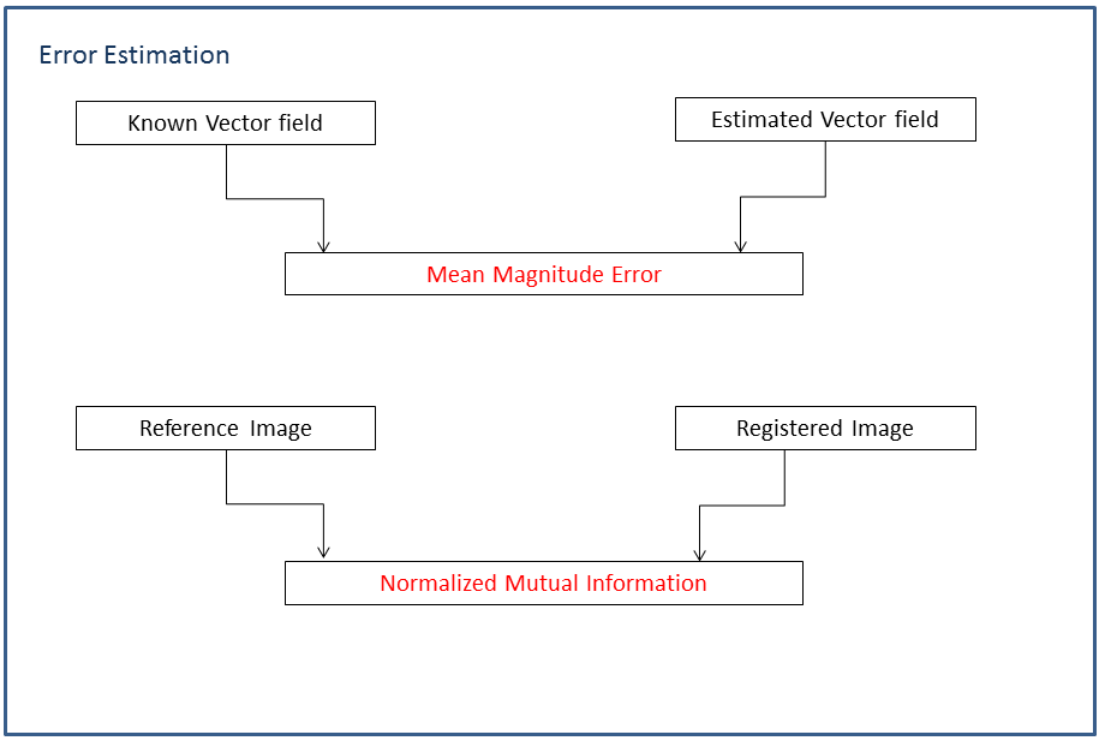

Figure 4.7: Flow chart of the final phase of the validation framework.

This phase concerns the elaboration of data obtained from previous operations, and computation of the results.

An evaluation parameter used to assess the good performance of the image registration algorithm, is the so called *Mean Magnitude Error* (MME).
It considers the known vector field, used to warp images, and the estimated one by the registration algorithm.
MME is defined as:

$$MME = \overline{\|d(n) - s(n)\|}$$

where **d(n)**is the known vector fields and **s(n)** is the estimated one by the registration process.
It measures the misalignment between the two vector fields in *mm*. If the algorithm performed well, MME is very low, tending to zero.

First the known vector field and the estimated one are loaded as NIfTI format.
The 5-D matrix obtained for each vector is then divided in three different matrices of the same size of the image from which it was estimated, containing the deformation values in the three directions of 3-D space (x, y, z). Then it was computed the punctual norm of the difference of the values contained in the matrices previously generated[6].
Finally the mean of these values of punctual norm was computed, obtaining a single parameter that quantify the error, for each registration performed.

The error is expressed in *mm* and indicates the medium misalignment in *mm* committed by the algorithm of image registration.

The other parameter considered for the validation of the algorithm, is the Normalized Mutual Information (NMI, see paragraph 3.3).
NMI quantify the similarity of two images and it was estimated between the reference and the registered image to know if they are almost the same, thus indicating the good performance of the registration.

Brain Extraction

The evaluation parameters (Mean Magnitude Error and Normalized Mutual Information) were computed after the operation of brain extraction from the images with an apposite tool.

[6]**Note:** In this case it was computed the sum of the two vector fields, instead of the difference, due to the opposite direction of these deformations. Infact the known vector field describe the deformation given to the reference image to generate the warped image. The estimated one, instead, describe the deformation which refers the warped image to the reference one. So their difference is the algebric sum (refer to the Figure 4.2 for furthers details).

The Brain Extraction Tool deletes non-brain tissue from an image of the whole head (see Appendix D).
This task was made using the software *MRIcron* with the FSL library and the apposite command `bet`.

It was selected to generate a binary brain mask. Then with this mask multiplicated to the entire image only the brain was extracted, by thresholding the image and preserving only values greater than zero (see Figure 4.8).

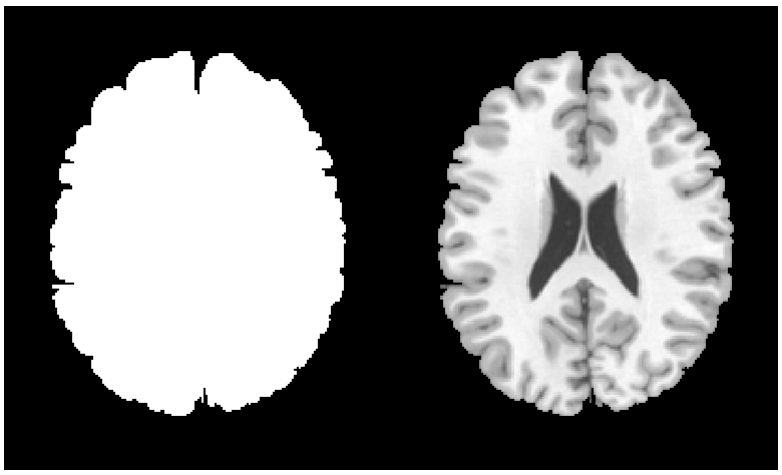

Figure 4.8: On the left there is an example of binary mask generated with the command 'bet'. On the right the brain extracted with the binary mask from a MRI.

Finally it was calculated the Mean Magnitude Error and the Normalized Mutual Information as previously described, but only considering the brain area which is the area where it is very important to properly register the images.

4.1.2 Input parameters optimization

Moreover it was decided to evaluate how the registration algorithm performs at the variation of input parameters, thus trying to estimate the optimal setup for each parameter.
The investigated parameters were:

- Bin levels
- Grid dimensions
- Regularization lambda

The evaluation parameter used is Mean Magnitude Error, as in the previous validation framework.

A follow up MRI of a patient among those included in the study was selected as reference image (Figure 4.9).

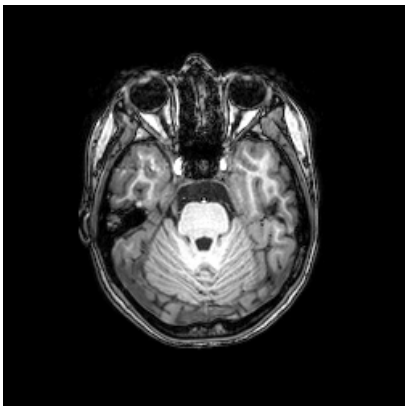

Figure 4.9: A template MRI of a patient used for the validation of the registration parameters.

This image was manually warped with IRTK to simulate a natural cerebral growth, as in the previous section, thus generating the test image.
The warping was made using the 'Transformation Editor' available in IRTK, as shown in Figure 4.10.

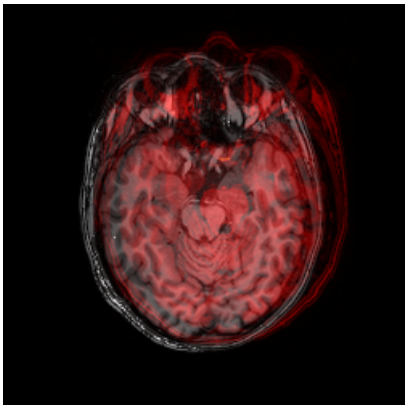

Figure 4.10: The reference image represented in grayscale and the manually warped one in red.

The two images are then registered with B-spline Plastimatch registration to extract the vector field to be applied during the validation and to be used as reference.
The parameters used for this registration were the same used also for the validation framework (see section 3.5).

The vector field estimated was then inverted in Matlab® and used to warp the reference image with Plastimatch, thus obtaining the test image (see the previous section for further explanation on this passage).

Then for each of the three parameters tested the workflow implemented is:

1. Selection of the values to test.
2. Registration between the reference and the test image with the parameters selected.
3. Computation of Mean Magnitude Error in the brain area.

These parameters were tested separately keeping unchanged the others, that were fixed to the same values used for the validation.
We tested ∼15-20 different values for each of the three input parameters, thus performing a total of ∼60 registration.

4.2 Results

In this section are presented the results obtained from the previously described work.

Figure 4.11 exemplifies on a brain MRI of a patient, the validation framework applied: It is possible to see the process of degradation of a reference MRI with the known vector field and the additive Gaussian noise, comparing two different levels of noise. The figure also shows the output of image registration between the reference and the degraded image.
Qualitatively a slight worsening of the result in term of image alignment for the registration with high level of noise on the test image can be observed. The following results will quantify this observation.

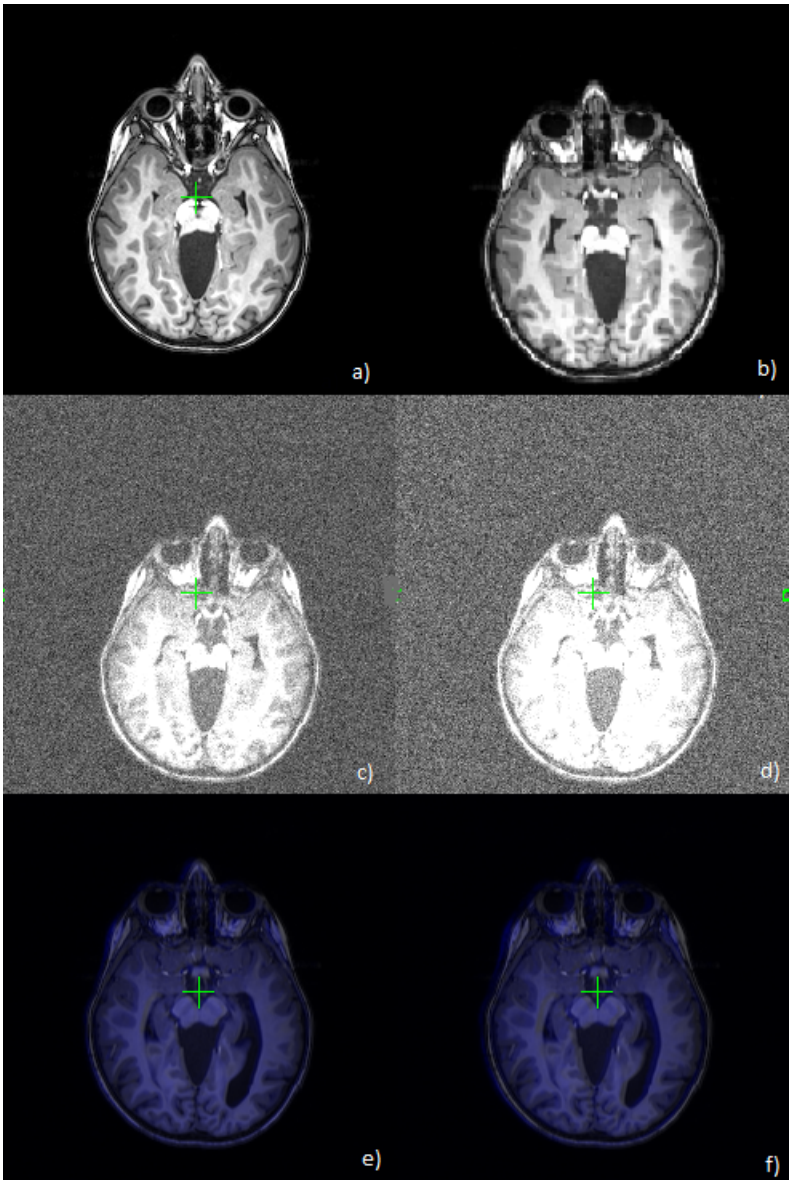

Figure 4.11: In Figure a) is shown the reference image of a patient. In Figure b) is presented the reference image of Figure a) warped by the known vector field and degraded in resolution. Figure c) represents the warped image with lowest level of additive Gaussian noise while Figure d) shows the warped image with additive noise at the highest level. Finally Figure e) and f) represents the overlay between the reference image (gray) and the registered one (blue) respectively for low level and high level of noise.

4.2.1 Validation of Image Registration algorithm

Figure 4.12 shows the results found for each patient.

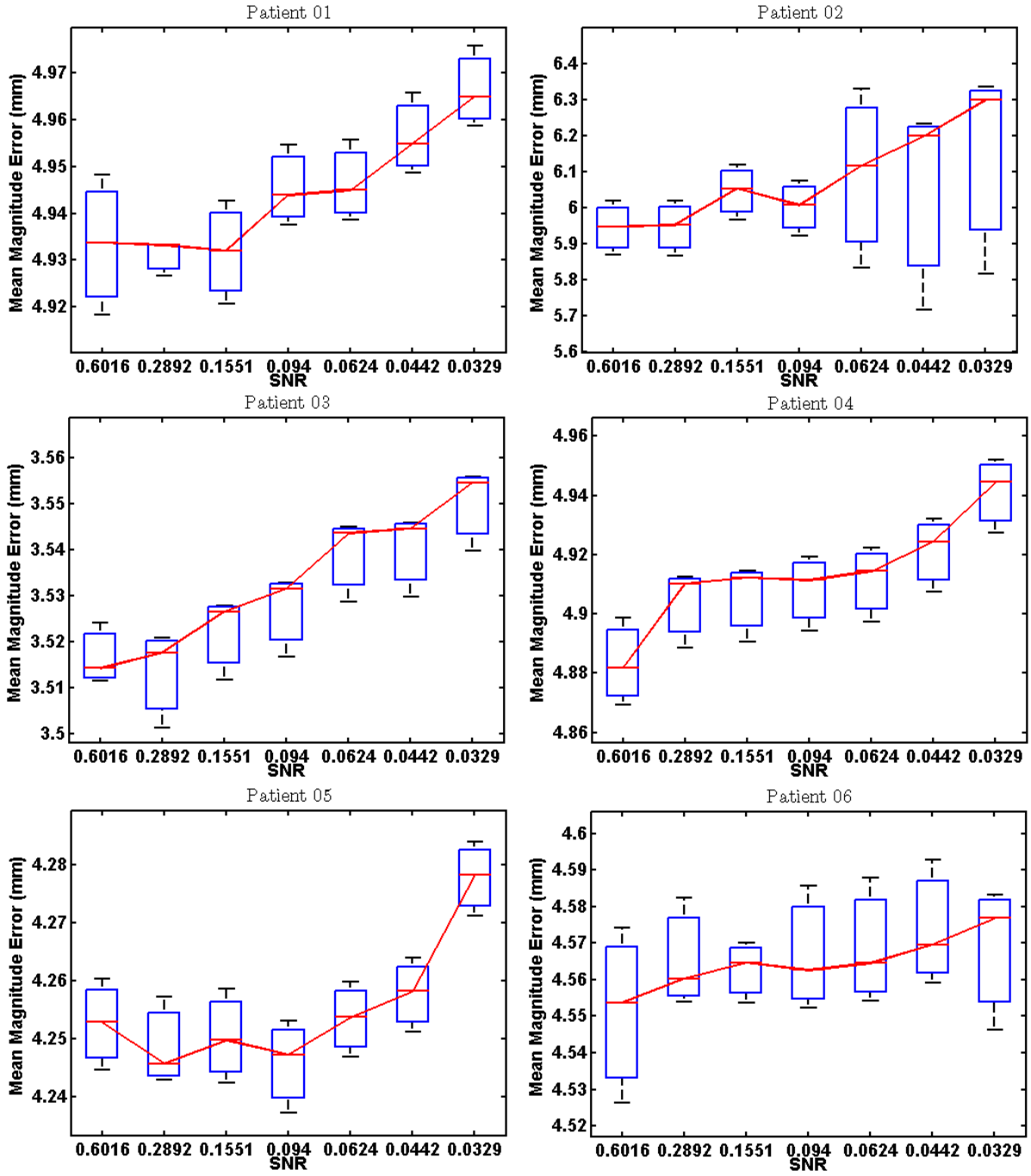

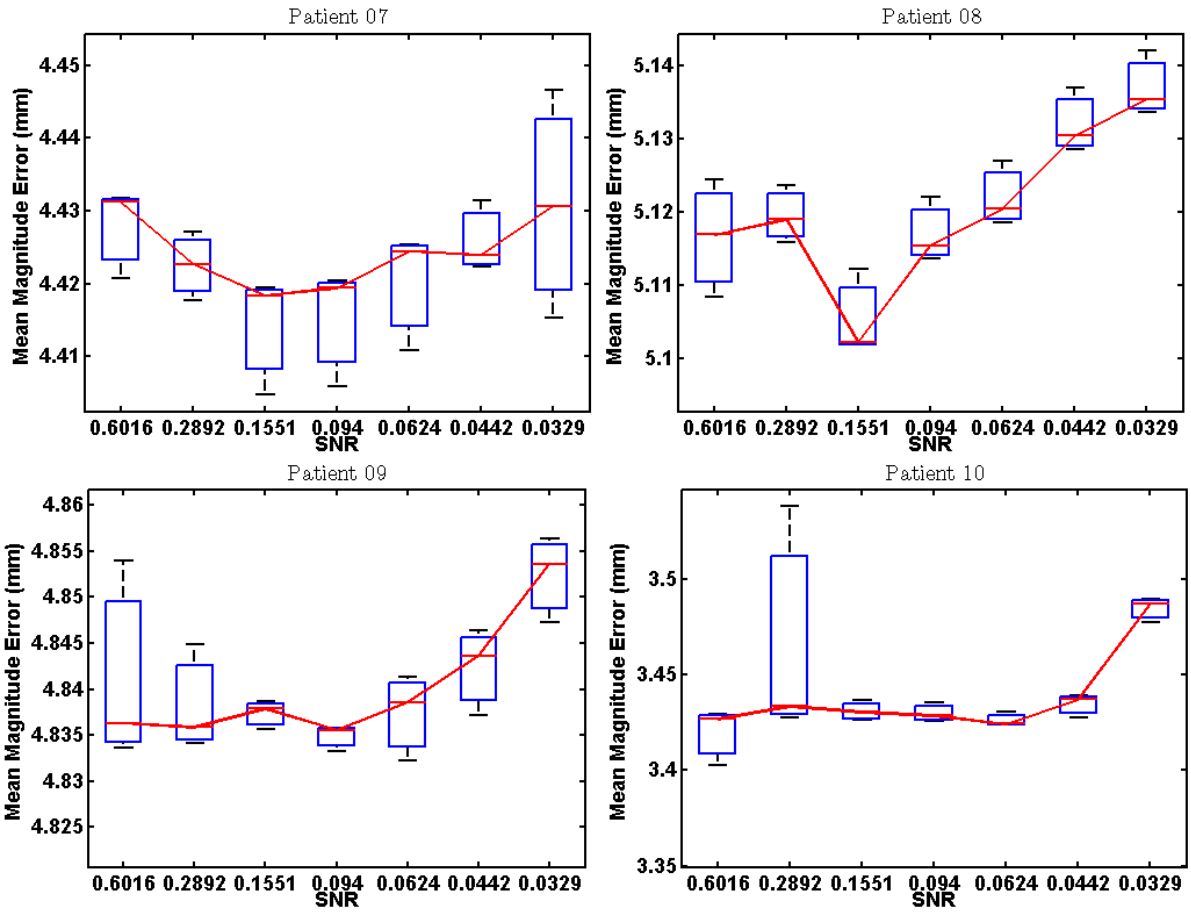

Figure 4.12: The boxplots represent the trend of registration error on the brain area at increasing noise level on the image, for each patient. On the x-axis there is the value of Signal-to-Noise Ratio. Each box shows the error values for the same noise level, for the three tests performed. The central mark is the median, the edges of the box are the 25th and 75th percentiles. The red line represents the fitting with spline function of the median values of the errors for each cicle.

Mean Magnitude Error and Normalized Mutual Information are computed only on the brain area of the image (BET) and reported in a boxplot which represents the trend of the evaluation parameters at different levels of noise on the image for each patient.
It is possible to note from the previous graphics a good performance of the registration algorithm, since the mean of total misalignment between the known vector

field and the estimated one is around $\sim$ 3-5 mm in all the patients and for all noise levels (the images voxels spacing is 0.5 x 0.5 x 1 mm).

Moreover MME increases at high levels of noise, showing that low values of Signal-to-Noise Ratio on the images, worsened the performance of the registration algorithm.

The same plots were made for the *Normalized Mutual Information*, and results are shown in Figure 4.13.

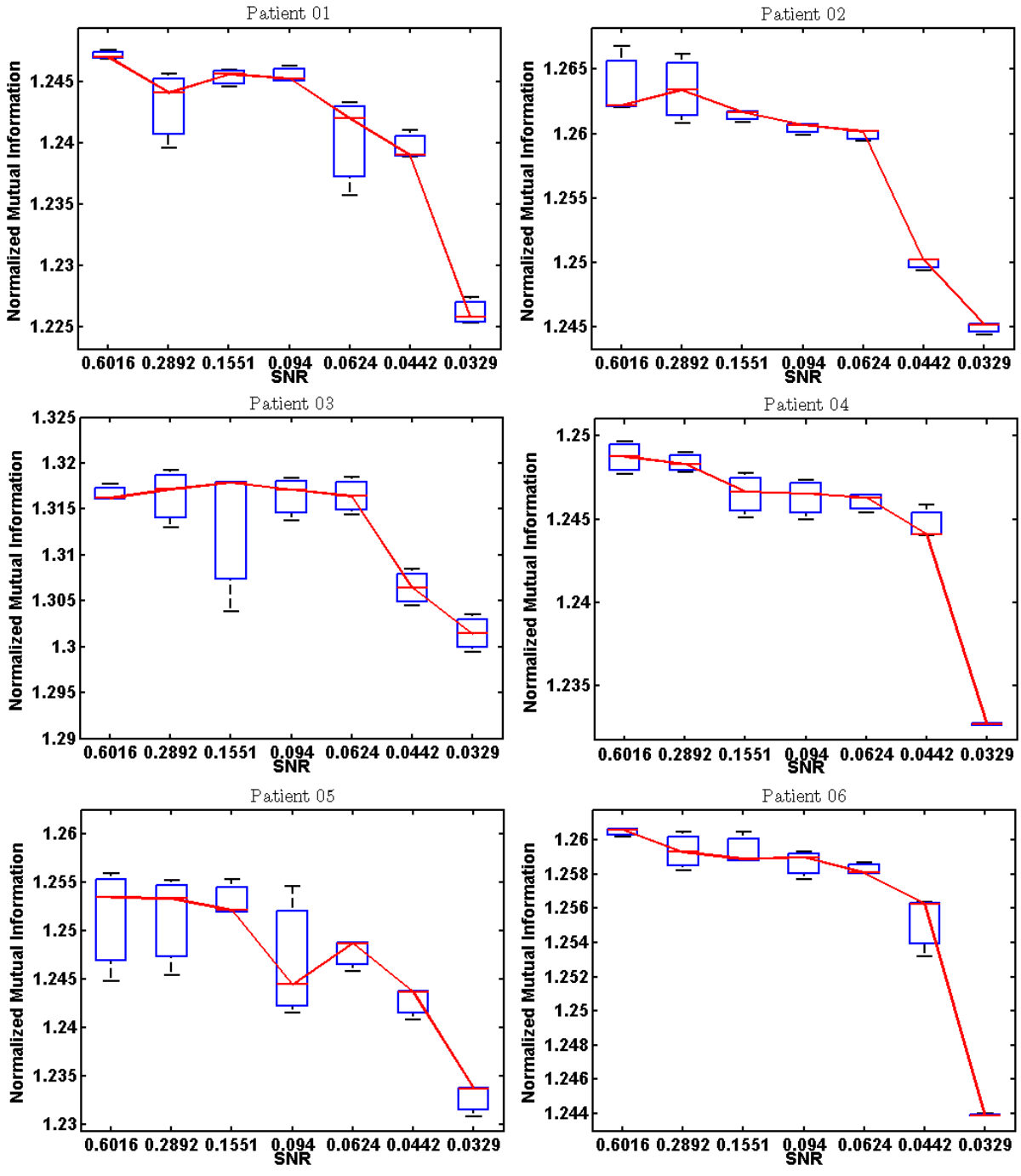
Patient 01
Normalized Mutual Information
1.245
1.24
1.235
1.23
1.225
0.6016 0.2892 0.1551 0.094 0.0624 0.0442 0.0329
SNR
Patient 02
Normalized Mutual Information
1.265
1.26
1.255
1.25
1.245
0.6016 0.2892 0.1551 0.094 0.0624 0.0442 0.0329
SNR
Patient 03
Normalized Mutual Information
1.325
1.32
1.315
1.31
1.305
1.3
1.295
1.29
0.6016 0.2892 0.1551 0.094 0.0624 0.0442 0.0329
SNR
Patient 04
Normalized Mutual Information
1.25
1.245
1.24
1.235
0.6016 0.2892 0.1551 0.094 0.0624 0.0442 0.0329
SNR
Patient 05
Normalized Mutual Information
1.26
1.255
1.25
1.245
1.24
1.235
1.23
0.6016 0.2892 0.1551 0.094 0.0624 0.0442 0.0329
SNR
Patient 06
Normalized Mutual Information
1.26
1.258
1.256
1.254
1.252
1.25
1.248
1.246
1.244
0.6016 0.2892 0.1551 0.094 0.0624 0.0442 0.0329
SNR

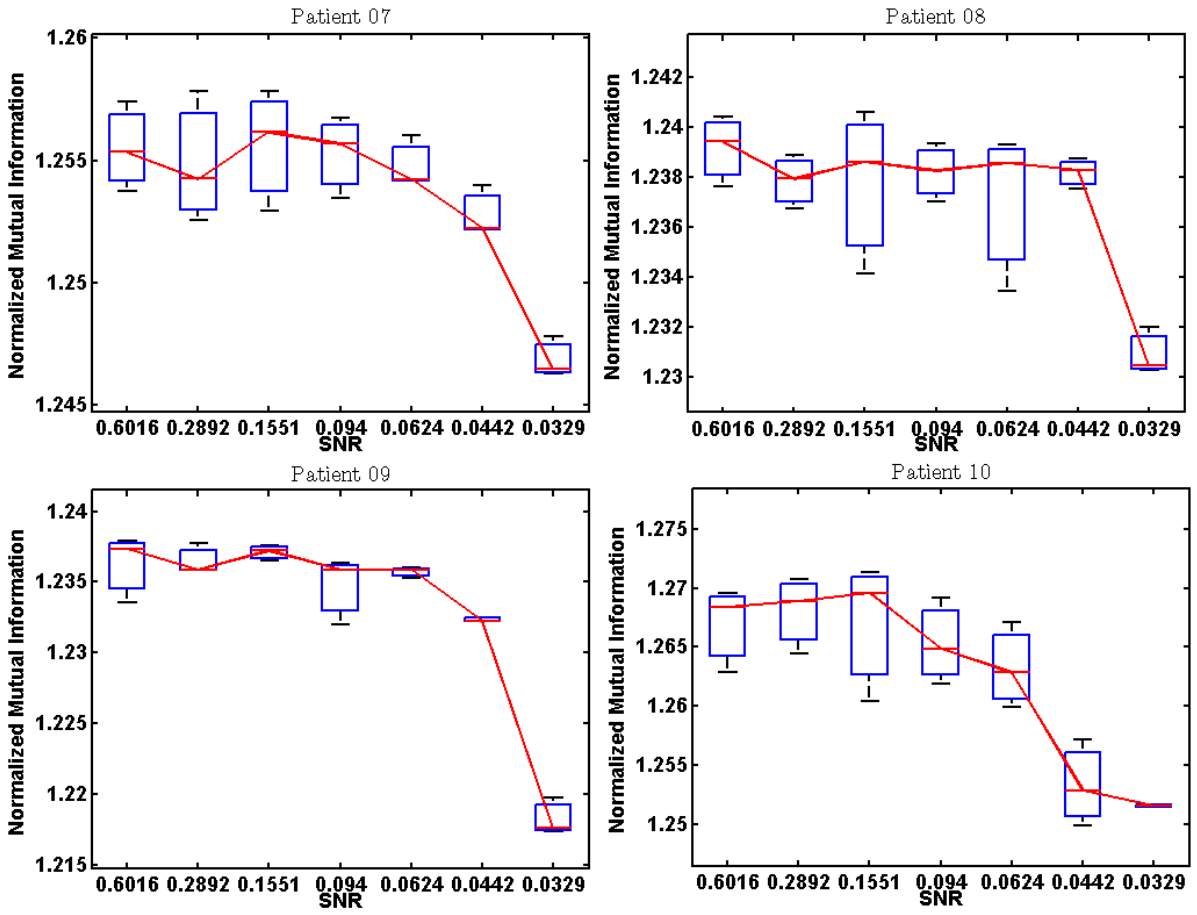

Figure 4.13: Normalized Mutual Information between the reference image and the registered one, computed on the brain area, at different levels of Signal-to-Noise Ratio.

It is evident that the mutual information decreases by increasing the intensity of Gaussian noise on the image. This is intuitive since the registration algorithm performance worsened with increasing deterioration of the image by the noise. So the reference image and the registered one "share" less information than a situation of optimal registration (less corrupted test image) in which the two images are almost the same.
The oscillations of the values have been ascribed to the stochastic nature of the noise.

In Figure 4.14 it is represented the trend of the mean registration error for all patients at increasing of noise intensity on the images.

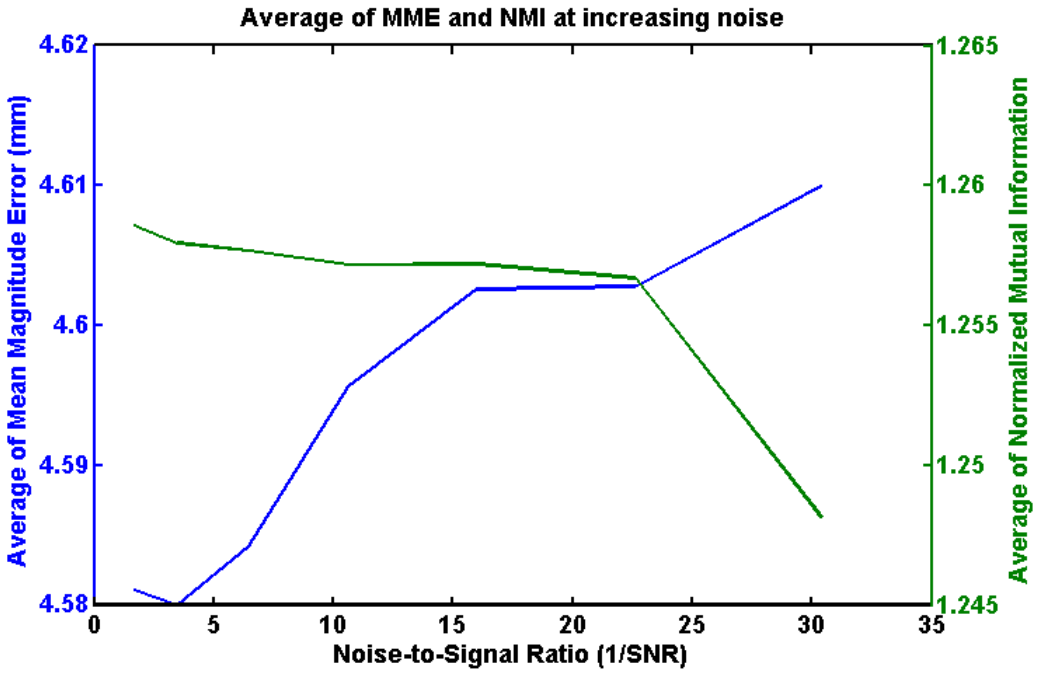

Figure 4.14: Average of the Mean Magnitude Error (at left) and Normalized Mutual Information (at right) at different values of Noise-to-Signal ratio, for all patients.

From the graphic it is possible to note that the registration error increases with the intensity of noise on the images, while the mutual information between the reference and the registered image decreases.
In particular NMI shows comparable values (although decreasing) until the last noise scaling, in which the mutual information drastically decays.

Finally it was computed the Jacobian of the known vector field, used to degradate the images, and that of the estimated by the registration.
It is possible to identify in Figure 4.15 the zone which contract and those which expand the image by observing the vector field.

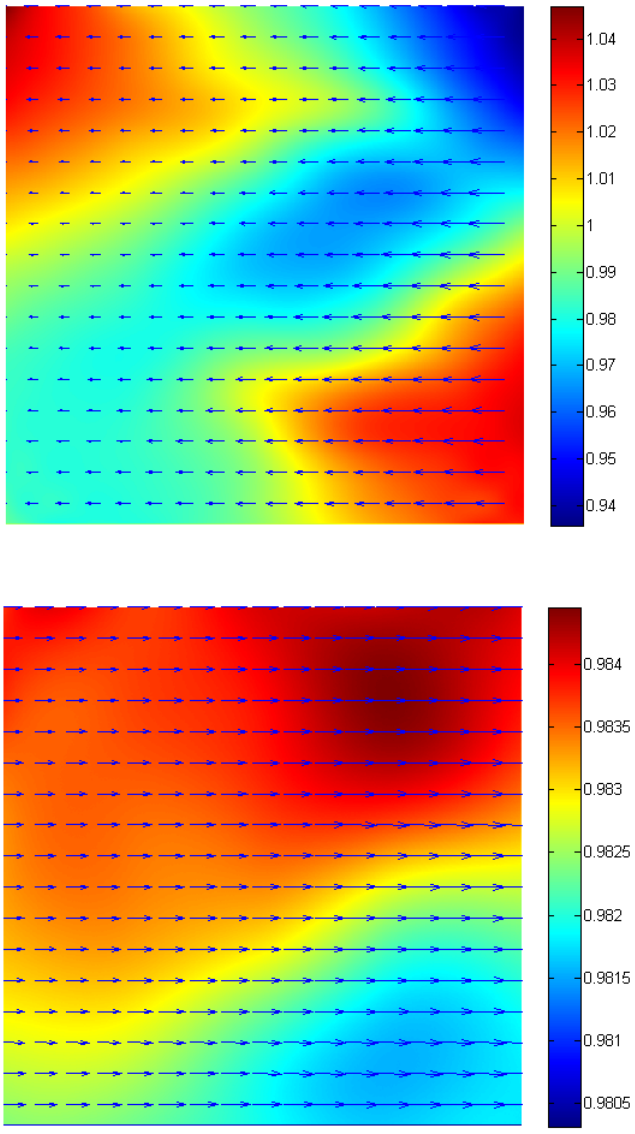

Figure 4.15: The first figure represents the jacobian of the known vector field of a slice for the component x, with the corresponding vector field. The second figure represents the same but for the vector field estimated by the registration. Values greater than 1 indicated a local expansion, while values less than 1 indicated a shrinkage at those points.

4.2.2 Input parameters optimization

In this section the results of the image registration test by varying the three input parameters are presented.

Number of bin values

The number of bin values tested are: 4, 8, 16, 32, 48, 64, 72, 84, 92, 100, 110, 116; considered most significant in term of results.
The trend of the registration error for different parameters in input to the registration algorithm is reported in Figure 4.16.

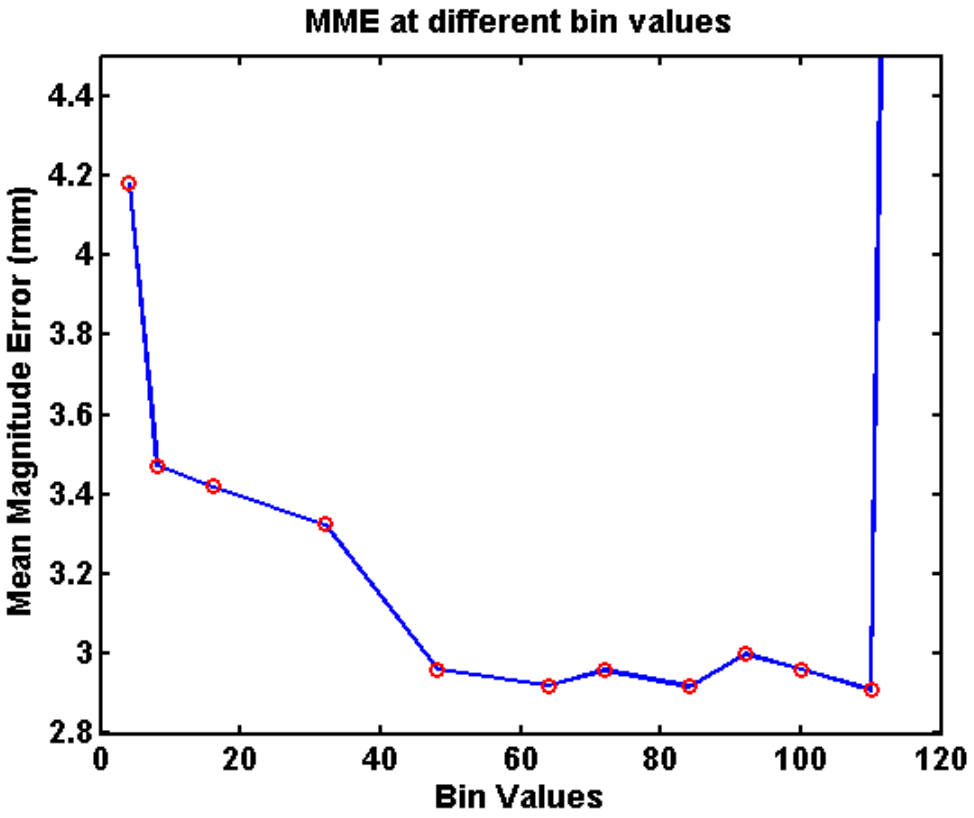

Figure 4.16: Mean Magnitude Error at increasing number of bin values for the same vector field applied on the image.

It can be noticed that on equal vector field, the registration error improves by increasing the number of bin values, reaches some local minima in a range between

$\sim$ 48 and 110, and then rises dramatically.

This is justifiable considering the histogram of the image using different values of bin values, as showed in Figure 4.17.

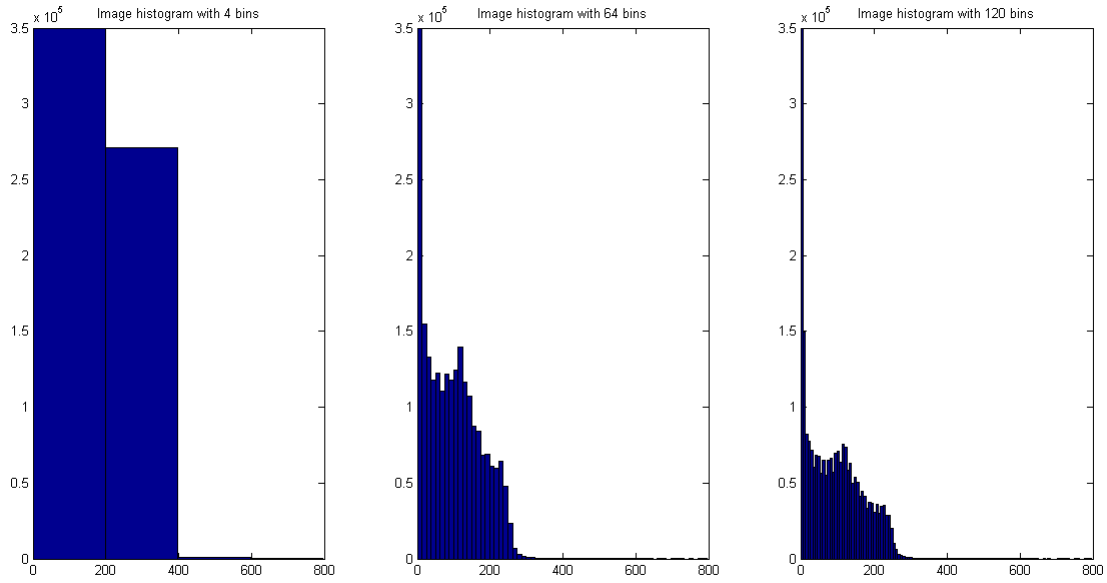

Figure 4.17: The figure represents the histogram of the same image using respectively 4, 64 and 120 bins.

It may be observed that the histogram of the image is underestimated with 4 bins; with 64 bins its shape is correctly represented, but with 120 bins the estimated histogram starts to alter its real shape, making it more smooth.
Thus the registration algorithm can not perform well for low bin values, neither for high values.
The selection of this parameter should therefore rely in a range between 48 and 116.

Grid values

To test the performance of registration algorithm, several 'grid' size are selected ranging from 10 to 150 mm, with a step of 10 mm.

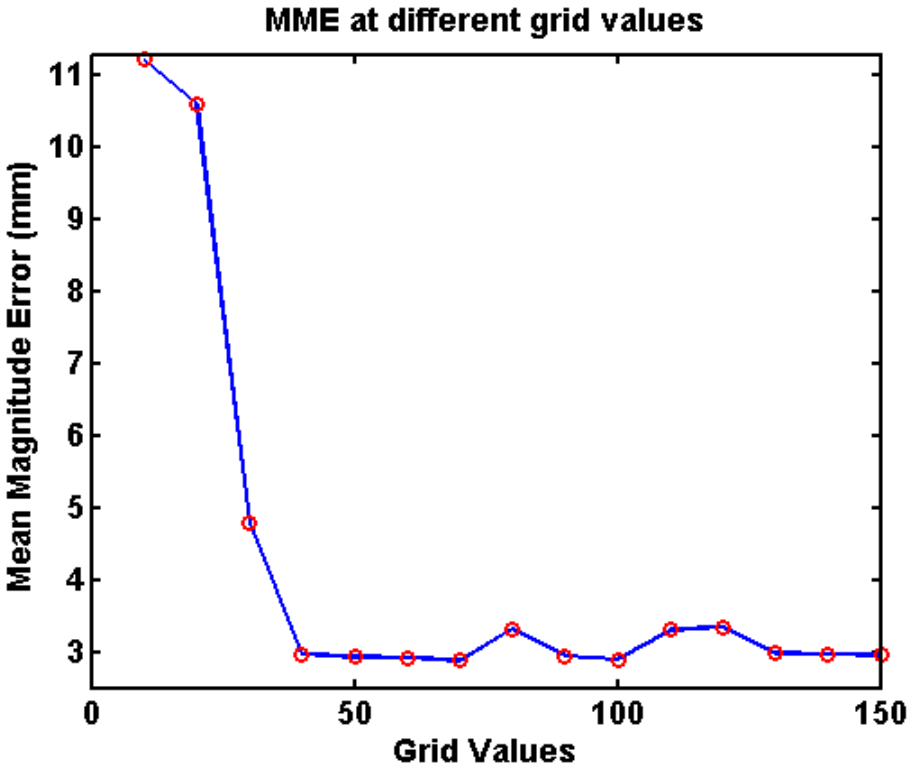

Figure 4.18: The figure represents the Mean Magnitude Error for different grid values.

Figure 4.18 shows that for low levels of grid (10 - 30 mm) the error is high, then decreases with increasing of grid values reaching an asintote.
Infact for low values of this parameter the image is divided in a very dense grid, with many nodes for the estimation of the vector field, but few points for the computation of the mutual information (because it is computed in each subset of the grid), Figure 4.19 points out this difference. So the mutual information is altered and may affect the registration process (since it is the metric used in the cost function of the algorithm).

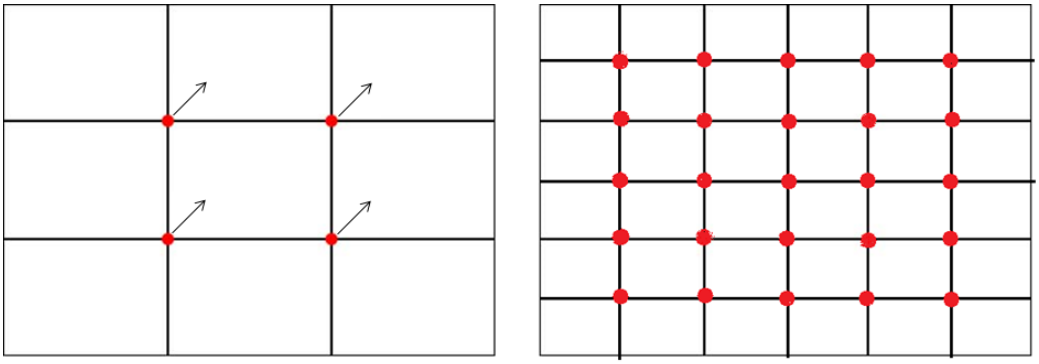

Figure 4.19: The left figure represents a large mesh grid with few points for the estimation of the vector field (arrows). At the left a more dense grid with smaller subset of voxels for the computation of mutual information.

Regularization Lambda

In addition several values of λ in input to the registration algorithm were tested, the values ranged between 0.01 and 0.3 with a step of 0.01.
The trend of the registration error (Mean Magnitude Error) for different parameter values is reported in Figure 4.20.

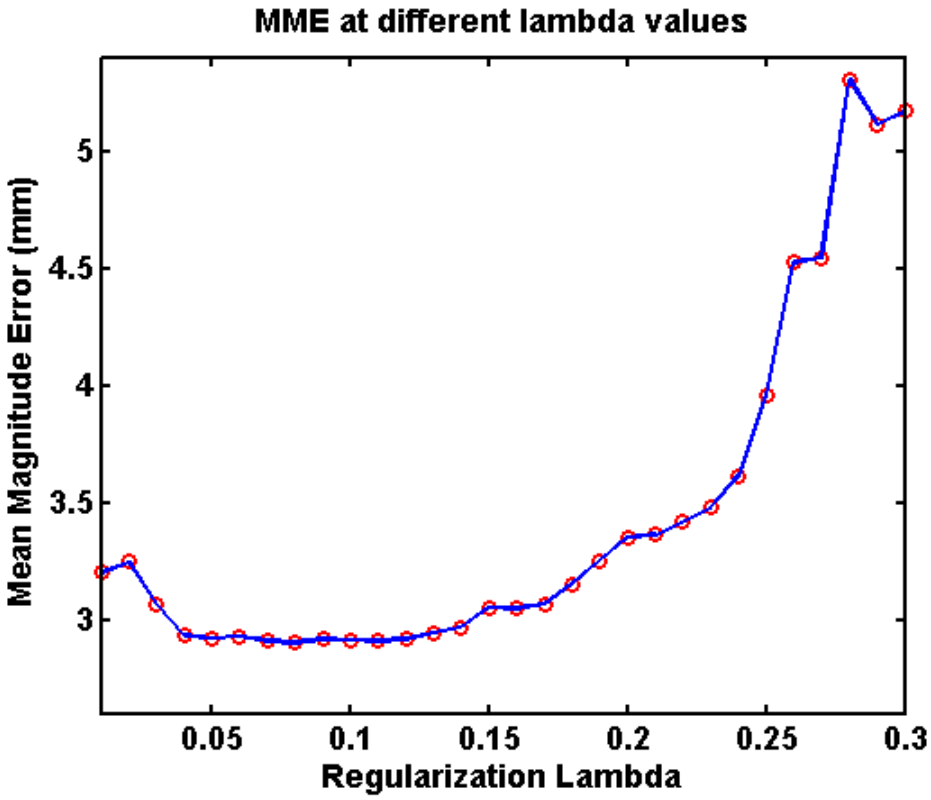

Figure 4.20: Mean Magnitude Error at increasing λ values.

It is possible to note that for the same vector field, low values of λ (from 0.01 to 0.03) provide higher errors than the subsequent values (from 0.04 to 0.015) in which the MME is minimal ($\sim 3mm$) and remains approximately constant for a wide range of values.
Then the registration error increases almost exponentially reaching maximum values of $\sim 5.5mm$ of misalignment between the reference and the test image.

This trend could be explained considering the role of the parameter in the cost function. Infact the parameter λ is a scalar term which penalizes vector fields that are not smooth, weighting on the regularization term.
As previously described, the regularization term of the cost function used in plastimatch registration algorithm, is the square of the vector field second derivative, according to:

$$C = MI(f, m) - \lambda c_{RM} \tag{4.1}$$

where f and m are respectively the fixed and the moving images and c_{RM} is the second derivative of the vector field.
Therefore too low values of λ "weigh" very little the term due to the second derivative of the vector field and in the cost function dominates the mutual information, allowing a deformation poorly controlled on the moving image.
In contrast, high values of this parameter prevent a strong warping, even if the information conveyed by the mutual information would require it.
The mechanism of the cost function could be compared to that of the accelerator and brake, in which the mutual information is the accelerator (requires strong warping) while λ is the brake (penalizes non-smooth vector fields).

To better understand this trend and try to give an empirical criterion for the choice of lambda, the same image used for the previous test was deformed manually with three increasing levels of skewness (Figure 4.21).
For each of these deformation the images were registered with the original one to estimate the vector field and then warped by the latter inverted.

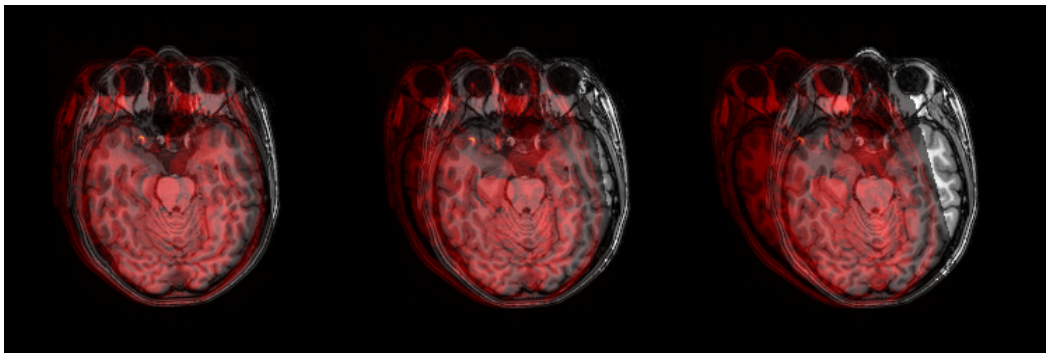

Figure 4.21: The reference image with overlayed the three deformed images with increasing levels of skewness: 5, 10, 15 degrees in xy plan.

Finally the original image was registered with the three test images generated by these deformations, at different values of regularization λ.
The results are reported in Figure 4.22.

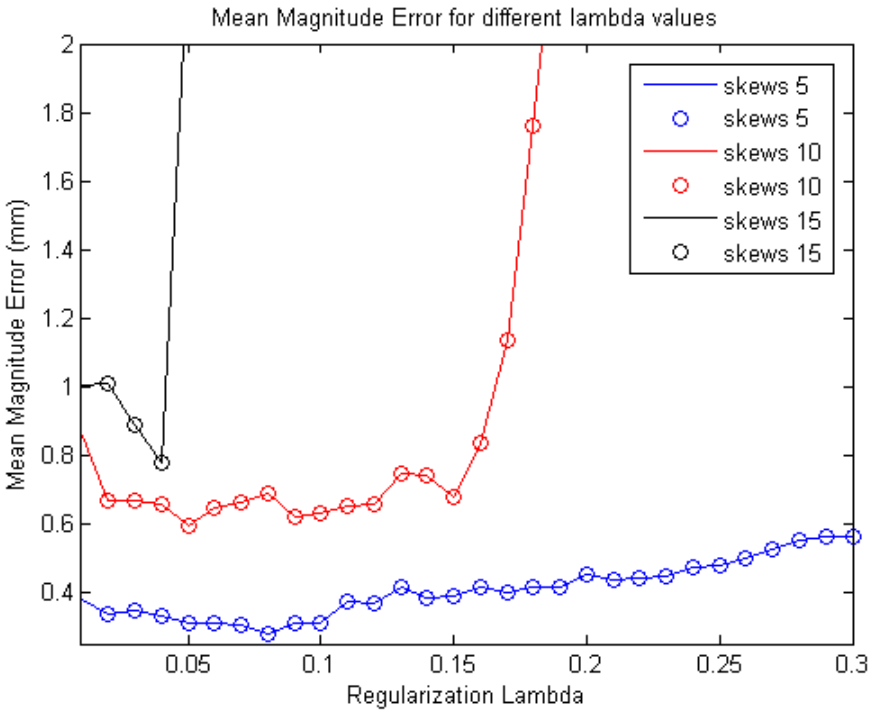

Figure 4.22: Mean Magnitude Error at increasing λ for three different levels of skewness on the image. The blue line corresponds to the image warped with 5 degrees of skews, the red line to the 10 degrees of deformation, while the blue one corresponds to 15 degrees of skews applied on the image.

It is possible to note that for low deformation of the image (5 degrees of skewness), also high values of λ (0.2-0.3) provide small registration errors, although the result gradually worsen.
With increasing levels of deformation (10 to 15 degrees of skews), the registration error rises faster for lambda values increasingly lower; the slope of the curve becomes steeper for higher deformation.
This because for large deformations it is necessary a strong warping to bring the moving image on the fixed image, but weigh too much the regularization term means a warping on the moving image less than necessary, thus leading to a bad registration. Moreover for low deformations also high regularization is appropriate because anyhow there are required low warping.

The registration errors for the three input parameters considered are interpolated in a 3D space.
It is possible to observe from Figure 4.23, the trend of the errors in a space defined by the bin, grid and lambda input values previously tested for each axis.

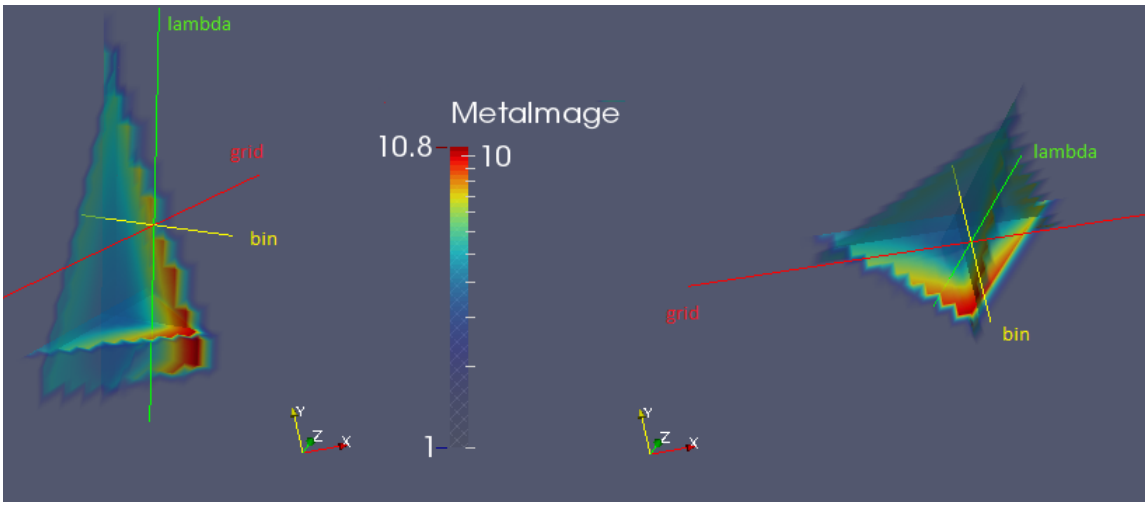

Figure 4.23: 3D function with MME values for the three parameters previously tested.

Chapter 5

Results of the clinical study

5.1 Mismatch quantification through perceived misalignment

For a further qualitative assessment it was asked to an expert pediatric neuroradiologist to evaluate the registrations between post-radiotherapy MRI and follow up MRI.
In order to quantify and validate the misalignment of the registration, there were compared registered and target images using a scale ranging from 0 to 5.
These 6 levels represent the perceived misalignment (PM) of the registered images respect to the fixed image (MRI of follow up); degree 0 expresses a radiological good registration, 3 represents a sufficient grade of matching, while 5 typifies the worst grade registration.
After that it was asked to an expert radiologist to draw up ten ROIs on the images for each plan: axial, coronal and sagittal as shown in Figure 5.1.

These ROIs where defined by tracing the contour of some focus point, like hippocampus or brainstem brain gyrus and sulci. Then this ROI was overlaid on the image which derive by the registration step, so that the same radiology could evaluate the different position of the focus point in each pair of images.
The results are reported in Table 5.1.

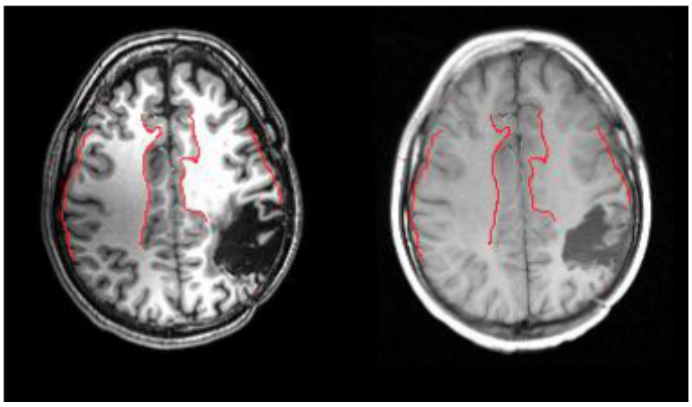

Figure 5.1: Qualitative validation using ROIs drawn by an expert radiologist.

Patient	RM0-RMn (Axial)	RM0-RMn (Coronal)	RM0-RMn (Sagittal)
Pt01	1	0	0,5
Pt02	1	2	2
Pt03	1	2	1
Pt04	0	2	1
Pt05	3	3	2
Pt06	2	2	2
Pt07	2	1	2
Pt08	1	1	2
Pt09	1	2	2
Pt10	1	2	2

Table 5.1: Registration perceived mismatch between MRI post radiation therapy and MRI of follow up, for each plan.

The good score for the exams evaluation through PM demonstrates the ability of the algorithm to manage the issues deriving by the late revaluation of these images.

5.2 Evaluation of radiation-induced damage by Fractional Anisotropy

5.2.1 Fractional Anisotropy comparison between cerebral hemispheres

DWI of the patients after the follow up period was examined to assess whether the Fractional Anisotropy (FA) between the brain area that has undergone the radiation dose and its controlateral area (the healthy hemisphere) is significantly different.
This comparison was made on patients which no longer present the tumor lesion. In Figure 5.2 an example of fractional anisotropy map is shown with overlapped the dose image. It is possible to note that this patient experienced has undergone the higher radiation dose on the left frontal lobe.

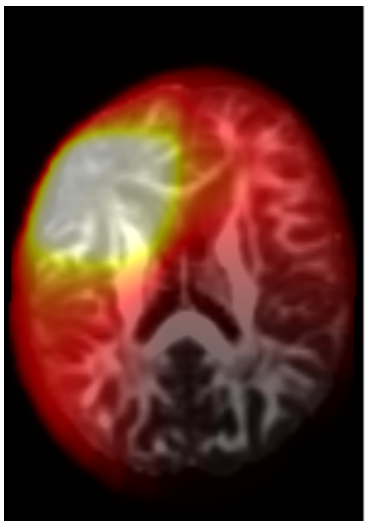

Figure 5.2: FA map with overlapped information of dose.

Thus in the particular case of this patient the comparison between fractional anisotropy values is made on the frontal lobe of the two hemispheres, as shown in Figure 5.3.

Figure 5.3: FA map with overlapped the ROIs considered for the comparison. At left the zone that undergone radiation dose, at right the healty area.

Non-parametric Wilcoxon rank-sum statistical test was performed to compare fractional anisotropy values between the same areas of the two hemispheres.
The results are reported in Table 5.2.

Patient	mean±std FA_lesion	mean±std FA_healthy	p-value
Pt01	0,163±0,089	0,215±0,091	0
Pt02	0,122±0,051	0,211±0,09	0
Pt03	0,110±0,06	0,182±0,089	0
Pt04	0,111±0,079	0,221±0,078	5,89E-39
Pt05	0,099±0,040	0,123±0,073	3,04E-33
Pt06	0,145±0,091	0,172±0,081	1,12E-04
Pt07	0,142±0,051	0,189±0,089	0

Table 5.2: Mean±standard deviation of FA values in the area that has undergone radiation dose and in the healthy zone. In the last column the p-values of the Wilcoxon test between the Fractional Anisotropy values of the two hemispheres are reported.

From the results it is possible to establish that the structures that have undergone radiation dose have significantly different fractional anisotropy values compared to the same structures that have received little or no dose.

5.2.2 Fractional Anisotropy at different dose levels

Finally the value of fractional anisotropy in the cerebral areas which received the radiation treatment was evaluated.
For the patient of Figure 5.2, for example, it was considered the left frontal lobe, obtaining the result of Figure 5.4.
In these structures were evaluated the mean FA values at different dose levels, and reported on a graph.

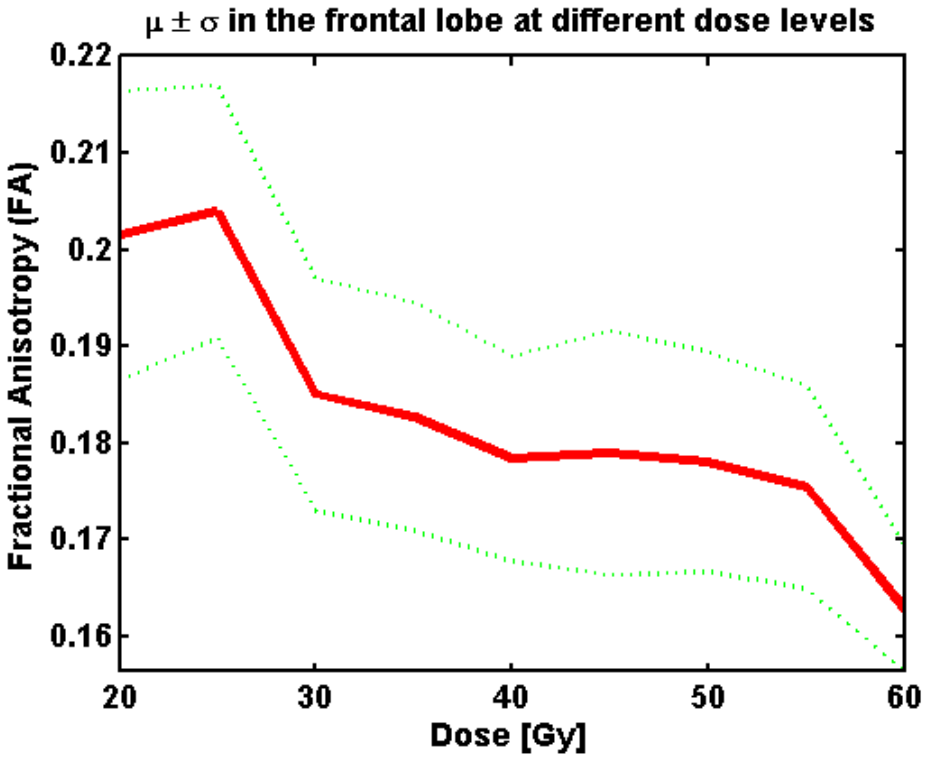

Figure 5.4: In red the mean Fractional Anisotropy of the left frontal lobe is represented at different dose levels. The green lines represent the standard deviation of the values.

In general it is possible to note that there is a trend in FA values at increasing of radiation dose; in fact the fractional anisotropy decreases.
Thus the ionising radiation alters the degree of anisotropy of the diffusion process of a nervous fiber; so years later by the treatment, nerve fibers which have undergone high dose, are damaged.

Chapter 6

Discussion

6.1 Conclusions

In this study the performance of an automatic image registration algorithm to correctly align images of the same pediatric patient (acquired at distance of years) has been validated.
The parameters used for this evaluation are the Mean Magnitude Error, that quantify the absolute misalignment in *mm* between the known and the estimated vector field, and the Normalized Mutual Information that evaluate how many the fixed and the registered image "are similar".

The obtained results have revealed a good capability of the algorithm to correctly align the corresponding structures of the two images with neglectable error.
In particular the *Plastimatch* image registration algorithm demonstrated to have the following properties:

- RELIABILITY: The registration error, computed as Mean Magnitude Error, assumes low values of misalignment between the two images to confront, thus revealing a good performance of this automatic process.
- STABILITY: Applying the algorithm in the same condition and using the same input parameters, it acts similarly. The several repetitions reported approximately the same result except for the different Gaussian noise applied on the test image.

- ROBUSTNESS: Noise don't undermine significatively the success of the algorithm and the quality of the registration, also for its high levels. Infact the values of the registration error doesn't increase significatively, rather it is comparable in the different situations.

Also qualitative assessment by the score of an expert neuroradiologist shows that the algorithm has an excellent capability of alignment two images of different resolutions, field of view but above all size of the cerebral structures.

The image registration algorithm was tested also varying three input parameters: the number of bins of the histogram, the dimensions of the imaginary grid to estimate vector field and mutual information, and finally the λ of regularization of the cost function used in the registration process.
This test showed that for the same vector field applied on the image, the input parameters considered reveal an optimal range of values for which the registration error is minimal.

Considering the number of bin, it emerged that low values (between $\sim$ 4 and 48) and too high values (up to $\sim$ 118) are not suitable to correctly model the histogram of an image, thus having a bad estimation of the mutual information between the images (that is based on the joint histogram) and worsening the performance of image registration. In particular, if the image has an irregular histogram it is preferable to select high bin values of the optimal range identified, while for smoothed histogram also lower values are suitable for good performances of the algorithm.

It was also pointed out that the grid dimensions to give in input to the registration algorithm should be at least 30 (mm), for image resolution that does not exceed the millimeter, to have a larger subset of values to estimate the mutual information between the images and correctly register them.
Although it is not preferable to choose too high values, not to have few points (node) for the estimation of the vector field.

For the regularization λ the criterion of selection is similar to that of the bin values. Infact too low values ($\sim$ 0.01 to 0.03) are not preferable, to avoid a weak

regularization of the vector field, which could generate a strong warping of the moving image, thus deforming too much the latter and not align it correctly to the reference image.
Vice versa high values of λ could weight too much the regularization term and prevent the information conveyed by the mutual information, producing a bad registration result.
It is showed that desirable λ values for this registration algorithm lie in a range between ~ 0.04 and 0.15.
But this range of optimal values could undergoes slight change for different vector fields. In particular for very different images to register, that require a strong warping of the moving image, the range of values of λ in input to algorithm, which provide a good registration result, is reduced, as shown in Figure 4.22.
The optimal ranges of values for the input parameters previously described, could eventually lightly change according to different vector fields applied on the image.

From the comparison of Fractional Anisotropy between the structures that have undergone high radiation dose to the same structures that have received little or no dose, it emerged a statistically significant difference.
Radiation therapy has altered the bundles of nerve fibers of the white matter, not allowing the child to properly develop these tissues with the growth.
Therefore, it is important to improve radiosurgical planning in childhood brain tumors trying to adapt them as much as possible to the individual necessity of each patient, thus improving their future quality of life.
For this purpose it may be useful the functional MRI (fMRI) before each radiosurgical planning. Through this functional neuroimaging technique it is possible to better evaluate what brain structures should strictly avoid radiation treatment.

6.2 Future developments

The work developed in this study revealed some encouraging preliminary results, thus paving the way to possible developments of the study.
The validation of the algorithm in fact was made (on all the patients) using a real vector field only, but it is possible to confront the registration error also varying the vector field; to verify if its trend remain approximately constant for different warping.

The validation was made indeed considering two monomodal images (both MRI), but it is possible to confront also two multimodal images, for example MRI and Computed Tomography (CT), for the same patient.

In addition the input parameters were tested modifying one of them and keeping to a fixed value the others.
The optimal condition to find the best input for the algorithm would be to test all the different combinations of parameters, although computationally expensive.

Finally it would be interesting to establish, if exist, an analytical criterion for the selection of the regularization λ to provide input to the algorithm.
So that the physician could have a more reliable objective criterion.
In fact in this study it was given only an empirical preliminary selection criterion.

Appendix A

T1-weighted MRI sequences

T1-weighted scans depict differences in the spin-lattice (or T1) relaxation time of various tissues within the body, unlike the T2-weighted scans that depict differences in the spin to spin relaxation time of various tissues within the body [69]. Different sequences could generate this contrast on images.
Below there are described the sequences of T1-weighted MRI data used in this study.

Turbo spin echo **(TSE)**
The spin-echo pulse sequence can produce proton density weighting, T1 weighting, and T2 weighting with a first 90° pulse and after a Time of Echo (TE) a second 180° pulse. TE and Time of Repetition (TR) are set to achieve these weightings. Turbo spin echo is a spin echo with multiple 180° pulses used to create multiple echoes [70]. However, instead of each echo forming a different image data set, all the echoes are used to create a single image data set at a faster rate.
A new acquisition parameter will be introduced called the *echo train length*, which is the number of echoes that are formed.
Figure A.1 shows a typical turbo spin echo sequence with an example of T1 TSE brain acquisition.

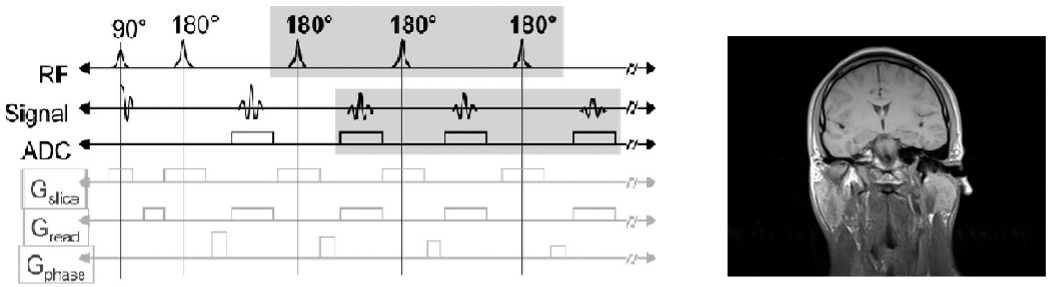

Figure A.1: A Turbo Spin Echo pulse sequence, in which multiple 180° RF pulses are applied after each excitation pulse. The right figure is a T1 turbo spin echo acquisition.

It is possible to choose the echoes closest to our TE of interest to form the contrast weighting that is desired.

Unlike the traditional spin-echo sequence, in which it acquires a single line of k-space (and therefore the image), then it is necessary to wait that the magnetization returns to the equilibrium state (normally a few seconds), in a fast sequence spin echo is acquired a series of echoes produced by various impulses at 180° that refocus the magnetization after the 90° pulse excitation.

Multi Planar Reconstruction **(MPR)**
Multi-planar reconstruction (MPR) software allows to acquire images at arbitrary planes, defined by the operator, using the pixel data from a stack of planar images (base images) [71].
The user can select plane orientation and thickness (typically equal or greater than the base scan thickness), and can prescribe the number, location, and separation of reconstructed slices.

Once suitable base scans have been performed; then, with a tool to scan "virtually" the patient, the base scan data can be used to create images precisely aligned with anatomical planes, create sets of slices with multiple orientations and slice thickness's (at the same contrast weighting as the base scans) and compensate for positioning errors.
The quality and utility of MPR images is directly related to the quality of the base images used to create them.

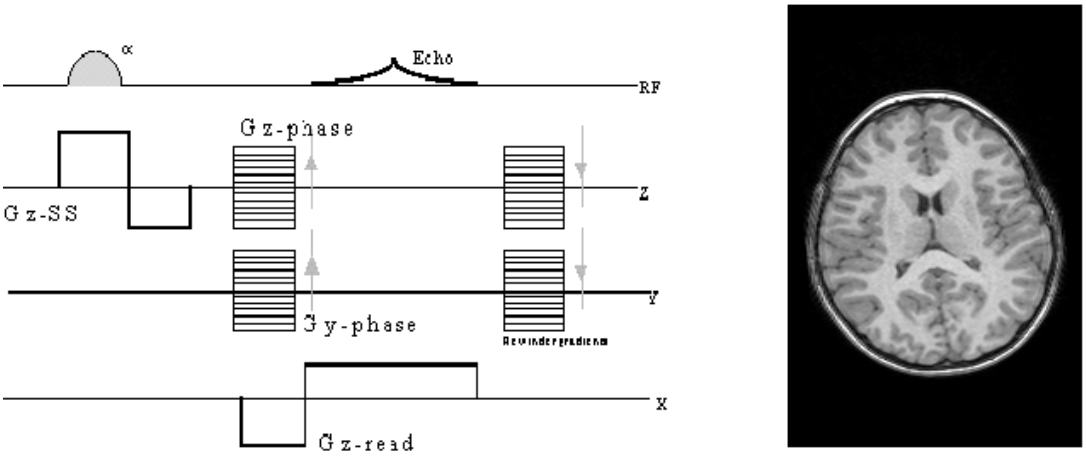

Figure A.2: The left figure represents a pulse-timing diagram for a slice selective MPR 3DFT sequence, while on the right there is an example of a Multi Planar Reconstruction of a T1 weighted brain MRI.

In Figure A.2 it is possibile to see an example of gradient, in the z, y, x direction, performed in this type of MRI acquisition.
The first G_z gradient is employed for the slice selection and then, together with the G_y gradient, it is used for the phase encoding in the two directions, for the positioning on the k - *space*. The G_x gradient is finally employed to perform the

sampling of data to fill in the space.
A typical application is the isotropic T1 brain imaging application, when thin slice T1 images are required with more time efficient or effective solutions.

Volumetric Interpolated Breath-hold Examination **(VIBE)**
VIBE is a novel 3D Ultra fast Gradient Echo sequence that uses a radial stack-of-stars sampling scheme to acquire the k-space information [72].
This sequence produces T1 weighted 3D images using interpolation and/or partial Fourier techniques. VIBE sequence is a modified form of FLASH sequence (that is an ultrafast gradient echo pulse sequence with data acquisition after an initial 180° preparation pulse for contrast enhancement), which permits dynamic and high-resolution imaging under 30 seconds breath-hold, as shown in Figure A.3. As

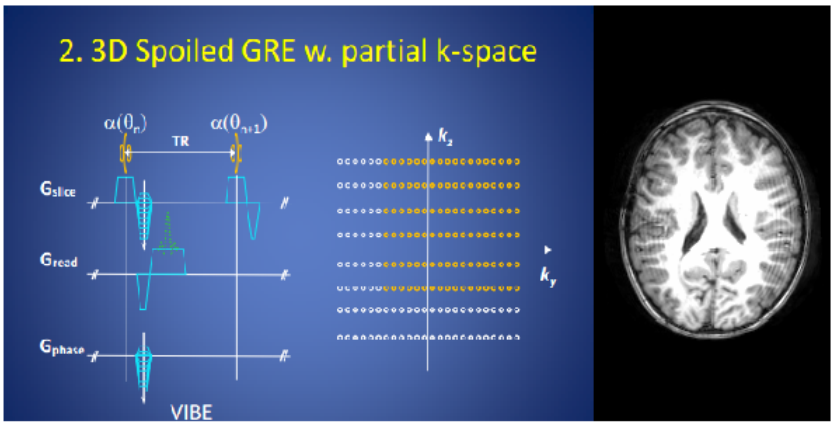

Figure A.3: A sequence of Volume Interpolated ultra fast GRE with the relative acquisition.

compared to a FLASH sequence, the VIBE sequence provides similar image quality (the same SNR and contrast) with increased slice selective spatial resolution. This sequences are particularly useful for the evaluation of soft tissue and vasculature simultaneously.

Appendix B

NIfTI format

The NIfTI file format was born to enhance the utility and communicability of informatics tools related to neuroimaging [73].
In medical imaging infact, there is a lack of adequate information about orientation in space, such that the stored data could not be unambiguously interpreted; also the file is used by many different imaging software that introduce their coordinate system.
Although there is a convention adopted by most manufacturers of radiological equipment to show the left side of the patient on the right side of the observer, as if the patient were being observed from face-to-face or, if lying supine, from the feet, neurologists actually convened to create a "neurological" convention that would be just the opposite of the radiological.
The NIfTI format obviated all these issues, rendering these terms obsolete. Software can now mark the left or the right side correctly, sometimes giving the option of showing it flipped to better adapt to the user personal orientation preference [73].

Appendix C

'Plastimatch warp' command.

The exact Plastimatch command used to warp an image with a vector field is the following:

```
plastimatch warp - -input RMn.nii - -output-img deform_RM.nii - -xf
inverse_vf.nii -F RMn.nii
```

where 'RMn.nii' was the reference image of the patient (follow up MRI), while 'deform_RM.nii' was the filename given to the warped image and 'inverse_vf.nii' was the known vector field obtained through the previous passages.
The final sequence '`- F RMn.nii`' indicates that it is matched the output image size to the image size specified in this line, to avoid that the deformation performed could change arbitrarily the dimension of the image, thus creating problem in the following computation.
Note that the Plastimatch command can be launched either from the command prompt of the computer that from Matlab®; in the latter case the call to the external environment is made with the exclamation symbol before the command, like this:

```
!plastimatch warp - -input RMn.nii - -output-img deform_RM.nii - -xf
inverse_vf.nii -F RMn.nii
```

Appendix D

Brain Extraction Tool

An automated robust and accurate method is proposed [74] for segmenting magnetic resonance head images into brain and non-brain, tested on datasets of a large variety of scanners and for a wide variety of MR sequence.
The method, Brain Extraction Tool (BET), uses a deformable model that evolves to fit the brain's surface by the application of a set of locally adaptive model forces. The method proposed does not attempt to model the brain surface at the finest level.

The intensity histogram is processed to find lower and upper intensity values for the image, and a threshold to differentiate brain/non-brain.
Then it is found the center-of-gravity of the head image along with the rough size of the head in the image. A triangular sphere's surface is initialized inside the brain and allowed to slowly deform following "smooth" forces, while attempting to move toward the brain's edge.
The process is re-run with a higher smoothness constraint until a suitable solution is arrived.
Figure D.1 illustrates the procedure described.

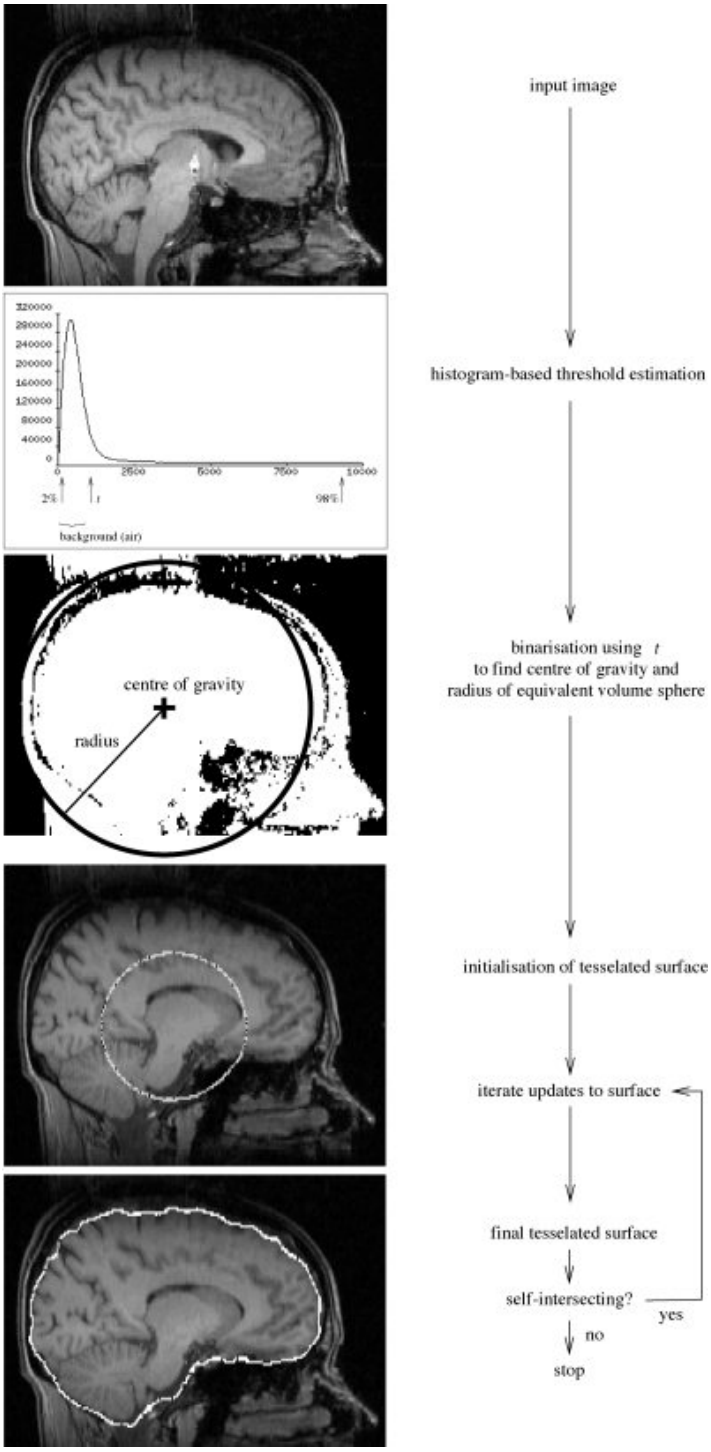

Figure D.1: BET processing flowchart.

Appendix E

Matlab code

```
1
2 % Resample
3 system(['resliceto' refn 'RMn.nii reference.nii']);
4
5
6 % Warp
7 system(['plastimatch warp --input reference.nii --output-
      img'
8  orginal_test '--xf' trasf' -F 'ref0']);
9
10 % Histogram rescaling
11 ans.img=(ans.img/max(ans.img(:)))*2000;
12
13 % Addition of noise
14 original_test.img=original_test.img+((med*gaus_scaling(a))+
15 (std*randn(size(original_test.img))));
16
17
18 % Registration
19 plastireg2b('align',ref,test,[],p.o0,p.i0,[1],20,'40
20              40 40',0,[],[],0.0005);
21 plastireg2b('translation',ref,test,[],p.o1,p.i1,
```

```
22                [10:-1:1],512,'40 40 40',0,[],[],0.0005);
23
24 plastireg2b('affine',ref,test,p.o1,p.o2,p.i2,
25                [6:-1:1],64,'40 40 40',0,[],[],0.0005);
26
27 plastireg2b('lbfgsbmipl',ref,test,p.o2,p.o3,p.i3,[3 1],
28                64,'60 60 60',0,1,1,0.05);
29
30 % Mean Magnitude Error
31 arr=arrayfun(@(gx,gy, gz, tx, ty, tz) norm([gx,gy,gz]+[tx,
       ty,tz]),
32 nx(:),ny(:),nz(:), sx(:),sy(:),sz(:));
33 MME=mean(arr);
```

Bibliography

[1] C. Sklar, "Childhood brain tumors," *Journal of Pediatric Endocrinology and Metabolism*, vol. 15, pp. 669 – 674, 2011.

[2] C. H. Chapman, V. Nagesh, P. C. Sundgren, H. Buchtel, T. L. Chenevert, L. Junck, T. S. Lawrence, C. I. Tsien, and Y. Cao, "Diffusion tensor imaging of normal-appearing white matter as biomarker for radiation-induced late delayed cognitive decline," *Int. J. Radiat. Oncol. Biol. Phys.*, vol. 82, pp. 2033–2040, Apr 2012.

[3] L. H. Leung, G. C. Ooi, D. L. Kwong, G. C. Chan, G. Cao, and P. L. Khong, "White-matter diffusion anisotropy after chemo-irradiation: a statistical parametric mapping study and histogram analysis," *Neuroimage*, vol. 21, pp. 261–268, Jan 2004.

[4] C. G. Filippi, D. D. Lin, A. J. Tsiouris, R. Watts, A. M. Packard, L. A. Heier, and A. M. Ulu?, "Diffusion-tensor MR imaging in children with developmental delay: preliminary findings," *Radiology*, vol. 229, pp. 44–50, Oct 2003.

[5] "http://plastimatch.org,"

[6] F. Ian and M. Pollak, "Brain tumors in children," *The New England Journal of Medicine*, vol. 331, pp. 1500 – 1507, 1994.

[7] E. Larson, "The epidemiology of primary brain tumors," *J Neurosurg Nurs*, vol. 12, pp. 121–127, Sep 1980.

[8] A. T. Schmidt, R. B. Martin, A. Ozturk, W. R. Kates, M. D. Wharam, E. M. Mahone, and A. Horska, "Neuroimaging and neuropsychological follow-

up study in a pediatric brain tumor patient treated with surgery and radiation," *Neurocase*, vol. 16, pp. 74–90, Feb 2010.

[9] P. Kaatsch, "Epidemiology of childhood cancer," *Cancer Treat. Rev.*, vol. 36, pp. 277–285, Jun 2010.

[10] E. M. Ward, M. J. Thun, L. M. Hannan, and A. Jemal, "Interpreting cancer trends," *Ann. N. Y. Acad. Sci.*, vol. 1076, pp. 29–53, Sep 2006.

[11] L. Padovani, N. Andre, L. S. Constine, and X. Muracciole, "Neurocognitive function after radiotherapy for paediatric brain tumours," *Nat Rev Neurol*, vol. 8, pp. 578–588, Oct 2012.

[12] K. Muller, A. Gnekow, F. Falkenstein, J. Scheiderbauer, I. Zwiener, T. Pietsch, M. Warmuth-Metz, J. Voges, G. Nikkhah, M. Flentje, S. E. Combs, D. Vordermark, M. Kocher, and R. D. Kortmann, "Radiotherapy in pediatric pilocytic astrocytomas. A subgroup analysis within the prospective multicenter study HIT-LGG 1996 by the German Society of Pediatric Oncology and Hematology (GPOH)," *Strahlenther Onkol*, vol. 189, pp. 647–655, Aug 2013.

[13] D. van de Beek, J. M. Drake, and A. R. Tunkel, "Nosocomial bacterial meningitis," *N. Engl. J. Med.*, vol. 362, pp. 146–154, Jan 2010.

[14] E. Dropcho, J. Wisoff, and R. Walker, "Supratentorial malignant gliomas in childhood: a review of fifty cases," *Ann Neurol*, vol. 22, pp. 355 – 364, 1987.

[15] G. Matlashewski, P. Lamb, D. Pim, J. Peacock, L. Crawford, and S. Benchimol, "Isolation and characterization of a human p53 cDNA clone: expression of the human p53 gene," *EMBO J.*, vol. 3, pp. 3257–3262, Dec 1984.

[16] H. Yan, D. W. Parsons, G. Jin, R. McLendon, B. A. Rasheed, W. Yuan, I. Kos, I. Batinic-Haberle, S. Jones, G. J. Riggins, H. Friedman, A. Friedman, D. Reardon, J. Herndon, K. W. Kinzler, V. E. Velculescu, B. Vogelstein, and D. D. Bigner, "IDH1 and IDH2 mutations in gliomas," *N. Engl. J. Med.*, vol. 360, pp. 765–773, Feb 2009.

[17] "http://www.hopkinsmedicine.org/neurology_neurosurgery/specialty_areas/brain_tumor/center/glioma/treatment.html,"

[18] S. E. Metcalfe, "Biopsy versus resection for malignant glioma," *Cochrane Database Syst Rev*, no. 2, p. CD002034, 2000.

[19] N. authors listed, "Chemotherapy for high-grade glioma," *Cochrane Database Syst Rev*, no. 4, p. CD003913, 2002.

[20] A. S. Jakola, K. S. Myrmel, R. Kloster, S. H. Torp, S. Lindal, G. Unsgard, and O. Solheim, "Comparison of a strategy favoring early surgical resection vs a strategy favoring watchful waiting in low-grade gliomas," *JAMA*, vol. 308, pp. 1881–1888, Nov 2012.

[21] M. G. Hart, R. Grant, R. Garside, G. Rogers, M. Somerville, and K. Stein, "Temozolomide for high grade glioma," *Cochrane Database Syst Rev*, no. 4, p. CD007415, 2008.

[22] B. Kennedy, "Astrocytoma," *Medscape*, 2013.

[23] J. C. Buckner, P. D. Brown, B. P. O'Neill, F. B. Meyer, C. J. Wetmore, and J. H. Uhm, "Central nervous system tumors," *Mayo Clin. Proc.*, vol. 82, pp. 1271–1286, Oct 2007.

[24] J. Pierre, M. Cure, M. Mohr, N. Heldt, F. Kwiatkowski, and . R. P. Jean-Jacques Lemaire, M.D., "Low grade supratentorial astrocytomas," *Wiley online library*, vol. 73, pp. 1937 – 1945, 2006.

[25] A. Raimondi and T. Tomita, "Medulloblastoma in childhood," *Pediatric Neurosurgery*, vol. 5, pp. 310 – 328, 1979.

[26] J. G. Gurney, M. A. Smith, and G. R. Bunin, "Cns and miscellaneous intracranial and intraspinal neoplasms," *Cancer Incidence and Survival among Children and Adolescents: United States SEER Program 1975 1995*, vol. 99, 1999.

[27] D. Grammel, M. Warmuth Metz, A. von Bueren, M. Kool, T. Pietsch, and K. HA., "Sonic hedgehog associated medulloblastoma arising from the cochlear nuclei of the brainstem.," *Acta Neuropathol*, 2012.

[28] V. Kieffer Renaux, C. Bulteau, and J. Grill, "Patterns of neuropsychological deficits in children with medulloblastoma according to craniospatial irradiation doses," *Dev Med Child Neurol*, vol. 42, pp. 741 – 750, 2000.

[29] T. MacDonald, K. Brown, and B. LaFleur, "Expression profiling of medulloblastoma: Pdgfra and the ras/mapk pathway as therapeutic targets for metastatic disease," *Nat Genet*, vol. 29, pp. 143 – 152, 2001.

[30] M. Blomstrand, N. P. Brodin, P. Munck Af Rosenschold, I. R. Vogelius, G. Sanchez Merino, A. Kiil-Berthlesen, K. Blomgren, B. Lannering, S. M. Bentzen, and T. Bjork-Eriksson, "Estimated clinical benefit of protecting neurogenesis in the developing brain during radiation therapy for pediatric medulloblastoma," *Neuro-oncology*, vol. 14, pp. 882–889, Jul 2012.

[31] M. Massimino, G. Cefalo, D. Riva, V. Biassoni, F. Spreafico, and E. Pecori, "Long term results of combined preradiation chemotherapy and age tailored radiotherapy doses for childhood medulloblastoma," *The Journal of Neuroncology*, 2012.

[32] H. Poppleton and R. Gilbertson, "Stem cells of ependymoma," *Br J Cancer*, vol. 36, pp. 9–10, 2007.

[33] L. Zhang, H. Chen, L. Wang, T. Liu, J. Yeh, G. Lu, L. Yang, and H. Mao, "Delivery of therapeutic radioisotopes using nanoparticle platforms: potential benefit in systemic radiation therapy," *Nanotechnol Sci Appl*, vol. 3, pp. 159–170, 2010.

[34] F. Khan, *The physics of radiation therapy.* 2009.

[35] M. Durante, "New challenges in high-energy particle radiobiology," *Br J Radiol*, Nov 2013.

[36] H. Harder, H. Holtel, J. E. Bromberg, P. Poortmans, H. Haaxma-Reiche, H. C. Kluin-Nelemans, J. Menten, and M. J. van den Bent, "Cognitive status and quality of life after treatment for primary CNS lymphoma," *Neurology*, vol. 62, pp. 544–547, Feb 2004.

[37] P. K. Brastianos and T. T. Batchelor, "Primary central nervous system lymphoma: overview of current treatment strategies," *Hematol. Oncol. Clin. North Am.*, vol. 26, pp. 897–916, Aug 2012.

[38] P. E. Valk and W. P. Dillon, "Radiation injury of the brain," *AJNR Am J Neuroradiol*, vol. 12, pp. 45–62, Jan 1991.

[39] M. L. Rinne, E. Q. Lee, and P. Y. Wen, "Central nervous system complications of cancer therapy," *J Support Oncol*, vol. 10, no. 4, pp. 133–141, 2012.

[40] N. E. Anderson, "Late complications in childhood central nervous system tumour survivors," *Curr. Opin. Neurol.*, vol. 16, pp. 677–683, Dec 2003.

[41] P. L. Khong, L. H. Leung, A. S. Fung, D. Y. Fong, D. Qiu, D. L. Kwong, G. C. Ooi, G. McAlonan, G. McAlanon, G. Cao, and G. C. Chan, "White matter anisotropy in post-treatment childhood cancer survivors: preliminary evidence of association with neurocognitive function," *J. Clin. Oncol.*, vol. 24, pp. 884–890, Feb 2006.

[42] R. K. Mulhern, H. A. White, J. O. Glass, L. E. Kun, L. Leigh, S. J. Thompson, and W. E. Reddick, "Attentional functioning and white matter integrity among survivors of malignant brain tumors of childhood," *J Int Neuropsychol Soc*, vol. 10, pp. 180–189, Mar 2004.

[43] C. A. Meyers and P. D. Brown, "Role and relevance of neurocognitive assessment in clinical trials of patients with CNS tumors," *J. Clin. Oncol.*, vol. 24, pp. 1305–1309, Mar 2006.

[44] S. L. Palmer, W. E. Reddick, J. O. Glass, R. Ogg, Z. Patay, D. Wallace, and A. Gajjar, "Regional white matter anisotropy and reading ability in patients treated for pediatric embryonal tumors," *Brain Imaging Behav*, vol. 4, pp. 132–140, Jun 2010.

[45] P. K. Duffner, "Long-term effects of radiation therapy on cognitive and endocrine function in children with leukemia and brain tumors," *Neurologist*, vol. 10, pp. 293–310, Nov 2004.

[46] P. L. Khong, L. H. Leung, A. S. Fung, D. Y. Fong, D. Qiu, D. L. Kwong, G. C. Ooi, G. McAlonan, G. McAlanon, G. Cao, and G. C. Chan, "White matter anisotropy in post-treatment childhood cancer survivors: preliminary evidence of association with neurocognitive function," *J. Clin. Oncol.*, vol. 24, pp. 884–890, Feb 2006.

[47] R. K. Mulhern, T. E. Merchant, A. Gajjar, W. E. Reddick, and L. E. Kun, "Late neurocognitive sequelae in survivors of brain tumours in childhood," *Lancet Oncol.*, vol. 5, pp. 399–408, Jul 2004.

[48] C. A. Sklar and L. S. Constine, "Chronic neuroendocrinological sequelae of radiation therapy," *Int. J. Radiat. Oncol. Biol. Phys.*, vol. 31, pp. 1113–1121, Mar 1995.

[49] M. Krawczuk-Rybak, "[Endocrine disorders in children after treatment for brain tumors]," *Pediatr Endocrinol Diabetes Metab*, vol. 16, no. 2, pp. 114–118, 2010.

[50] J. Radcliffe, R. J. Packer, T. E. Atkins, G. R. Bunin, L. Schut, J. W. Goldwein, and L. N. Sutton, "Three- and four-year cognitive outcome in children with noncortical brain tumors treated with whole-brain radiotherapy," *Ann. Neurol.*, vol. 32, pp. 551–554, Oct 1992.

[51] H. A. Wahba, M. Abu-Hegazy, Y. Wasel, E. I. Ismail, and A. S. Zidan, "Adjuvant chemotherapy after reduced craniospinal irradiation dose in children with average-risk medulloblastoma: a 5-year follow-up study," *J BUON*, vol. 18, no. 2, pp. 425–429, 2013.

[52] J. Michael Fitzpatrick, L. G. Derek, Hill, and J. Calvin R. Maurer, *Image Registration.*

[53] F. J. Zitova B., "Image registration methods: a survey," *Image and Vision Computing*, p. 977 1000, 2003.

[54] J. Nocedal and W. S.J., *Numerical Optimization.* New York: Springer-Verlag, 2000.

[55] "http://superk.physics.sunysb.edu/ mcgrew/phy310/lectures/phy310-lecture-18-2007.pdf,"

[56] D. Guo, "Mutual information and minimum mean-square error in gaussian channels," *Browse Journals and Magazines*, vol. 51.

[57] "http://plastimatch.org/mutual_information.html,"

[58] D. Rueckert, L. I. Sonoda, C. Hayes, D. L. Hill, M. O. Leach, and D. J. Hawkes, "Nonrigid registration using free-form deformations: application to breast MR images," *IEEE Trans Med Imaging*, vol. 18, pp. 712–721, Aug 1999.

[59] C. Studholme, D. L. G. Hill, and D. J. Hawkes, "An overlap invariant entropy measure of 3D medical image alignment," *Pattern Recognit*, vol. 32, pp. 71, 86, 1998.

[60] R. Varadhan, G. Karangelis, K. Krishnan, and S. Hui, "A framework for deformable image registration validation in radiotherapy clinical applications," *J Appl Clin Med Phys*, vol. 14, no. 1, p. 4066, 2013.

[61] C. Davatzikos, "Spatial normalization of 3D brain images using deformable models," *J Comput Assist Tomogr*, vol. 20, no. 4, pp. 656–665, 1996.

[62] M. Iacono, Passera, Magrassi, Mainardi, Bastianello, and Lago, "A method to analyze the evolution of malignant gliomas using MRI," pp. 11548–008–0263–0, 14 September 2008.

[63] N. Kadoya, Y. Fujita, Y. Katsuta, S. Dobashi, K. Takeda, K. Kishi, M. Kubozono, R. Umezawa, T. Sugawara, H. Matsushita, and K. Jingu, "Evaluation of various deformable image registration algorithms for thoracic images," *J. Radiat. Res.*, Jul 2013.

[64] S. G.C., J. R. Li, Wolfgang, G. Chen, M. Peroni, M. F. Spadea, S. Mori, J.Zhang, J. Shackleford, and N. Kandasamy, "Plastimatch. An open source software suite for radiotherapy image processing," *In Proceedings of the XVIth International Conference on the use of Computers in Radiotherapy (ICCR), Amsterdam.*

[65] K. Murphy, B. van Ginneken, J. M. Reinhardt, S. Kabus, K. Ding, X. Deng, K. Cao, K. Du, G. E. Christensen, V. Garcia, T. Vercauteren, N. Ayache, O. Commowick, G. Malandain, B. Glocker, N. Paragios, N. Navab, V. Gorbunova, J. Sporring, M. de Bruijne, X. Han, M. P. Heinrich, J. A. Schnabel, M. Jenkinson, C. Lorenz, M. Modat, J. R. McClelland, S. Ourselin, S. E. Muenzing, M. A. Viergever, D. De Nigris, D. L. Collins, T. Arbel, M. Peroni, R. Li, G. C. Sharp, A. Schmidt-Richberg, J. Ehrhardt, R. Werner, D. Smeets, D. Loeckx, G. Song, N. Tustison, B. Avants, J. C. Gee, M. Staring, S. Klein, B. C. Stoel, M. Urschler, M. Werlberger, J. Vandemeulebroucke, S. Rit, D. Sarrut, and J. P. Pluim, "Evaluation of registration methods on thoracic CT: the EMPIRE10 challenge," *IEEE Trans Med Imaging*, vol. 30, pp. 1901–1920, Nov 2011.

[66] "http://plastimatch.org/registration_command_file_reference.html,"

[67] "http://www.mathworks.com/matlabcentral/fileexchange/8797-tools-for-nifti-and-analyze-image/content/load_untouch_nii.m,"

[68] "http://www.vtk.org/,"

[69] J. Vymazal, M. Hajek, N. Patronas, J. N. Giedd, J. W. Bulte, C. Baumgarner, V. Tran, and R. A. Brooks, "The quantitative relation between T1-weighted and T2-weighted MRI of normal gray matter and iron concentration," *J Magn Reson Imaging*, vol. 5, no. 5, pp. 554–560, 1995.

[70] J. Park, J. P. Mugler, W. Horger, and B. Kiefer, "Optimized T1-weighted contrast for single-slab 3D turbo spin-echo imaging with long echo trains: application to whole-brain imaging," *Magn Reson Med*, vol. 58, pp. 982–992, Nov 2007.

[71] B. G., "Multi-Planar Reconstructed Magnetic Resonance Imaging as a tool for anatomical investigation," *Department of Radiology Royal Adelaide Hospital, North Terrace Adelaide Australia.*

[72] M. Larson, P. Weisser, K. Block, M. Beeres, R. Bauer, S. Boettger, R. Hammerstingl, and T. Vogl, "Free Breathing Radial 3D VIBE Contrast enhanced MR imaging. A time saving protocol in pediatric MR examinations of children under general anesthesia," *RSNA*, 2012.

[73] "http://nifti.nimh.nih.gov/background/,"

[74] S. M. Smith, "Fast robust automated brain extraction.," *Human Brain Mapping*, vol. 14, pp. 143 – 155, 2002.